

FUNDAMENTAL PHYSICS AND PRACTICAL APPLICATIONS OF
ELECTROMAGNETIC LOCAL FLOW CONTROL IN HIGH SPEED FLOWS (RUTGERS)

AFOSR GRANT FA9550-07-1-0215

Greg Elliott[†], Nick Glumac^{††}, and Eli Lazar^{†††}

[†]Professor, Department of Aerospace Engineering

^{††}Professor, Department of Mechanical Science and Engineering

^{††}Graduate Student, Department of Mechanical Science and Engineering

University of Illinois at Urbana-Champaign

Submitted to:

Dr. John Schmisser

Air Force Office of Scientific Research

875 North Randolph Street

Suite 325, Room 3112

Arlington, VA 22203

Phone: (703) 696-6962 · Fax: (703) 696-8451

Email: John.Schmisser@afosr.af.mil

February 16, 2010

REPORT DOCUMENTATION PAGE

Form Approved
OMB No. 0704-0188

The public reporting burden for this collection of information is estimated to average 1 hour per response, including the time for reviewing instructions, searching existing data sources, gathering and maintaining the data needed, and completing and reviewing the collection of information. Send comments regarding this burden estimate or any other aspect of this collection of information, including suggestions for reducing the burden, to the Department of Defense, Executive Service Directorate (0704-0188). Respondents should be aware that notwithstanding any other provision of law, no person shall be subject to any penalty for failing to comply with a collection of information if it does not display a currently valid OMB control number.

PLEASE DO NOT RETURN YOUR FORM TO THE ABOVE ORGANIZATION.

1. REPORT DATE (DD-MM-YYYY) 2/16/2010	2. REPORT TYPE Final report	3. DATES COVERED (From - To) 3/15/2007 to 11/30/2009			
4. TITLE AND SUBTITLE FUNDAMENTAL PHYSICS AND PRACTICAL APPLICATIONS OF ELECTROMAGNETIC LOCAL FLOW CONTROL IN HIGH SPEED FLOWS (RUTGERS)		5a. CONTRACT NUMBER 5b. GRANT NUMBER FA9550-07-1-0215 5c. PROGRAM ELEMENT NUMBER 5d. PROJECT NUMBER 5e. TASK NUMBER 5f. WORK UNIT NUMBER 8. PERFORMING ORGANIZATION REPORT NUMBER AFOSR-FR-2010			
6. AUTHOR(S) Gregory Elliott, Nick Glumac, and Eli Lazar		9. SPONSORING/MONITORING AGENCY NAME(S) AND ADDRESS(ES) Air Force Office of Scientific Research 875 North Randolph Street Suite 325, Room 3112 Arlington, VA 22203			
10. SPONSOR/MONITOR'S ACRONYM(S) Program Manager: Dr. John Schmisser		11. SPONSOR/MONITOR'S REPORT NUMBER(S)			
12. DISTRIBUTION/AVAILABILITY STATEMENT Approved for Public Release					
13. SUPPLEMENTARY NOTES					
14. ABSTRACT An experimental research program conducted at the University of Illinois examined fundamentals of energy deposition processes, as well as, electromagnetic local flow control (ELFC) in high speed applications. A new ELFC device that utilizes a microwave co-axial resonator (MCAR) for pulsed frequencies between 400 Hz to 10 kHz was characterized for pressures ranging from 0.05 atm to 1 atm. Additionally the effect of reduced pressure and multiple wavelengths was studied for the plasmas formed from laser induced optical breakdown. The application of ELFC as a means of active flow control for the shear layer above a supersonic cavity in the open configuration was investigated at a freestream Mach number of 1.4. Analysis of phase averaged schlieren images and 2D velocity field characterized the formation and growth of a coherent large-scale structure in the wake of the generated disturbance. Also the application of ELFC in a sonic underexpanded jet injected normally into a Mach 2.25 crossflow was shown to not only perturb the shock wave interaction, but also induced the formation of vortices, which may lead to improved mixing of the jet with the freestream.					
15. SUBJECT TERMS electromagnetic local flow control, cavity flows, transverse jet, mixing, high speed flows, plasmas					
16. SECURITY CLASSIFICATION OF: a. REPORT Unclassified	b. ABSTRACT Unclassified	c. THIS PAGE Unclassified	17. LIMITATION OF ABSTRACT no limit	18. NUMBER OF PAGES 87	19a. NAME OF RESPONSIBLE PERSON Gregory Elliott 19b. TELEPHONE NUMBER (Include area code) 217-265-9211

Reset

Standard Form 298 (Rev. 8/98)

Prescribed by ANSI Std. Z39-18

Adobe Professional 7.0

Abstract

Electromagnetic local flow control (ELFC) has been investigated as part of a joint research effort with Rutgers University (Prof. Doyle Knight) and the University of Minnesota (Prof. Graham Candler). The experimental research program conducted at the University of Illinois examined fundamental aspects of the energy deposition process (i.e. arcs and plasmas generated by microwaves and lasers), as well as, applications for local flow control in high speed flows (particularly those relevant to high-speed air-breathing propulsion applications). Fundamental measurements were conducted of a new ELFC device that utilizes a microwave coaxial resonator (MCAR) for pulsed and continuous generation of plasmas. This device utilizes a quarter-wave resonator to generate a localized pulsed plasma at frequencies between 400 Hz to 10 kHz, and was investigated for pressures ranging from 0.05 atm to 1 atm. Following studies to optimize the configuration of the device, the resulting plasma was characterized using emission imaging, emission spectroscopy and schlieren photography to show the resulting effects on the surrounding flow field in quiescent air. Examination of phase averaged schlieren images revealed that a blast was produced by the emission that could be used to alter a flow field. Vibrational and rotational temperatures of the plasma were determined from the emission spectroscopy for a wide range of experimental conditions. Additionally the research conducted further experimental investigations on the plasma and flow field resulting from laser induced optical breakdown including collecting data on the characteristics at lower pressures and multiple wavelengths (266nm and 532 nm). The study suggested that the plasma generated by the 266nm wavelength results in a lower peak temperature and more rapid temperature decay rate for the lower pressure cases. In addition to these fundamental investigations of the plasmas and flow fields produced by laser and microwave energy deposition methods, the application of ELFC was investigated in two high-speed flows. The first of these investigated the effectiveness of pulsed energy deposition as a means of active flow control for the shear layer above a supersonic cavity in the open configuration. The study was conducted at a freestream Mach number of 1.4 and for a cavity length-to-depth ratio of 5.29. The flow field was analyzed over a range of delay times from the excitation laser pulse using schlieren photography and particle image velocimetry. Analysis of phase averaged schlieren images suggested the formation and growth of a coherent large-scale structure (consisting of two adjoining vortices) in the wake of the generated disturbance. This result was confirmed through two-component velocity field data obtained from particle image velocimetry measurements. The velocity information was also used to determine the instantaneous convective velocity and define characteristic scales for the large-scale structure. The second flow field investigated was of a sonic underexpanded jet injected normally into a Mach 2.25 crossflow. The jet exit geometry was circular and was operated at a jet-to-crossflow momentum flux ratio of 1.7. The unperturbed flow field was analyzed with schlieren imaging, PIV velocity data, surface oil flow visualizations, and pressure sensitive paint measurements. As a means of excitation to the flow field, an energy pulse from a Q-switched Nd:YAG laser was focused in the center of the jet exit at three different vertical locations. The perturbed flow field was analyzed with schlieren photography and particle image velocimetry. Analysis of phase averaged schlieren images suggested that the resulting blast wave from the laser pulse disrupted the structure of the barrel shock and Mach disk. The two-component velocity field data revealed that the excitation pulse also caused a perturbation to the jet shear layer and induced the formation of vortices, which may lead to improved mixing of the jet with the freestream, that convect downstream.

1. INTRODUCTION

Although the prospect of controlling the characteristics of a flow field has been a subject of interest since the turn of the twentieth century, the full development of the technology and understanding of the underlying physics has remained incomplete. Historically, the science of flow control was first pioneered by Prandtl [1] who demonstrated the use of suction to delay boundary layer separation from the surface of a cylinder. Later, development of flow control methods received accelerated growth as new fluid dynamic techniques were sought after to progress aeronautically superior vehicles. Flow control research remained primarily an interest of the military until the 1970s, when energy crises forced a noticeable shift of concentration to the civilian sector. During this period government agencies and private corporations invested extensive resources in search of methods to conserve energy for civilian air, sea, and land vehicles; similar efforts were also pursued for industrial applications (e.g. drag reduction in pipelines). Following this era and beyond, more complex control devices have been researched and developed, specifically geared toward manipulating the coherent structures in transitional and turbulent shear flows. [2] [3]

Although several schemes for classifying flow control methods exist, a commonly used distinction is to consider the energy expenditure and the control loop involved. Under this classification two main categories of flow control devices emerge, passive and active control. Passive control methods require no auxiliary power or control loop and utilize a permanent disturbance to the flow field, either through a geometric alteration to a surface or by a mounted obstruction in the flow. They are typically inexpensive and simple and can be employed through a variety of mechanisms. Some common examples include: rigid fixed fences, spoilers, ramps, and passive bleed systems. [4] While many studies have demonstrated the effectiveness of passive control methods, these techniques are inherently limited as they typically can only be designed for a small range of flow conditions.

In contrast, active control methods utilize an energy expenditure which provides the application of a steady or unsteady input into a flow field. [3] Such techniques can then exploit the inherent instability mechanisms of a flow field, thereby amplifying a small control input to achieve a larger global effect. [2] Therefore, to maximize the efficiency of a device the external perturbations should match the flow instability band to take advantage of the natural amplification of the flow. [5] Active control methods also require a control loop that is further

divided into predetermined and reactive categories. For predetermined control, no sensed information is recorded and the modifying input is applied without regard to the particular state of the flow field. Techniques utilizing this design use an open-loop control and no flow monitoring sensors are required. Conversely, reactive (or closed-loop) control is a class of active control in which the modifying input is continuously adjusted based on flow field quantities which are directly measured or estimated. [3] While there is typically an increased complexity in involving a feedback response, the added versatility allows a control device to be effective over a wider range of flow conditions and Mach numbers. As a result, this type of active control is often advantageous for most applications.

In general, primary active flow control methods include: acoustic excitation, continuous or pulsed suction, synthetic jets, and micro-electro-mechanical systems (MEMS). [6] In relevance to cavity flow fields, the use of steady or pulsating microjets has acquired particular interest as a means of active flow control. In addition to being effective at controlling the cavity oscillations, this technique is advantageous as it is small, robust, and capable of producing a high momentum flux with a very small mass flux. [7] However, there are several disadvantages associated with them, as well as with other mechanical devices. In particular, with devices such as blowing/suction jets, there are inherent challenges with installation and concerns with reliability and performance under extreme conditions such as icing or trapped debris. [8] Accordingly, in recent years and of particular interest to the current study there has been a renewed interest in the use of energy deposition for high-speed flow control. A selective review of using energy deposition as a means of aerodynamic flow control at high-speed is given by Knight. A more detailed overview covering all flow control methods is available in Ref. [3]. The scope of the present research activity is research activity encompasses a range of approaches (e.g. plasma arcs, pulsed lasers, microwaves) for use in practical applications, including: mixing, lift and moment enhancement, and in forcing modifications to shock structures. [9] [10]

The research activity summarized in this report is part of an experimental and computational research program conducted with Rutgers University (Prof. Doyle Knight) and The University of Minnesota (Prof. Graham Candler) to perform fundamental investigations of the energy deposition process (i.e. arcs and plasmas generated by microwaves and lasers) and investigate energy deposition methods for Electromagnetic Local Flow Control (ELFC) of high speed flows relevant to Air Force applications. The research conducted at the University of Illinois focused

on the experimental study of ELFC which was two-fold. First, fundamental measurements were conducted of a new ELFC device which utilizes a microwave co-axial resonator (MCAR) for pulsed and continuous generation of plasmas. Also fundamental investigations of plasmas generated by laser induced optical breakdown were conducted, including investigations relevant to more rarified conditions found in hypersonic Mach number facilities (such as those utilized at Purdue University for boundary layer transition studies), as well as, measurements conducted using Planar Laser Induced Fluorescent techniques. Secondly, the experimental research program at the University of Illinois focused on flow fields in which ELFC shows promise including the flow field resulting from a supersonic flow above a two dimensional cavity and enhancement of large scale structures important in bringing fluids together for mixing of transverse injection into a supersonic free stream.

2. FUNDAMENTAL INVESTIGATIONS OF ENERGY DEPOSITION METHODS

Among all energy deposition methods, the use of plasma actuators has been established as an emerging field for aerodynamic flow control. While the method itself is not entirely new, recent technological advances have allowed sufficient quantities of plasma to be produced efficiently at atmospheric conditions, thereby allowing high performance and low cost flow control devices to be developed. First investigations into the use of plasmas as aerodynamic flow control were conducted by Kilmov et al. [11] who reported on an observed decrease in the strength of a propagating normal shock in the presence of a weakly ionized flow. More recent efforts have expanded to include: lift enhancement, drag reduction, noise control, etc. The use of plasma as flow control can be accomplished through several different approaches. Of relevance to the current work are plasmas initiated by microwaves and laser-induced optical breakdown.

2.1. Microwave Generated Plasma

There are a variety of methods which have been shown to be effective in generating pulsed or continuous plasmas for ELFC (i.e. barrier discharges, electric arcs, laser discharges) each have their own inherent advantages and disadvantages. Therefore as part of the present study a microwave based system utilizing a quarter-wave microwave coaxial resonator (MCAR) was investigated. In general, a quarter-wave microwave coaxial resonator (MCAR) consists of outer and inner conductors which are short circuited at one end and left open circuited at the opposing

end. Additionally, an equivalent electrical circuit of such a device can be developed with capacitive (C_o) and inductive (L_o) elements that determine the resonant frequency and a resistive (R_o) element to incorporate losses (see Fig 1).[12] This configuration allows for coupling of the microwave energy into the resonator, which at steady state produces a standing wave that has a voltage node at the short circuited end and a voltage maximum at the open circuited end. Accordingly, a large microwave electric field exists at the open circuited end and due to the coaxial structure of the resonator, has its highest values at the inner conductor.[13] In properly designing such a resonator, there are a number of parameters that need to be considered. The first is the length of the resonator (L) which scales with the electromagnetic wavelength (λ) of the microwaves and is determined by ($\lambda/4$). For the current investigation, the operating frequency (f) used was fixed at 2.45 GHz, resulting in a theoretical L of 30.6 mm. However, in practice the actual length used is usually slightly shorter to account for the capacitive effect at the open end of the resonator.[12] For the diameter of the resonator, loss mechanisms and a calculation of the maximum electric field of the inner conductor at the open circuited end ($E_{r,max}$) need to be considered. Following the work presented by Linkenheil et al.[14] the measure representing the losses of the resonator is the quality factor (Q). This parameter is defined as the ratio of maximum reactive power ($P_{B,max}$) to the input power (P_w) consumed:

$$Q = \frac{P_{B,max}}{P_w}. \quad (1)$$

The dominant loss mechanism is the loss in the resonator walls (along z-axis), which can be calculated through:

$$\frac{dP_w}{dz} = \frac{2\pi R_s}{Z_{FO}^2} \frac{1 + \frac{D}{d}}{D \left[\ln \left(\frac{D}{d} \right) \right]^2} \cdot U(z)^2, \quad (2)$$

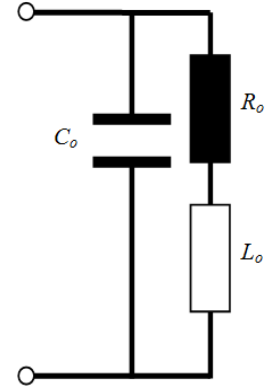


Fig 1. Equivalent circuit of quarter wavelength resonator.

where D and d represent the diameters of the outer and inner conductors of the resonator, and R_s (surface resistance), Z_{FO} (free-space characteristic impedance), and $U(z)$ (voltage along the resonator) are given by:

$$R_s = \sqrt{\frac{\mu_o \omega}{2\kappa}}, \quad (3)$$

$$Z_{FO} = \sqrt{\frac{\mu_o}{\epsilon_o}}, \quad (4)$$

$$U(z) = |U_{\max}| \cdot \sin\left(2\pi \frac{z}{\lambda}\right). \quad (5)$$

In Eqs. (3) and (4) μ_o is the permeability of free space, ω , the angular frequency, κ , the conductivity of the material, and, ϵ_o , the permittivity of free space. Integration of Eq. (2) along the resonator axis gives:

$$P_w = \frac{\pi^2}{Z_{FO}^2} \frac{c \sqrt{\mu_o}}{4\sqrt{\pi \cdot \kappa \cdot f}} \frac{1 + \frac{D}{d}}{D \left[\ln\left(\frac{D}{d}\right) \right]^2} |U_{\max}|^2, \quad (6)$$

where c is the speed of light. The reactive power has its maximum value in case of resonance and can be calculated through:

$$P_{B,\max} = \frac{1}{2} \cdot |U_{\max}|^2 \cdot B_{\text{Res}}, \quad (7)$$

with

$$B_{\text{Res}} = \frac{\pi}{4} \cdot \frac{1}{Z_L}, \quad (8)$$

where B_{Res} is the susceptance in case of resonance and Z_L is the characteristic impedance of the resonator given by:

$$Z_L = \frac{Z_{FO}}{2\pi} \cdot \ln \frac{D}{d}. \quad (9)$$

Substituting Eqs. (6) through (9) into Eq. (1), the quality factor is given by :

$$Q = Z_{FO} \frac{\sqrt{\pi \cdot \kappa \cdot f}}{c\sqrt{\mu_o}} \cdot \frac{D \cdot \ln \left(\frac{D}{d} \right)}{1 + \frac{D}{d}}. \quad (10)$$

Considering Eq. 10, the quality factor maximizes for $D/d = 3.6$, whereas the absolute value of this maximum depends upon the diameter of the outer conductor. This ratio is also consistent with the value at which conventional coaxial transmission line has minimum losses.[13] Neglecting fringing effects, the maximum electric field (which occurs at the open circuited end of the inner conductor) is given by:

$$E_{r,\max} = \frac{1}{d} \cdot \frac{|U_{\max}|}{\ln \left(\frac{D}{d} \right)}. \quad (11)$$

Combining Eqs. (7) through (11) with Eq. (1), the input power as a function of the maximum electric field is described by:

$$P_W = \frac{1}{2 \cdot 4 \cdot 60 \cdot 120\pi} E_{r,\max}^2 \cdot D \left[\frac{1}{\left(\frac{D}{d} \right)^2} + \frac{1}{\frac{D}{d}} \right] \cdot \frac{\lambda}{4} \sqrt{\frac{\mu_o \cdot \epsilon_r \cdot \omega}{2\kappa}}. \quad (12)$$

In contrast to the quality factor [Eq. (10)], no exact value for the D/d ratio exists to minimize the input power for a given $E_{r,\max}$ and D . Furthermore, from Eq. (12), if $E_{r,\max}$ and D are held constant, it can be seen that the required power is directly proportional to the diameter of the inner conductor. Accordingly, the dimensions of the outer and inner conductors of the MCAR design require a balance between minimum losses and a maximum electric field. Hence, no

optimal values exist. A final parameter to consider in the design of the resonator is the coupling height h . This parameter characterizes the distance from the short circuited end of the resonator to the point where the coaxial feeding line is located and determines the input impedance.[13] For a $50\ \Omega$ system, Linkenheil et al.[14] report that a coupling height of 1 mm will minimize the reflected power of a similar system. For the design of the MCAR in the current study, to allow for testing of different connection configurations between the feeding line and resonator, a slightly larger coupling height of 1.7 mm was used.

2.1.1. Microwave Co-axial Resonator (MCAR) System

In the current experimental study, microwave-excited plasma was generated for investigation using a quarter-wave coaxial resonator. The microwave power system included a 1.8 kW magnetron head which delivered an output at a frequency of 2.45 GHz (a band reserved for industrial, scientific, and medical applications). The accompanying power supply was capable of delivering a continuous or pulsed input signal. In continuous mode, the power of the magnetron was able to be adjusted over the range of 160 W up to 1.6 kW, where the output level being used was controlled at an interface on the power supply (or magnetron) and expressed as a percentage of the maximum system power (1.8 kW). In pulsed mode, the magnetron produced a peak power of 8 kW and allowed for pulsing frequencies ranging from 400 Hz to 10 kHz and pulse on-times from 20 μ s to 500 μ s. This resulted in a duty factor ranging 0.8 % to 20 %, and a corresponding maximum average power of 1.6 kW. Similar to the operation in continuous mode, the power output level being used was controlled and expressed as a percentage of the maximum average power level of the system (1.6 kW). A schematic and image of the experimental setup are shown in Fig 2. The design and construction of the system shown in Fig 2 was provided by Gerling Applied Engineering.

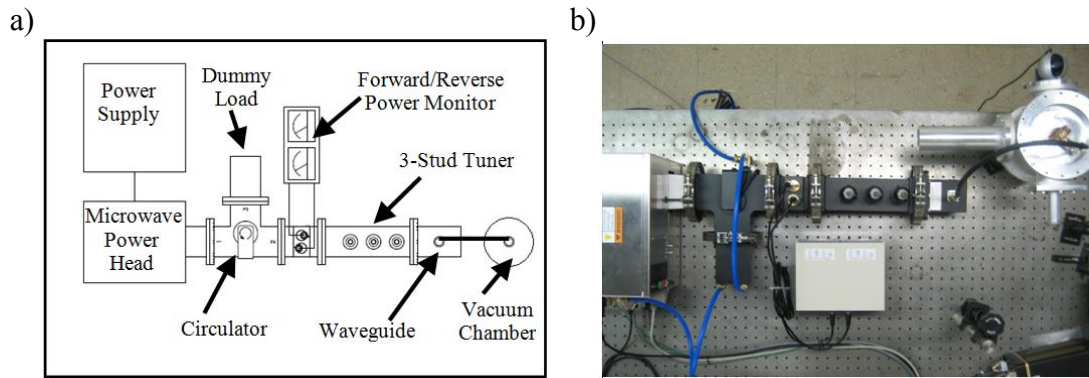


Fig 2. (a) Schematic and (b) photographic image of experimental setup for producing microwave generated plasma.

A vacuum pump and throttle valve allowed investigation of the plasma in the chamber at pressures of air ranging from 0.05 atm to 1 atm. The vacuum chamber was also fitted with two 50 mm and one 25 mm ports to allow for optical access. The quarter-wave coaxial resonator was fabricated completely out of copper; relevant dimensions have also been summarized in Table 1 and an illustration is shown in Fig 3. It should be noted that to optimize the position of the plasma, the length of the inner conductor was extended slightly beyond the outer conductor (1 to 2 mm). Additionally, the tip of the inner conductor (at the open circuited end) was tapered to a point to increase the electric field at this location.

Table 1 Mechanical dimensions of resonator

Property	Symbol	Value [mm]
Outer conductor diameter	D	0.12
Inner conductor diameter	d	0.05

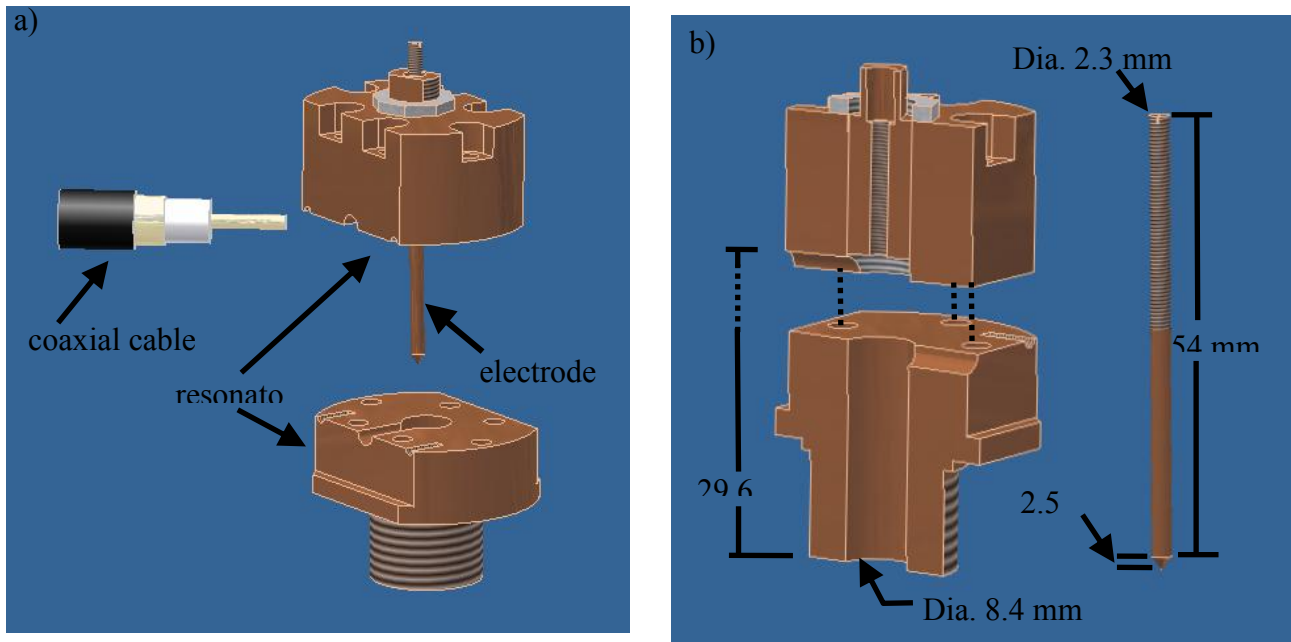


Fig 3 (a) Full and (b) split view of quarter-wave coaxial resonator

2.1.2. Diagnostics for the MCAR Investigation

Preliminary examination of the generated plasma was obtained through images recorded with a CCD camera (1600 x 1200 pixel array) and temporal emission waveforms from a photomultiplier tube with an accompanying oscilloscope. The photographic images were

composed with a 1500 μ s exposure of the plasma emission. Consequently, the total exposure time in producing the plasma images were scaled according the pulsing frequency and plasma on-time being used. The plasma images were then filtered to remove ambient light collected during the emission recording process and superimposed on a background image. Waveforms of the plasma emission intensity obtained by a photomultiplier with a UV Schott glass filter were based on an average of 64 traces; instantaneous traces were also recorded to investigate any transient characteristics in the discharge intensity. As a means of investigating the effectiveness of plasma and the microwave system to be used as a device for local flow control, the resulting flow field following an emission was analyzed with a standard Z arrangement schlieren system. The illumination was provided by a Q-switched Nd:YAG laser operating at 532 nm, where the laser pulse was focused using a spherical lens into a arcing chamber containing Argon gas. The generated light was then collimated through an optical diagnostic port of the vacuum chamber and focused to a point where a razor blade was positioned to obtain a visualization of the density gradients in the resulting flow field. Before entering the camera the image of the flow field was passed through a 532 nm notch filter. Instantaneous schlieren images were recorded in the horizontal knife edge configuration with a 1600 x 1200 pixel CCD camera. All equipment was controlled with a 4-channel pulse generator. For each condition tested, 200 schlieren images were collected and averaged. Lastly, emission spectra were recorded to obtain rotational and vibration temperatures of the plasma emission. Spectra were taken with a 270 mm SPEX imaging spectrometer with a 3600 gr/mm grating using 512 x 512 pixel Roper Scientific Super-Blue PI-Max intensified camera detector, yielding resolution of approximately 0.05 nm over the range of 375 nm to 381 nm. For all diagnostics used, the plasma generated by the MCAR was investigated for pressures ranging from 0.05 atm to 1 atm, frequencies between 400 Hz to 10 kHz, and for power levels of 20% to 80% of the maximum power capabilities of the magnetron head (as described in section II. A). For the plasma pulse on-time, although the full range of conditions (20 μ s to 500 μ s, as well as operating in continuous mode) were studied, results are presented only for the 20 μ s case, which is likely to be the condition with the greatest potential usefulness for flow control applications.

2.1.3. MCAR Operation and Plasma Emission Results

In principle the MCAR system can support plasma generation through three different processes. These include: electrons being emitted through field emission, electrons being generated via thermal emission, or secondary electron generation from incident electrons, photons, and ions.[14] While the investigation of these phenomena was not a direct objective of the current study, Linkenheil et al.[14] offer a brief discussion on the topic using a nearly identical system. In their findings they report that the material of the inner conductor (copper) can typically be fabricated with a low surface roughness. Therefore, assuming a normal machined surface quality, full support of the plasma solely through field emission is unlikely, though there may be a slightly positive effect in some cases. In their investigation the field strengths obtained were approximately three orders of magnitude lower than the level at which significant field emissions would be expected (3×10^9 V/m). Additionally, in their study, thermal emission was also assumed to be unlikely, as the pulsed system was examined with a rather small duty cycle. Therefore, it was concluded that the most likely cause was the additional production of secondary electrons due to incident electrons, ions, and photons, summarized in the Townsend coefficient. A strong influence with this mechanism is possible since the plasma is in direct vicinity of the inner conductor. [14] For the current study, although a wide range of conditions were tested, sustainable plasma generation was able to be achieved at relatively low system power levels and pulsing frequencies, which suggests a similar primary mechanism. However, as will be discussed in the sections to follow, variations in the characteristics of the plasma were observed with changes in pressure and frequency, which also indicate that different mechanisms may become more dominant as the conditions are varied.

In assessing the ability of the MCAR system to be used as a flow control device, a critical issue addressed was the transition between the coaxial feeding line and the resonator (i.e. getting the microwave energy into the resonator without destroying its resonant nature). The importance of the topic is realized in the minimization of the reflected input power. The method used for coupling the energy into the resonator was through a small inductive loop with its magnetic field coupling to the one of the resonator.[12] The optimized position (or radius) of the loop depends on the geometrical dimensions of the resonator, and, in our study, the loop configuration was investigated experimentally. With this effort, three configurations for the transition were constructed. In each of the three configurations 50Ω connectors were used, however, the

diameter of the inner contact was varied to allow additional positions within the resonator to be tested. Relevant physical specifications of the connectors used have been summarized in Table 2 and an illustration of each configuration is shown in Fig 4. In all cases the connectors were soldered into position. For the configuration utilizing the smaller diameter connector [Fig 4 (b) and (c)], the contact was first inserted into a small hole drilled into the resonator surface before being soldered. This was done to help fix the geometry of the inductive loop and improve the connection between the inner contact of the connector and the resonator material. The first configuration tested is shown in image (a). In image (a), the connector with the largest diameter is used. The contact is brought straight into the resonator and given a slight bend to position it firmly against the surface of the resonator. In images (b) and (c) a smaller diameter connector was used to allow a greater bending of the contact and provide a more significant inductive loop in the transition. In image (b), the contact is brought directly into the resonator and then given a 90° bend. In image (c) the length of the contact was extended to allow it to be bent to the side of the resonator first before making the 90° bend. As shown in Fig 4, for all of the configurations the dielectric surrounding the inner contact was removed once inside of the resonator area. In the discussion to follow, each of these configurations will be evaluated in efficiency and plasma production.

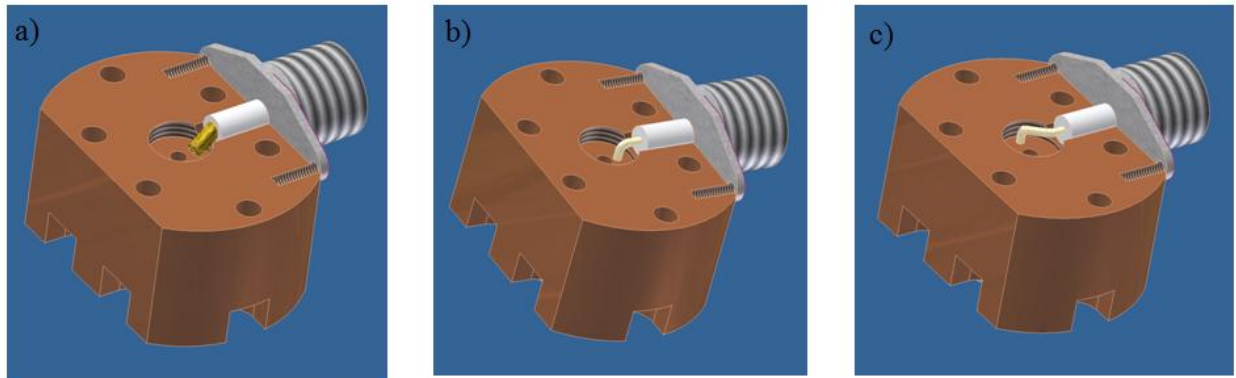


Fig 4. Connection configurations between coaxial cable connector and resonator using connectors with an inner contact diameter of: (a) 0.12 in. (large diameter), (b) 0.05 in. (small diameter), and (c) 0.05 in. (small diameter w/extended length). See Table 2 for full connector specifications.

As discussed above, the first setup tested for the transition between the feeding line and resonator is shown in Fig 4 (a). As a means of characterizing the physical attributes of the plasma generated, imaging of the plasma emission was recorded using this configuration. This

diagnostic was used to investigate the plasma under the full range of conditions specified in above.

To summarize the results obtained, selected images are presented in Fig 5 of the plasma

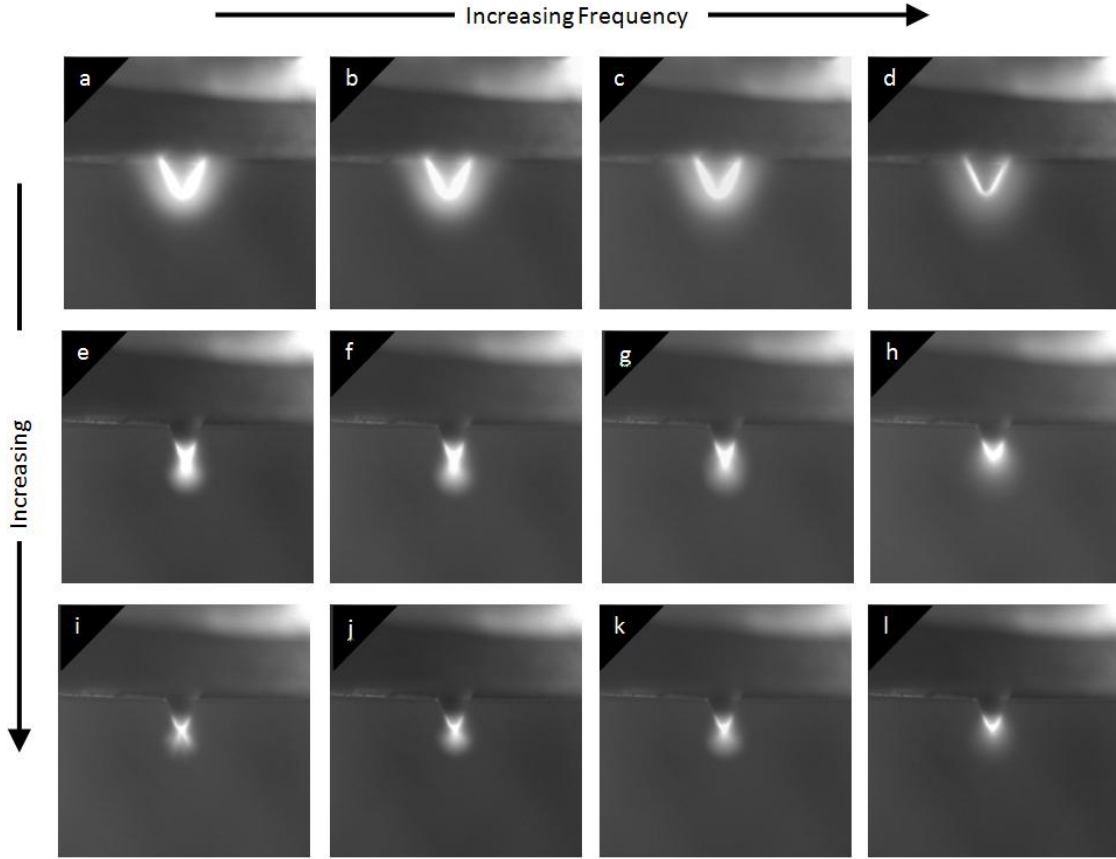


Fig 5. Images of plasma emission at 40% power for frequencies (from left to right) of: 400 Hz, 667Hz, 1,3 kHz, and 10 kHz and at pressure (from top to bottom) of: 0.05 atm, 0.5 atm, and 1 atm.

emission at a power level of 40%; for different power levels only a variation in the intensity of the emission was observed, while the general physical structure of the discharge remained primarily unchanged. For each of the images shown in Fig 5, the exposure time of the CCD camera was adjusted with the pulsing frequency of the plasma to ensure equal amounts of the emission were collected. While it was attempted to investigate the temporal behavior of a single plasma pulse (as opposed to an average appearance over multiple pulses), sufficient signal strength was unable to be obtained using a standard CCD camera. This may have been a result of the long diagnostic ports (used to prevent microwaves leakage) fitted to the vacuum chamber. These ports restricted optical access to the plasma emission and reduced to the amount of light

that could be collected. However, for the images shown in Fig 5 there are several trends that can be identified for the physical attributes of the plasma emission with changes in pressure and pulsing frequency.

In Fig 5, the images have been organized such that pressure increases down a given column and the frequency across a given row. Accordingly, pressure dependencies can be identified by individually comparing the three images for each of the four columns. Taking the first column, images (a), (e) and (i), the most noticeable characteristic is that the size of the plasma emission decreases with increasing pressure. The influence appeared to be strongest as the pressure transitioned from 0.05 atm to 0.5 atm, and then a reduced effect for the increase up to 1 atm. A more subtle observation was that for higher pressures the plasma is concentrated more towards the tip of the inner conductor. For image (e), this concentration appears to be forcing the emission to significantly detach from the inner conductor. In image (i), the detachment is still able to be observed, however, the reduction in the size of the plasma appears to be suppressing the effect. Both of these observed characteristics are further validated by comparing the images in the remaining three columns, specifically, images [(b), (f), (j)], [(c), (g), (k)], and [(d), (h), (l)].

Following a similar methodology for identifying frequency dependencies, characteristic trends can be identified by individually comparing the four images across a given row. Beginning with images (a), (b), (c), and (d), as the pulsing frequency increases, from 400 Hz [image (a)] to 10 kHz [image (d)], the amount of plasma generated appears to be decreasing. While this behavior was also observed with increasing pressure, the influence of increasing frequency does not appear to be as strong for this effect. Furthermore, in contrast to increasing pressure, this reduction in size results in a more symmetric distribution of the plasma around the inner conductor, as opposed to a concentration at the tip. These results suggest changes in the mechanisms supporting plasma generations as the external conditions are varied.

As the counterpart to the photographic images of the plasma the respective emission waveforms for the identical set of experimental conditions is presented in Fig 6. Beginning with image (a), it can be seen that there is an isolated spike in the emission profile at startup. By comparing the three waveforms in image (a), the amplitude of the observed spike increases with decreasing pressure. This result is also clearly illustrated in image (b), however, the amplitude has decreased with the increase in frequency, from 400 Hz to 667 Hz. In images (c) and (d), the amplitude of the spike continues to decrease with increasing frequency and begins to merge with

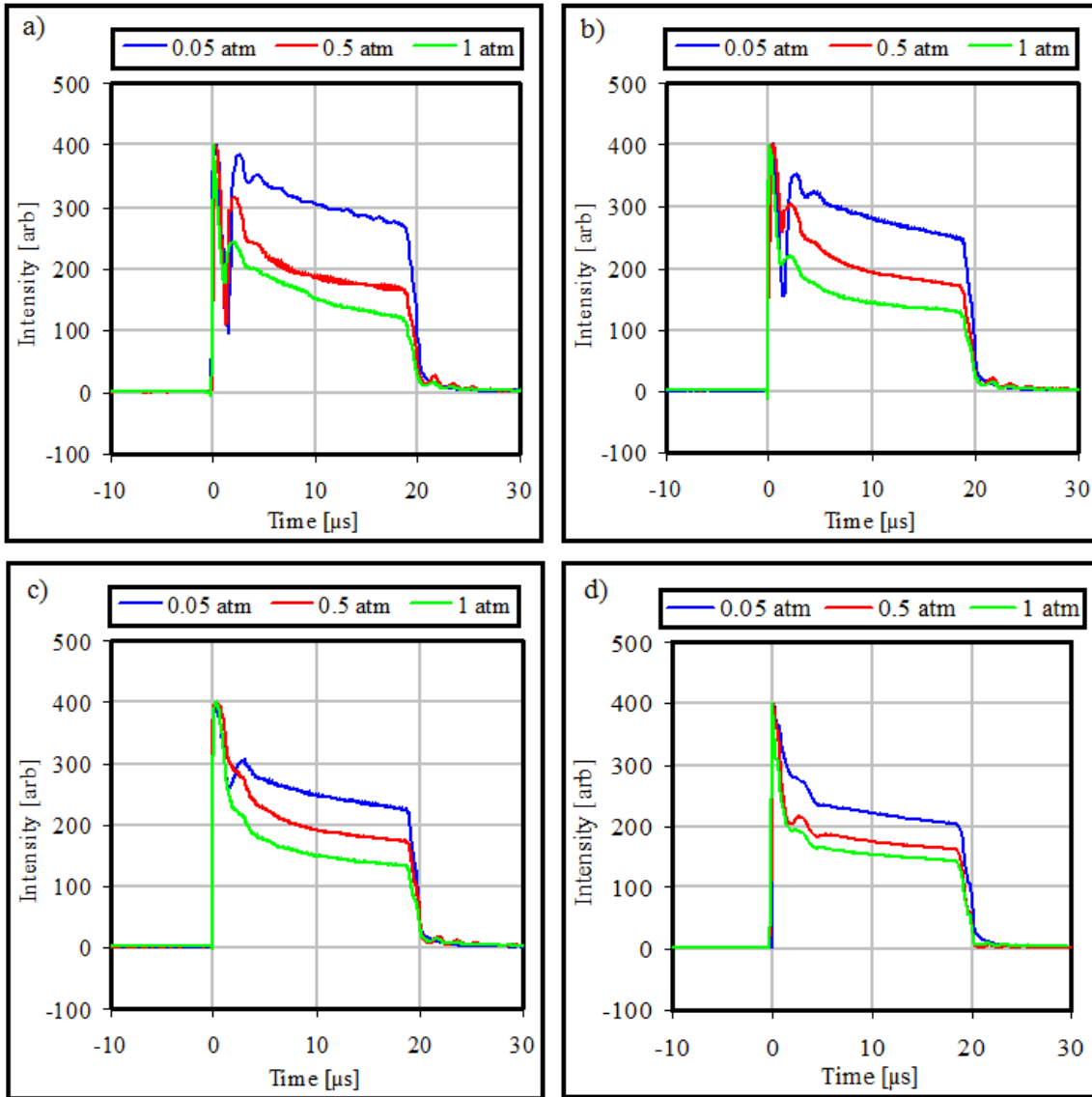


Fig 6. Emission waveforms at 40% power and for pressures of 0.05 atm, 0.5 atm, and 1 atm and at pulsing frequencies of: (a) 400 Hz, (b) 667 Hz, (c) 1.3 kHz, and (d) 10 kHz.

the rest of the profile. Although not shown in Fig 6, analysis of instantaneous waveforms revealed that this spike exhibited transient behavior and, while it was observed on average, it did not exist in every pulse. Lastly, the images collectively show that the emission temporally is more evenly distributed at lower pressures giving the intensity profile a squarer waveform. However, as the pulsing frequency increases, the profiles appear to be gradually collapsing upon one another, suppressing this observed characteristic. It should also be noted that the relative intensity of the waveform does not reveal any attributes of the plasma emission as this value was influenced by the gain of the photomultiplier tube used.

As discussed earlier, a critical component of the microwave system used is the transition between the coaxial feeding line and the resonator. Since the objective of the current investigation was to evaluate the potential of the system to be used as an efficient flow control device, three configurations for this task (see Fig 4) were tried in an attempt to minimize the reflected power. To investigate the efficiency of each of the three configurations, forward and reverse power measurements were recorded over a range of system power levels. The results are shown in Fig 7. For all of the images in Fig 7, the points represent experimental data while the lines as corresponding best fit curves. Direct measurements are presented along with that after a calibration has been applied. Both sets of data are shown to illustrate an uncertainty in the calibration used. This uncertainty was most likely brought about by influences in high levels of reflected power, forcing conditions far removed from which the applied calibration was determined. Additionally, an analog dial power meter was used to record the power levels for this investigation, bringing an additional degree of uncertainty into the data collected. However, despite these conditions, by extrapolating the experimental data with best fit curves qualitative trends can be extracted.

In the previous two sections, a discussion was given to characterize the plasma emission with pressure and frequency using the

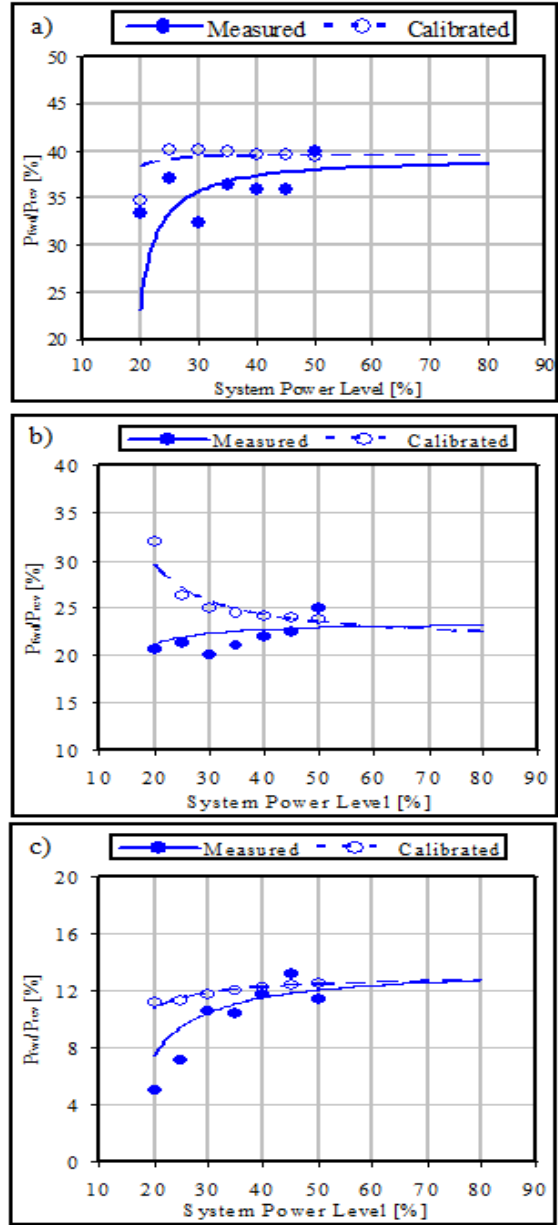


Fig 7. Reflected power for: (a) large diameter connector, (b) small diameter connector and (c) small diameter connector with extended length; see Fig 4 for illustration

configuration shown in Fig 4 (a). To investigate the efficiency of this configuration, forward and reverse power measurements, over a range of system power levels, are shown in Fig 7 (a). In image (a), it can be seen by the calibrated experimental data that the reflected power under this configuration was approximately 39 %. Therefore, only 61 % of the microwave energy was being coupled into the resonator. As a means of improving the efficiency of the system, a second configuration utilizing a small inductive loop was used, as shown in Fig 4 (b). The results of this setup are shown in image (b) of Fig 7. While observation of the calibrated data illustrates a degree of uncertainty in the reflected power for this configuration, the extrapolated curve suggests the reflected power was approximately 23%, thereby improving the overall efficiency of the system. To further validate the influence of using an inductive loop for the transition, as well as improve the performance of the system, a third configuration was used where the length of the contact was extended to allow the evaluation of an inductive loop utilizing two bends. The results of this configuration are shown in image (c), where the reflected power was minimized to approximately 13%. While image (c) currently represents the best input match achieved, these results suggest that the reflected power can be further minimized by geometrically varying the position of the inductive loop. This conclusion is also supported by previous studies that have used a similar setup. [12] [14] Currently, efforts are underway to redesign the resonator allowing the inductive loop to be more easily reshaped.

2.1.4. MCAR Schlieren Results

As a means of quantifying the effectiveness of the system to be used as a flow control device, visualization diagnostics were conducted in quiescent air to determine the instantaneous flow perturbation by the presence of pulsed plasma generation. Towards this end, instantaneous schlieren images were obtained to investigate the distribution of density gradients within the resulting flow field before and after excitation. The experimental study was conducted at incremental times (ranging from 5 μ s to 100 μ s) from the plasma energy input at the tip of the inner conductor of the resonator. Additionally, this diagnostic was carried out for a pulse on-time of 20 μ s and for each of the three connection configurations shown in Fig 4. Testing conditions included the full range of experimental pressures (0.05 atm, 0.5 atm, and 1 atm), all available system pulsing frequencies (400 Hz to 10 kHz), and for system power levels of 40 % and 80 %. For all images recorded, the knife edge was oriented horizontally. Selected images

from the three configurations are presented in Fig 8 and Fig 9 to demonstrate the ability of the system to produce a disturbance in the flow field and to be used as a local flow control device. For all the images presented, a 20 μ s delay existed between excitation and visualization. In image (a) of Fig 8, the resulting flow field is shown for the configuration utilizing a small diameter connector with extended length [Fig 4 (c)] for a pulsing frequency of 400 Hz and a pressure of 0.5 atm. While schlieren images were also recorded for the lower pressure case of 0.05 atm, the decreased density of the surrounding air coupled with the strength of the generated disturbance did not allow a density variation from the plasma pulse to be detected. In image (a) the formation of two blast waves can be seen, where the trailing disturbance (i.e. blast wave closest to the plasma) was determined to be a reflected wave that emanated from within the resonator. In image (b), all experimental conditions were held constant except for the system power level which was decreased from 80 % to 40 %. As anticipated, this change resulted in a decrease of the strength of the blast wave produced by the plasma pulse. For delay times greater than 20 μ s, the blast wave was seen to grow and decay as it moved throughout the flow field, where the density variation could no longer be detected at approximately 100 μ s. In images (c) and (d) the pressure remained at 0.5 atm, and the pulsing frequency was increased to 667 Hz. Under these conditions, the images revealed that while the structure of the blast wave remained consistent with images (a) and (b), there was a slight decrease in the observed strength. This result is more clearly seen by also observing images (e) and (f), where the pulsing frequency was further increased to 1.3 kHz. In images (e) and (f) the strength of the blast wave was decreased so significantly that the trailing wave could no longer be detected. It is speculated that under high frequency pulsing the quiescent air conditions have allowed the air in the vacuum chamber to heat up substantially enough that the thermal properties of the plasma pulse were no longer able to produce a blast wave. This result in no way inhibits the ability of this system to be used as a flow control device since for aerodynamic applications quiescent air conditions are not realized. Furthermore, by comparing images (e) and (f), the strength of resulting blast wave appeared to remain constant (if not slightly increased) with decreasing power. This observation further suggests that the temperature rise of the surrounding air in the vicinity of the inner conductor was causing the observed decrease in the strength of the resulting blast wave. However, further studies may be warranted to further investigate this result. In images (g) and (h) the pulsing frequency was increased to 10 kHz, and consistent with the findings in images (a)

through (f), the front and trailing blast wave can no longer be identified in either image. While schlieren images were also similarly investigated at this pressure for the other two configurations shown in Fig 4 [images (a) and (b)], the results of the blast wave were similar to those presented in Fig 8, however with decreased strength, as both of these cases experienced increased reflected power.

For the flow field investigation at 1 atm, schlieren images were again recorded for each of the three configurations shown in Fig 4. However, while a range of pulsing frequencies were evaluated the system power level for this case was restricted to 80%. This decision was based on the ability of the microwave system to produce sustained plasma under the same conditions for each of the three configurations shown in Fig 4. At a pressure of 1 atm and for a pulsing frequency of 400 Hz, configurations (a) and (b) in Fig 4 generated plasma that was temporally sustainable for power levels only above 40 %. As the pulsing frequency increased above 400 Hz, sustainable plasma was able to be produced for lower minimum power levels, eventually reaching 20 % for the 10 kHz case. For configuration (c), sustainable plasma was able to be produced for all combinations of the full range of frequencies (400 Hz to 10 kHz) and power levels (20 % to 80 %) evaluated. Therefore, to provide a comparative analysis of the resulting flow field for each of the three configurations, schlieren images were recorded only for a system power level of 80 %. In Fig 9, selected images are presented for pulsing frequencies of 400 Hz and 667 Hz using the small diameter connector with extended length [Fig 4 (c)]. Trends involving higher frequency pulsing are similar to those illustrated in Fig 8, for a pressure of 0.5 atm. Shown by images (a) and (b), while strong density gradients can be observed surrounding the area of the inner conductor of the resonator, only a weak, almost undetectable, blast wave was seen to be formed. Schlieren images at identical frequencies are also offered in images (c) and (d) for the small diameter configuration shown in Fig 4 (b). In this case, while the power measurements presented in Fig 7, as well as physical appearance, suggested a stronger plasma emission the blast wave formed under this configuration is more clearly identifiable. While the results are not shown, schlieren images utilizing the large diameter configuration in Fig 4 (a) were also obtained. Again, similar to the cases at 0.5 atm, the strength of the blast wave, as well as density variations in the vicinity of the inner conductor was decreased.

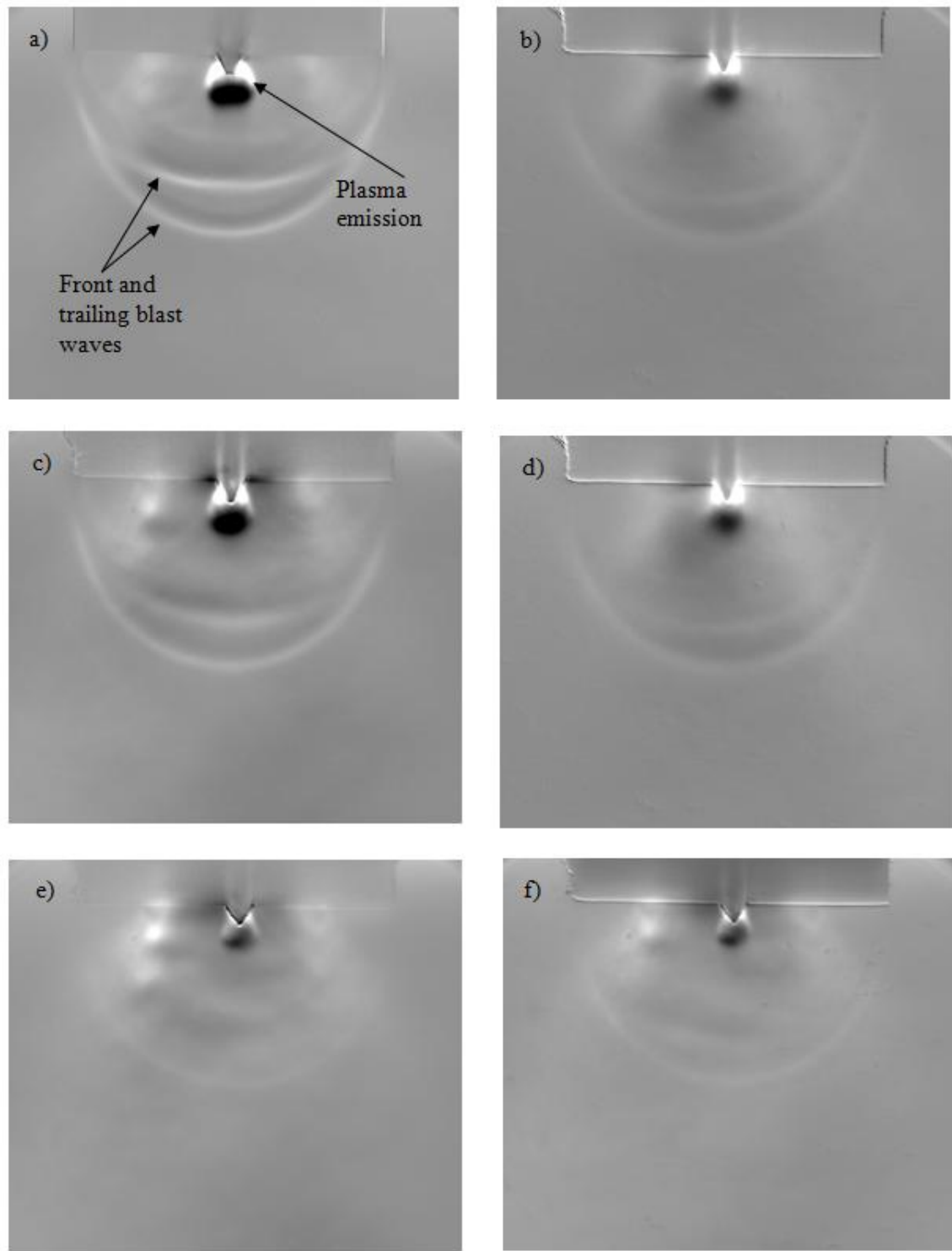


Fig 8. Schlieren images at 0.5 atm for small diameter connector w/extended length [Fig. 5(c)] for frequencies/power levels of: (a) 400 Hz/80 %, (b) 400 Hz/40 %, (c) 667 Hz/80 %, (d) 667 Hz/40 %, (e) 1.3 kHz/80 %, (f) 1.3 kHz/40 %. Cont. on next page...

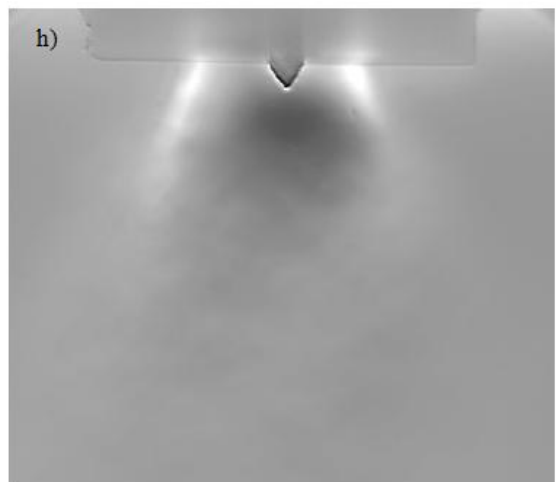
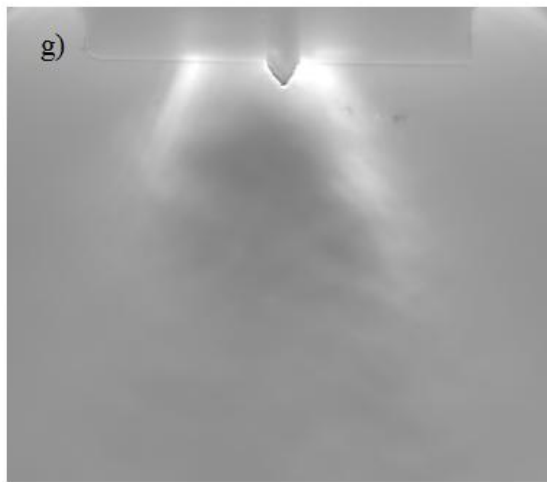


Fig 8 Cont. (g) 10 kHz/80 %, (h) 10 kHz/40 %.

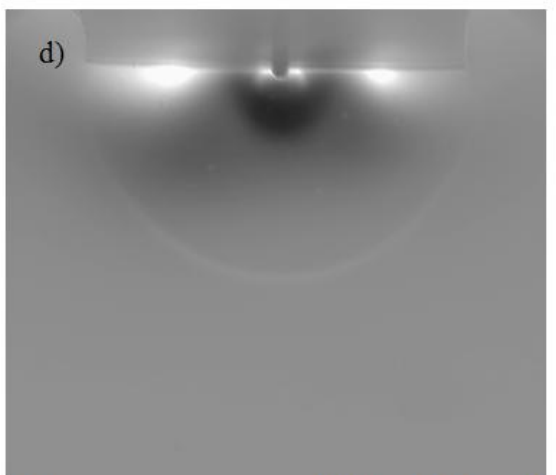
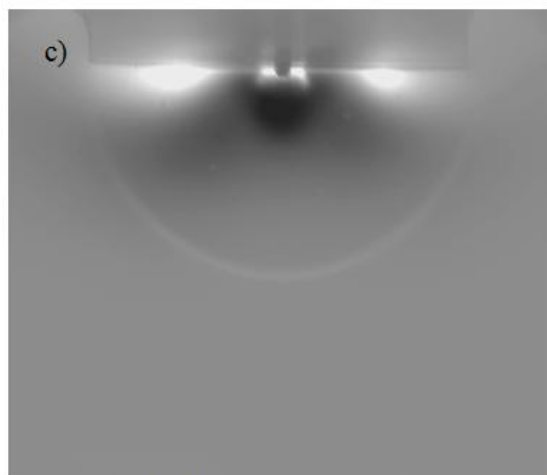
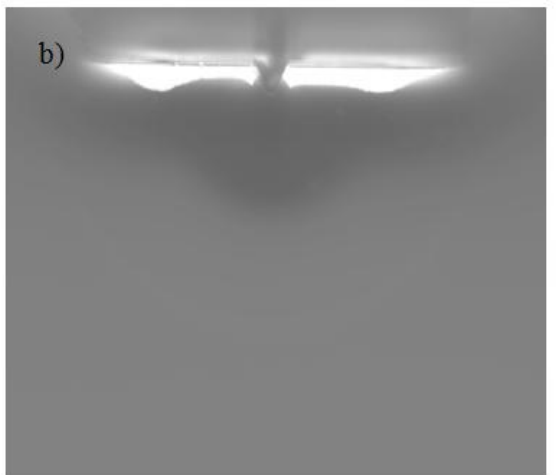
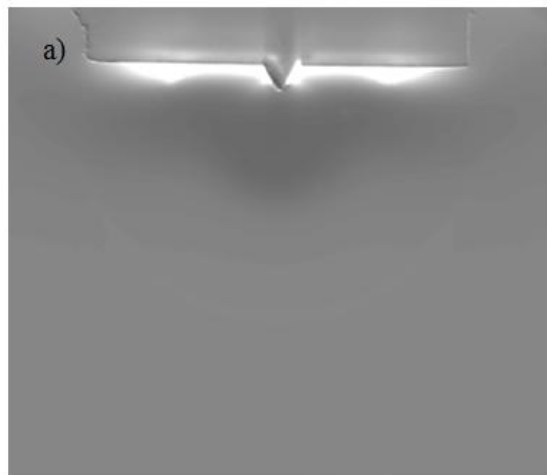


Fig 9. Schlieren images at 1 atm and 80% power for small diameter connector w/extended length [Fig 4 (c)] at frequencies of: (a) 400 Hz and (b) 667 Hz, and the small diameter connector with standard length [Fig 4 (b)] at similar frequencies of: (c) 400 Hz and (d) 667 Hz.

2.1.5. Spectroscopic Analysis of the MCAR

As a final investigation, emission spectra were taken to obtain quantitative measurements of relevant temperatures of the plasma. For application of this diagnostic and fitting of a spectroscopic model it was assumed that the plasma emission was optically thin (i.e. the emission was not self absorbing). The entire (0,2) band of the N₂ second positive system was captured along with the band head of the (1,3) band. From this region, rotational temperatures can be accurately determined, and a vibrational temperature can also be assigned based on the two bands. However, it is important to note that the vibrational population distribution is non-thermal, and so the vibrational “temperature” assigned to this plasma is of limited utility. While spectroscopy measurements were conducted for the full range of pressures, as well as for various pulsing frequencies and system power levels, selected spatially and temporally averaged data is presented in this section to identify characteristics of the plasma that were observed. For clarity, the vibrational and rotational temperatures for each of the cases to be presented have been summarized in Table 2.

In Fig 10, spatially averaged spectra over the entire plasma emission are presented for a system power level of 80%, at pressures of 0.05 atm and 1 atm, and for pulsing frequencies of

Table 2 Vibrational and rotational temperatures of plasma emission

Reference	Averaging	Pressure [atm]	Frequency [Hz]	Power [%]	T _{vib} [k]	T _{rot} [k]
Figure 11 (a)	Spatial	0.05	667	80	3329	371
Figure 11 (b)	Spatial	0.05	1,333	80	3322	412
Figure 11 (c)	Spatial	1	667	80	3293	545
Figure 11 (d)	Spatial	1	1,333	80	3134	1063
Figure 12 (a)	Spatial (Partial)	1	1,333	80	3721	975
Figure 12 (b)	Spatial (Partial)	1	1,333	80	2389	788
Figure 13 (a)	Spatial and Temporal	0.5	400	40	3679	446
Figure 13 (b)	Spatial and Temporal	0.5	400	40	4164	631

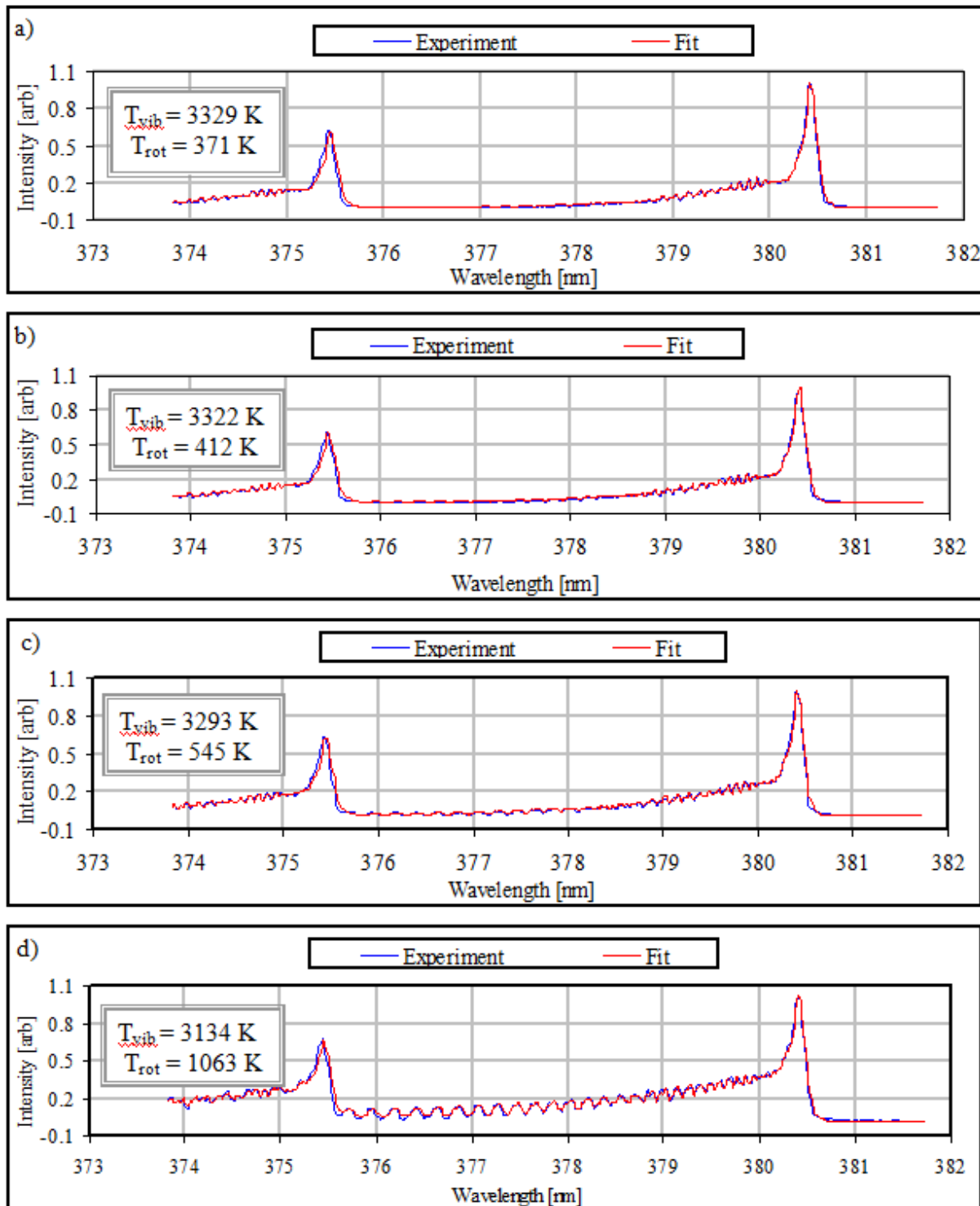


Fig 10. Spatial averaged spectra over entire plasma emission at a 80% system power level and for pressure/frequency conditions of: (a) 0.05 atm/667 Hz, (b) 0.05 atm/1.3 kHz, (c) 1 atm/667 Hz, and (d) 1 atm/1.3 kHz

667 Hz and 1.3 kHz. As seen in images (a) through (d), the spectroscopic model was able to reproduce the line positions and intensities of the experimental spectra. As expected, vibrational and rotational modes were not in equilibrium. In local thermodynamic equilibrium (LTE) plasmas, a single temperature characterizes all of the internal energy modes (i.e. vibrational, rotational, and electronic). In determining this temperature the absolute intensity of any atomic or molecular feature, or Boltzmann plots of vibrational or rotational population distributions can be used.[15] Therefore, it was concluded that the plasma was not close to LTE for any of the conditions tested. For image (d) of Fig 10, spatial averaging was also conducted for the top half (closest to the inner conductor) and bottom half of the emission region; the results are presented in Fig 11. As shown by images (a) and (b), the rotational and vibrational temperatures for the top half of the plasma were significantly higher than for the bottom half. Similar results were also obtained for the additional cases presented in Fig 10.

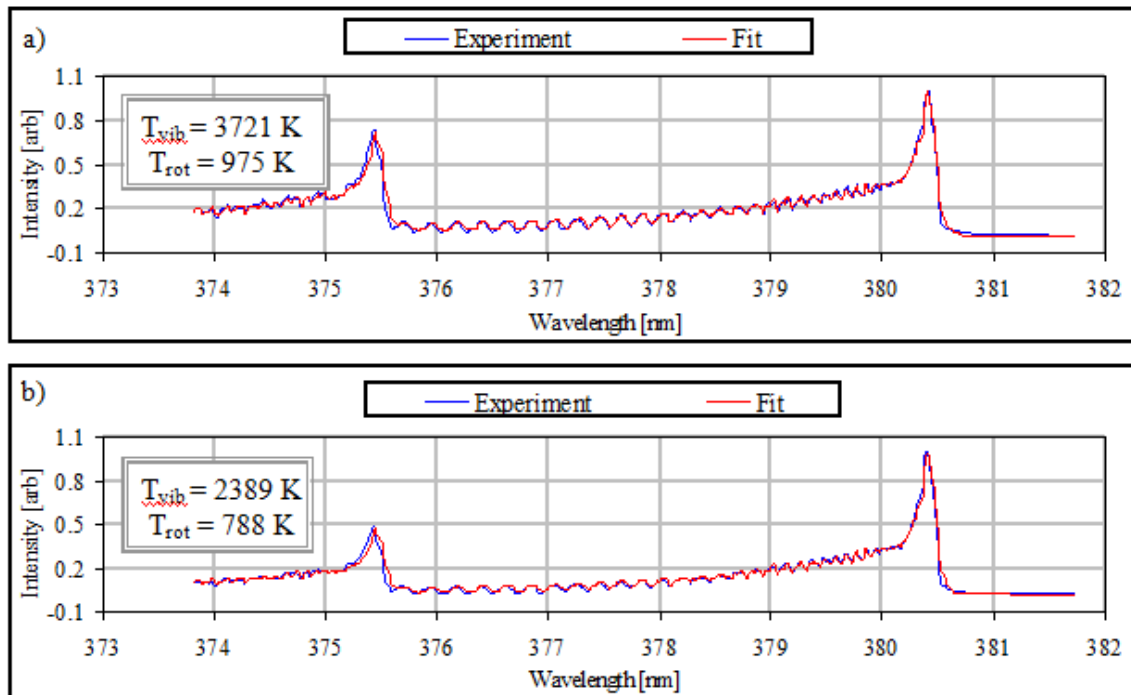


Fig 11. Spatial averaged spectra over (a) top half and (b) bottom half of emission at 80% power, 1atm, and a pulsing frequency of 1.3 kHz.

Temporal characteristics of the plasma emission were also investigated by collecting spectra of different sections of the 20 μs plasma pulse generated. Selected results for a pulsing

frequency of 400 Hz, pressure of 0.5 atm, and system power level of 40% are presented in Fig 12. While higher pulsing frequencies were investigated, the signal-to-noise ratio significantly decreased with an increase in this parameter. This observation may have been a result of the change in the physical characteristics of the plasma with increasing frequency as shown by the images in Fig 5. However, in image (a) of Fig 12 the vibrational and rotational temperatures for the front section of the plasma pulse were determined to be 3679 K and 446 K, respectively. These values were considerably lower than the temperatures determined for the middle section of the plasma as shown in image (b) and summarized in Table 2.

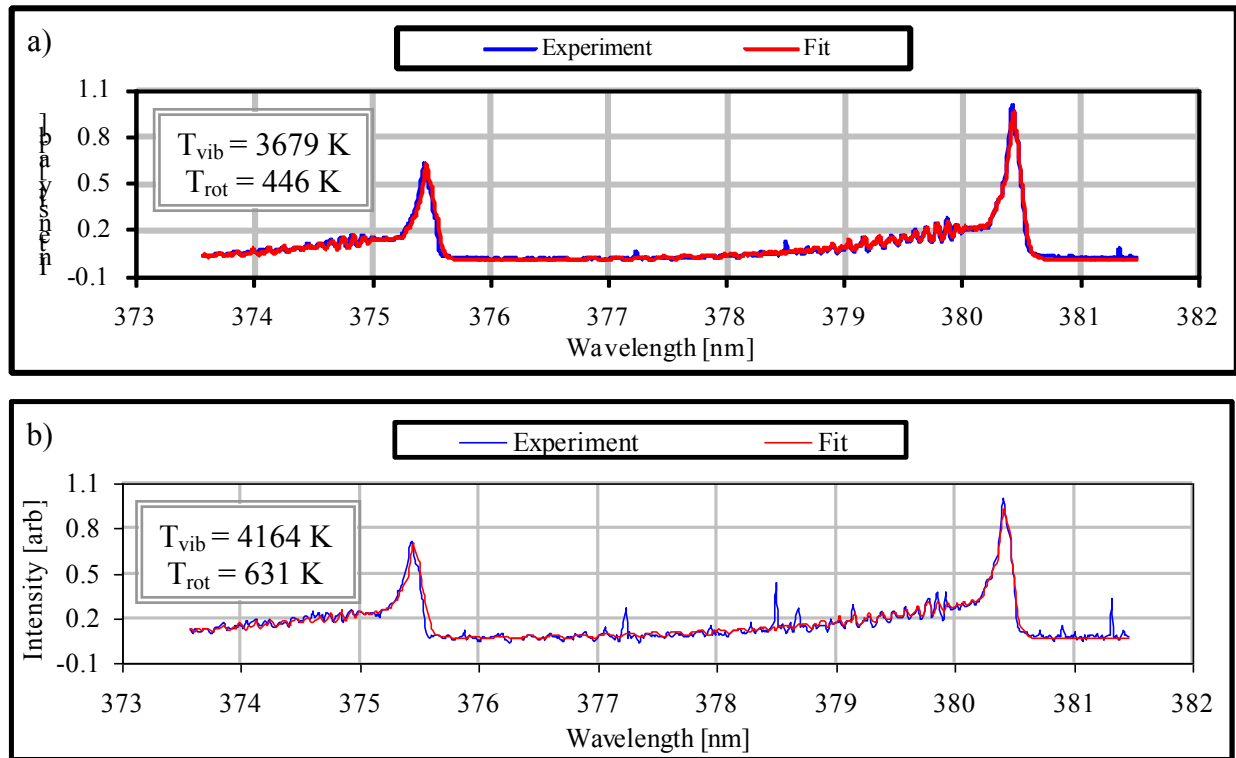


Fig 12. Spatially averaged spectra over the entire plasma emission for the temporal (a) front (b) middle sections of a 20 μs plasma pulse at 40 % power, a frequency of 400 Hz, and a pressure of 0.5 atm.

2.2. Laser Induced Optical Breakdown

Maker et al. [16] first reported on plasma through the laser-induced optical breakdown in a gas and we have conducted some fundamental studies as part of previous research efforts [17]. The process generating the plasma has been described by Raizer [18] [19], which begins when a pulsed laser beam is focused down to a small region of space and results in a rapid temperature rise in the fluid at that point. The breakdown of the air molecules leading to the ionization of the

gas is then triggered when the electric field of the laser radiation near the focus becomes greater than that of the binding electrons to their nuclei. Since the plasma becomes opaque to the laser a cascade effect incurs and more energy is absorbed. The process is described by Adelgren et al. [20] as a series of four progressive steps: 1) initial release of electrons by multiphoton effect, 2) ionization of the gas in the focal region by the cascade release of electrons, 3) absorption and reflection of laser energy by the gaseous plasma, and 4) formation and propagation of the detonation wave into the surrounding gas and relaxation of focal region plasma.

Often laser-induced optical breakdown is utilized as a pulsed plasma flow control device (as is the case in our present study) due to the ease with which the spark timing and location can be controlled and quickly changed. Additionally our present configuration provided the ability to investigate the laser-induced optical breakdown at more rarified conditions and other wavelengths (motivated by possible applications to provide flow perturbations in hypersonic wind tunnels) than we have done previously, as well as investigate the application of a unique Nitric Oxide planar laser induced fluorescence (NO-PLIF) system to study the resulting flow field.

2.2.1 Laser Induced optical breakdown: Pressure and Wavelength Investigation

Pressure and multiple wave length laser-induced optical breakdown studies were conducted for three different pressures (0.2 atm, 0.6 atm, and 1.0 atm) and for two different wavelengths (266 nm and 532 nm). For all cases the laser beam was first expanded to 50 mm in diameter and then focused to a point using spherical lenses. The lenses used were also 50 mm in diameter and each had an antireflective coating specific the wavelength of the laser light used. The lenses were positioned such that the beam focused to a point inside a sealed chamber with optical access windows on each side of it, allowing entry and exit of the laser radiation. The chamber allowed the pressure to be controlled in the environment that the plasma was formed, which was controlled with an external vacuum pump. An illustration of the experimental setup is shown in schematic in Fig 13.

The thermodynamic properties of the generated discharge are being investigated using several diagnostics. These included recording the waveforms through a photomultiplier tube, measuring the laser power before and after the plasma formed (to determine the amount of

energy absorbed by the plasma), and spectroscopic analysis. A few results from the spectroscopic analysis are shown in Fig 14. The spectroscopic measurements were processed to yield a single temperature and electron number density for a given gated exposure.

In the plots of Fig 14, a central time was defined as half of the exposure gate plus the delay time from the discharge pulse. The spectral region where only N II lines are present and which has a spectrum that is very sensitive to temperature over the 10,000–60,000K region were monitored. For the resulting spectra, a model was used which assumes an equilibrium distribution of population in electronic states corresponding to a single temperature. The linewidth is assumed to be a convolution of Doppler and Stark broadening due to a single

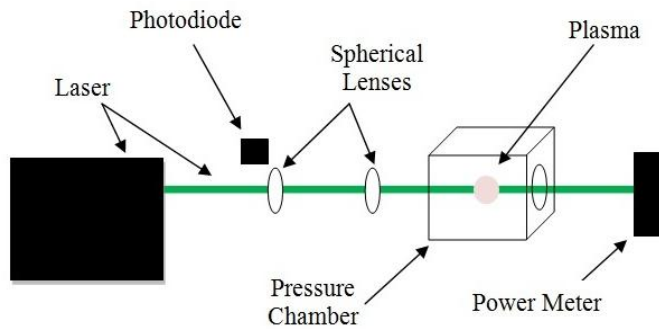


Fig 13. Schematic of laser spark setup

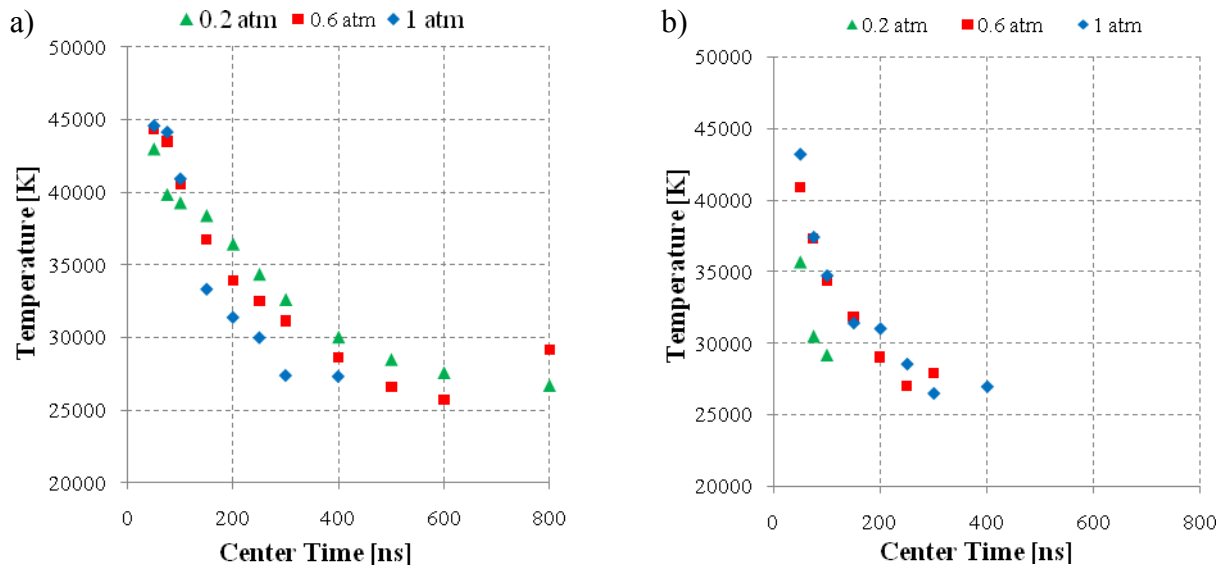


Fig 14. Spectral fit temperature at (a) 532 nm and (b) 266 nm versus time after the laser pulse for three pressure cases at a fixed incident laser energy of 75 mJ/pulse.

electron number density. Experimental broadening factors are used for the N II lines, and a linear dependence of Stark width and shift with electron number density are assumed. A spectral model fits each spectrum to a single temperature, electron number density, and optical depth. A global scaling parameter and two parameters associated with the (assumed linear) background are also determined in the fit. As observed in Fig 14 the plasma generated by the 266nm case exhibits a lower peak temperature early in the plasma formation process (particularly for the 0.2 atm case), and also appears to exhibit a more rapid temperature decay rate for the lower two pressure cases.

In addition to the spectroscopic measurements power measurements of the laser radiation were recorded to investigate the amount of energy absorbed by the plasma, and its dependence on the pressure of the surrounding environment and the wavelength of the laser light used. For this investigation the power of the laser radiation entering the pressure chamber (before the plasma formed) was measured using a power meter and then monitored during the experiment using a photodiode to verify the intensity of the laser light remained constant. The laser energy exiting the pressure chamber was then measured using the same power meter. The results

of this study are shown in Fig 15, where E_0 represents the laser energy passing directly through the chamber at a pressure low enough that the plasma was not able to form. This pressure was approximately 0.03 atm and served as a baseline reading for the measurements shown in Fig 15. Also, in Fig 15 $E(p)$ represents the measured laser energy at the exit of the pressure chamber. Fig 15 suggests that while the energy absorbed by the plasma is highly dependent on the surrounding pressure at a wavelength of 532 nm, the dependence is not as strong or possibly not existent at 266 nm. However this trend is somewhat questionable and may be due to a problem in the experimental measurement setup so further investigation is needed.

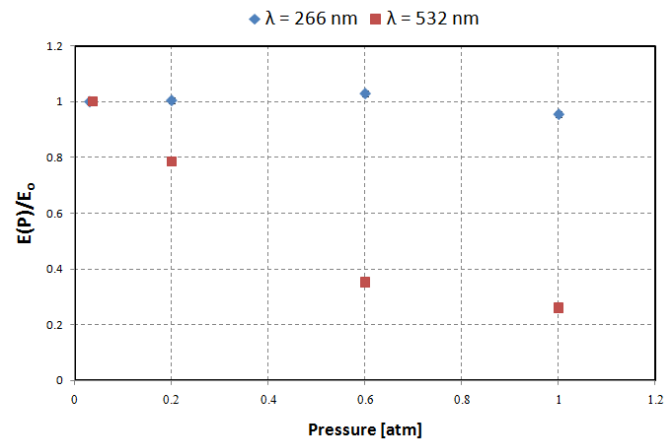


Fig 15. Energy absorbed by plasma as a function of wavelength and pressure

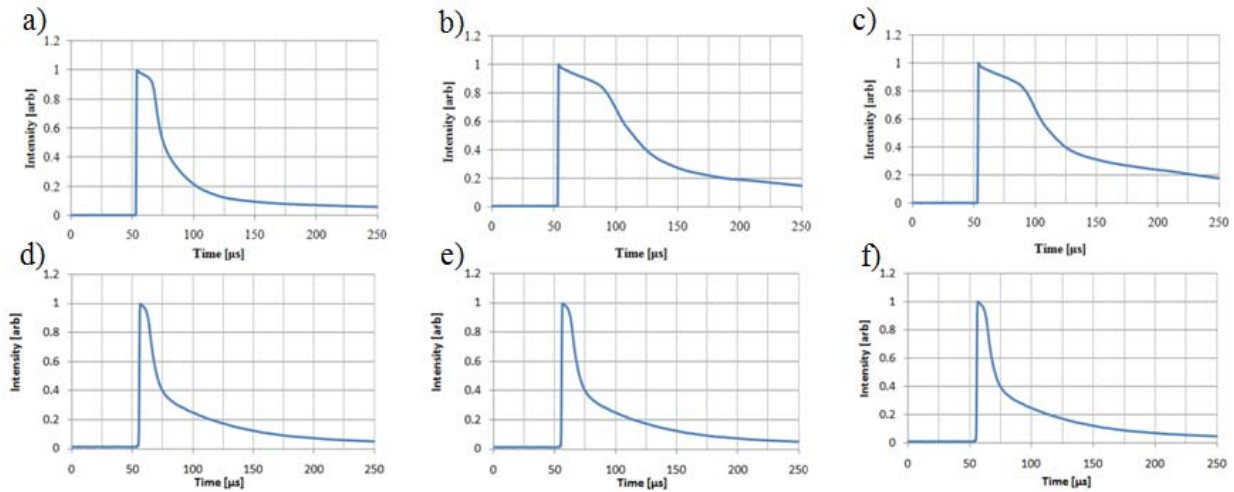


Fig 16. Waveforms of plasma emission recorded for laser light of 532 nm (top row) and 266 nm (bottom row) and at pressures of: 0.2 atm – (a) and (d), 0.6 atm – (b) and (e) , and 1 atm (c) and (f).

Lastly, recorded waveforms of the plasma radiation were recorded and are shown in Fig 16. The last row of images in Fig 16 represent the plasma emission generated with 532 nm laser light and the bottom row at 266 nm. Also, the pressure increases for the three images from left to right from 0.2 atm to 0.6 atm to 1 atm. The images in Fig 16 suggest that for the plasma generated with the 532 nm laser light the emission temporally broadens with increasing pressure. In contrast, the emission waveform appears to be independent of pressure for plasma generated with 266 nm light. The significance of this result, as well as, validation of it and the earlier trends observed may warrant further confirmation.

2.2.2. *Laser Induced optical breakdown: NO-PLIF Measurements*

In addition to the investigations of the laser-induced optical breakdown process at lower pressures and for multiple wavelengths, during the course of the present investigation NO-PLIF was also utilized to provide an additional tool to characterize the resulting plasma and flow field. This not only provided additional confirmation of previous results, but also allowed the further development of these diagnostic tools. Recently an optical parametric system to produce single-mode, narrow linewidth laser radiation useful for high-resolution spectroscopy was developed. [21] Instead of using solid-state amplification [22], cost-effective and straight-forward pulsed dye amplification was implemented to generate pulse energy levels sufficient for typical laser diagnostic techniques. The utility of the system was demonstrated by two-photon detection of oxygen atom in counter-flow flames [21] by our research partners at Purdue University (Prof. Robert Lucht, Aizaz H. Bhuiyan, and Dr. Sameer V. Naik) and it was determined that it may

have advantages over previous techniques that we have utilized (i.e. Rayleigh scattering) for characterizing flow fields such as those resulting from laser-induced optical breakdown.

The laser system consists of an optical parametric generator (OPG) followed by three stages of dye amplification. An

OPO/PDA system, as shown in Fig 17, has been setup to perform NO PLIF measurement in the flow field generated by laser induced optical breakdown. A complete description of the OPO/PDA system has been described previously by Bhuiyan et al. [23]. In the OPO stage, two counter-rotating beta-barium-borate (β -BBO) crystals are used. Two flat mirrors on either side of the crystals form the feedback cavity. The BBO crystals are pumped using 125 mJ/pulse of the third harmonic output (355 nm) of an injection-seeded Nd:YAG laser. A continuous-wave distributed feedback (DFB) diode laser is used to seed the optical parametric process at the idler wavelength near 1630 nm. The signal from the optical parametric process is generated near 452 nm and the output energy is 0.5 mJ/pulse. The 452-nm signal beam is amplified using two stages of pulsed dye amplification (PDA) which are. In each dye amplification stage, Coumarin 460 laser dye dissolved in methanol is pumped by \sim 130 mJ/pulse of the third harmonic output (355 nm) of the same Nd:YAG laser. The signal beam is amplified to \sim 6 mJ/pulse after the first stage of dye amplification and to \sim 13 mJ/pulse energy after the second stage. The signal beam from the OPO/PDA system is then frequency-doubled using another β -BBO crystal inside an Inrad Autotracker II to generate \sim 1 mJ/pulse UV radiation near 226 nm for exciting NO transitions in its A-X (0,0) electronic system. A sheet of 226-nm UV light is formed using a diverging cylindrical lens and then the sheet is focused using a converging spherical lens in the measurement region. The frequency of the UV beam can be tuned by changing the temperature of the DFB. The spatial and spectral characteristics of the 452 nm radiation were determined

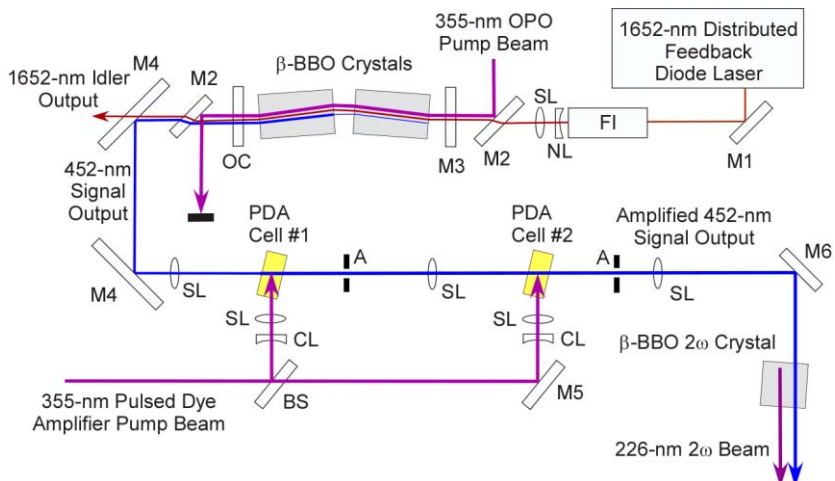


Fig 17. Injection-seeded optical parametric oscillator/pulsed dye amplifier (OPO/PDA) system to generate laser radiation near 226 nm for NO PLIF.

using a confocal cavity spectrum analyzer (Burleigh Model SA^{Plus}) having a free spectral range of 2 GHz and a finesse of 200. The spectral linewidth is found to be \sim 250 MHz which is nearly constant when tuning the idler wavelength.

An aluminum gas cell with an internal cavity of 2 inch diameter was built, as shown in Fig 18. The cell has optical access from all six sides. Fused silica windows are mounted on five sides of the cell and the remaining side is equipped with a 40-mm focal length converging spherical lens so as to generate plasma by focusing the second harmonic (\sim 532 nm) of another Nd:YAG laser. The inlet and the outlet ports for the gas are located at the bottom corners of the cell. Before each experiment, the cell is filled with 500 ppm NO in buffer nitrogen. The NO fluorescence signal is collected perpendicular to the laser sheet through the top window of the gas cell. Two 248-nm dichroic mirrors are used before detecting the LIF signal using an intensified camera so as to eliminate Rayleigh scattering and emission from the plasma. A Princeton Instrument intensified CCD camera with a coastal optics UV lens is used to collect the LIF signal. The camera and the two Nd:YAG lasers are synchronized by using a Stanford

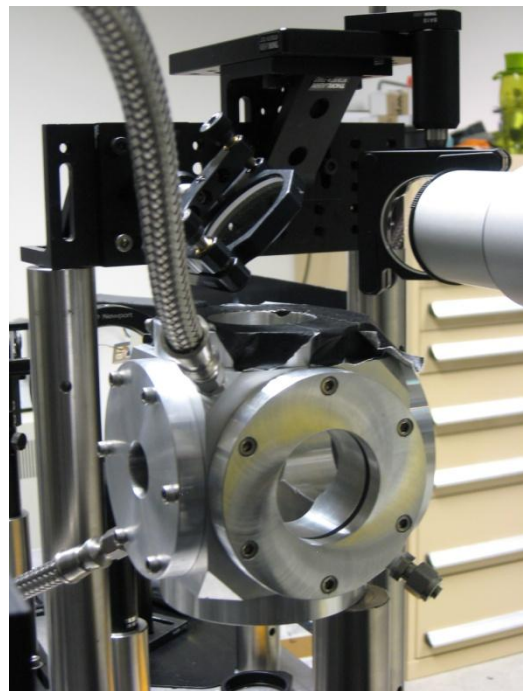


Fig 18. The gas cell equipped with fused silica windows on five sides and a focusing lens on the left side used to generate the laser induced optical breakdown.

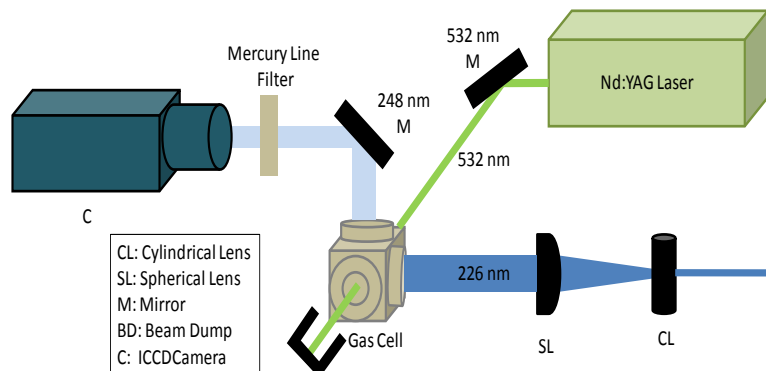


Fig 19. Experimental arrangement showing plasma generation using Nd:YAG laser, PLIF imaging and detection system.

Research Systems delay generator. Plasma generation and image acquisition arrangement is shown in Fig 19.

NO PLIF images were captured at different UV wavelengths by tuning the idler wavelength of the OPO by variation of the temperature of the DFB laser. For each wavelength, an average of 50 images was taken. A background image was taken by blocking the UV light and was subtracted from the signal image. A gate length of 500 ns was used on the intensified CCD camera to reduce the scattered light and emission from the spark. Images were captured at 10 μ s and 15 μ s after the initiation of the laser spark. Sample images at 10 μ s and 15 μ s delays are shown in Fig 20. The plasma emission is very bright even after transmission of the visible wavelength parts of the emission through two 248-nm dichroic mirrors. The plasma emission was eliminated to a considerable level by using a Semrock Mercury line filter (Hg01-254-25) so that the fluorescence signal from the entire area can be obtained. From the PLIF images in Fig 20, a circular region of higher intensity fluorescence is evident. This is due to the pressure rise across the blast wave generated from the laser-induced plasma. It is also evident that the diameter of the shock wave in Fig 20 (b) is higher than that in Fig 20 (a), which indicates the propagation of the shock wave. The speed of the shock wave can be determined from the displacement of the wave since the time for displacement of the shock wave is accurately known. The speed of the shock wave calculated from Fig 20 is 400 m/s for the 17 mJ pulse.

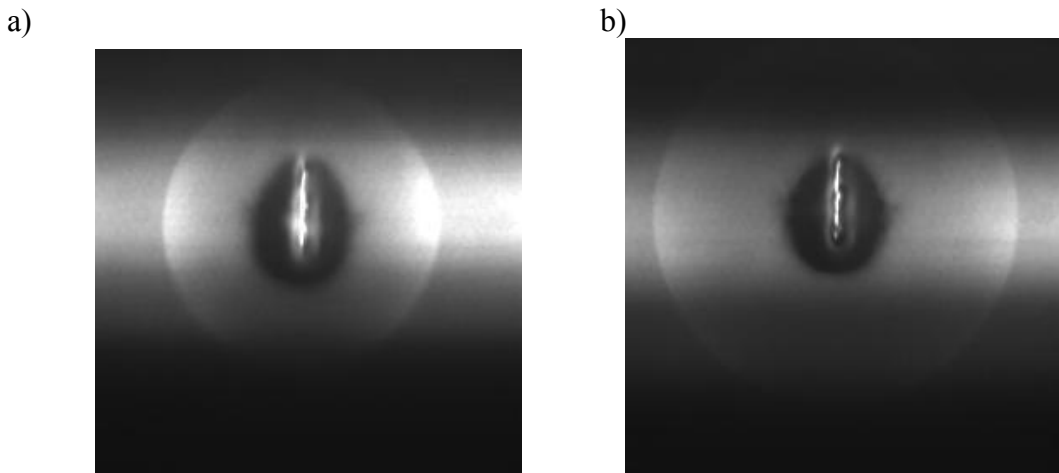


Fig 20. PLIF images of NO captured with a delay of (a) 10 μ s, and (b) 15 μ s after the initiation of laser spark.

The temporal evolution of the plasma is shown in Fig 21. Each image is the average of 50 instantaneous images and results in an excellent signal-to-noise ratio showing the details of the flow progression, while still imaging the emission from the initiating plasma and laser due to the effectiveness of the Mercury line filter. In this case, the plasma was generated by depositing 100 mJ/pulse of laser energy. Glumac et al. [17] have reported the maximum temperature of nearly 4100 K in the heated region around the spark. The concentration of NO in that region decreases significantly at high temperature causing the corresponding decrease in the fluorescence signal level. Therefore, the heated regions in Fig 21. appear to be darker than the outside regions since the density of NO in these regions is higher. The darker regions in Fig 21 indicate the presence of high-temperature plume at different times. In all these images, the plasma-generating laser beam is propagating from top to bottom. It may be noticed that the blast wave has propagated out of the field of view at the end of 25 μ s. As time progresses, the plasma induces fluid motion opposite to the laser propagation direction as described by Dors et al [24].

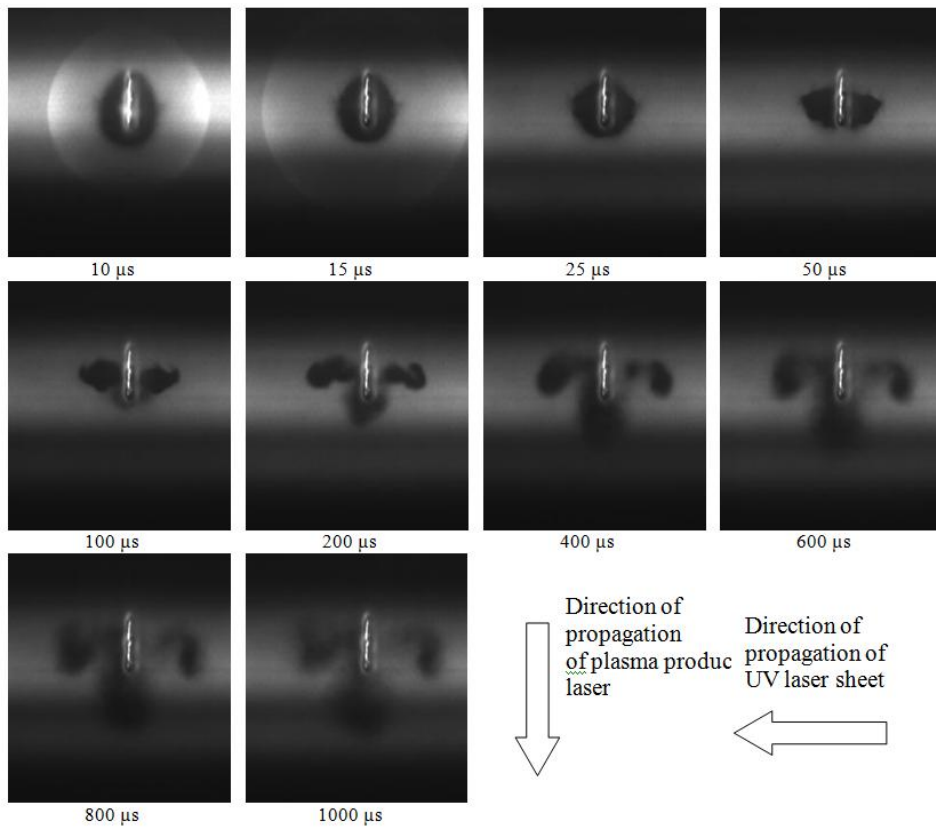


Fig 21. Temporal evolution of the heated plume inside the laser generated plasma. The time delays are shown below each image.

This fluid is ejected as a jet which propagates through a ring vortex. After 50 μ s, there are two separated heated region which indicates jet propagation and vortex formation. Formation of vortices is more evident near 100 μ s; the vortex ring propagates in the direction of laser propagation. The growth of the vortex ring diameter slows beyond 200 μ s.

The sequence of fluorescence images generated by tuning the UV wavelength over the $P_2(12)$ line of NO are shown in Fig 22. The UV frequency was tuned between 44094.25 cm^{-1} and 44098.43 cm^{-1} . The exact wavelength for each image is listed at the bottom of each image. From Fig. 22, it is clear that the fluorescence signal intensity varies over the NO absorption line. The maximum signal intensity is found near 44096.5 cm^{-1} , which is the center of the $P_2(12)$ transition of NO. Depending on the relative position of the laser wavelength relative to the NO absorption line the flow after the shock wave appears darker or brighter than the ambient conditions due to the thermodynamic changes in the flow. This suggests that the thermodynamic

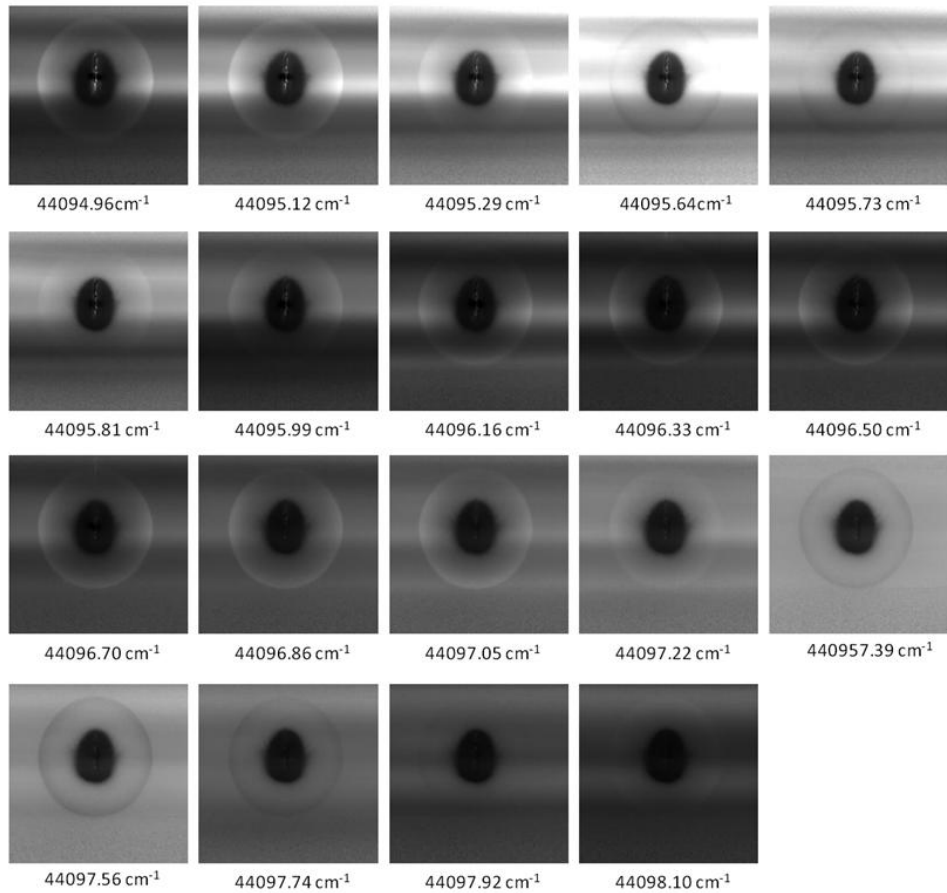


Fig 22. Sequence of NO PLIF images in the laser-produced plasma when scanning the DFB frequency over the $P_2(12)$ transition of NO.

properties (i.e. pressure and temperature) may also be able to be calculated using the NO-PLIF technique as has been described by Naik et al. [7], going beyond the flow visualizations shown here, but improvements are still needed in the data (i.e. variation and stability of the laser intensity distribution in the illuminating sheet) and modeling of the signal to be able to take this next quantitative step.

3. LOCAL FLOW CONTROL OF SUPERSONIC CAVITY FLOWS

As an application to plasma flow control, two different flow types were investigated; the first being a cavity flow. Although flow over a cavity represents a basic fluid dynamic configuration, this intrinsically simple arrangement can produce a number of complex flow field characteristics (e.g. shear layer instability, flow-induced acoustic resonance, vortex flow, shock/expansion wave interaction, etc.). Consequently, the presence of these features can result in significant changes to the surroundings external and internal to the cavity, such as in pressure, noise, and the convective heat transfer environment. [25] [26] While this phenomenon alone appropriately distinguishes this topic as one of fundamental interest to the discipline of fluid dynamics, the common occurrence of cavity-like geometries (e.g. wheel wells, grooves, etc.) in a wide range of tangible applications has underscored the importance of understanding its underlying physics and control. As a result, what began as a topic of scientific inquisition in the 1950s has evolved into an extensive experimental, analytical, and computational research effort.[7] Currently, two active areas of investigation in cavity flows are related to aircraft store release and combustion arrangements in proposed scramjet engines.

Inherent to all scramjet engines are the challenges of fuel injection, ignition, and flame holding as parts of the combustion process in a high-speed flow. Particular difficulties are rooted in the fuel injection method which must provide sufficient fuel-air mixing in an environment with limited flow residence time in the combustor and adverse compressibility effects.[27] Moreover, for sustained supersonic combustion a stable region for flame holding must exist under a wide range of operating conditions. As a proposed solution, in recent years the use of a cavity-based flame holder in the wall of a scramjet combustion chamber has been suggested as an integrated approach to overcome many of these design challenges. A cavity can optimize the mixing rate through flow recirculation, which can be enhanced by the induced periodic shedding

of coherent structures into the shear layer.[28] [29] The application of a cavity flow field for improved fuel-air mixing in a scramjet engine is of particular interest to the current investigation. With this effort, results will be presented demonstrating the use of pulsed energy deposition as a strategy for mixing enhancement. Specifically, it will be shown that the shear layer spanning a cavity can be optimized through the forcing of coherent structures, thereby increasing the fuel-air mixing capabilities of the flow field.

In general, a cavity flow field can be broadly categorized into two basic flow regimes depending primarily on its streamwise length-to-depth ratio (L/D). The significance of this parameter is revealed in its ability to predict whether the flow field in the cavity will be in an open or closed configuration, although other transitional states may occur. A schematic illustrating both flow arrangements

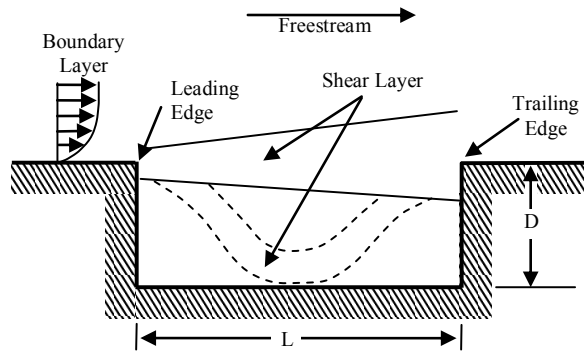


Fig 23. Schematic of cavity flow field operating in an open (solid line) and closed (dashed line) configuration.

is shown in Fig 23. Apparent in all flows over a cavity is the presence of a shear layer which develops out of the boundary layer behind the leading edge of the cavity and is sustained by the velocity difference between the freestream and the flow inside the cavity. However, in the closed configuration, identified by a shallow cavity with an $L/D > 10 - 13$, the shear layer is unable to bridge the entire length of the cavity and rather attaches to the bottom wall before reaching the trailing edge. [29] In this configuration, the flow is generally steady and the pressure distribution along the cavity floor consists of a strong adverse gradient which can result in large drag losses as well as be detrimental to other performance attributes, such as heat transfer. In this configuration, the flow is generally steady and the pressure distribution along the cavity floor consists of a strong adverse gradient which can result in large drag losses as well as be detrimental to other performance attributes, such as heat transfer. [25] [26] Conversely, in the open configuration the shear layer spans the entire length of the cavity and reattaches near the trailing edge forming a single recirculation region below it. This type of flow is typically unsteady due to the susceptibility of instabilities in the shear layer. Consequently, for the compressible flow case intensive noise radiation and large shock motion can develop.[25] Open cavity flows are associated with deeper cavities, identified by an $L/D < 7 - 10$. As with the

closed configuration described above, the ambiguity in the critical limits of the transition between the open to closed arrangements is due to a slight dependence on other flow parameters, including boundary layer thickness, freestream Mach number, and cavity width. [29]

A cavity in the open configuration can also exhibit either transverse (normal to the streamwise direction) or longitudinal (parallel to the streamwise direction) pressure oscillations. [30] For the case when the L/D is on the order of unity, self-sustained pressure oscillations form in the transverse mode. In short, this occurs as a result of a single vortex (formed out of shear layer instabilities) within the cavity entraining mass from the freestream and compressing the gas beneath it. This increased pressure environment ejects the vortex into the freestream flow; a new vortex is then shed from the cavity leading edge, closing the feedback loop.[31] Open cavities with an L/D approximately greater than unity oscillate in the longitudinal mode. There are primarily two similar, but distinct models to describe the mechanism for the longitudinal oscillations. For both models, the shear layer impinging the cavity rear wall causes an inflow of freestream mass and momentum at the trailing edge. As a result, the pressure within the cavity increases and an acoustic wave develops that propagates upstream at the local sound speed. In the first model, as the acoustic wave impacts the cavity front wall the formation of small vortices are induced at the leading edge. These vortices grow as they convect downstream, which due to instabilities, leads to upward and downward deflections in the shear layer. In the second model, the reflection of the acoustic wave at the cavity front wall (rather than vortex shedding) causes the shear layer deflection. The feedback loop is closed when the shear layer deflection reaches the cavity trailing edge and the mass added at the beginning of the loop is ejected.[29]

The frequencies (f) that the longitudinal oscillations occur are expressed in terms of the nondimensional Strouhal number (Sr) which is based on cavity length and freestream velocity (U_∞):

$$Sr = \frac{fL}{U_\infty}. \quad (13)$$

The first attempt at developing a model for predicting the resonant frequencies of the cavity oscillations was undertaken by Rossiter [32] in 1964. Through experiments carried out in subsonic and transonic flows he developed a semi-empirical equation that assumed a coupling between acoustic radiation and vortex shedding; specifically, acoustic radiation induces vortex

shedding at the cavity leading edge and the propagation of vortices over the trailing edge of the cavity causes the acoustic radiation. With these assumptions, the fluid mechanic frequency of the vortex shedding is then equal to the acoustic frequency:[33]

$$Sr_m = \frac{m - \alpha}{1/k_c + M_\infty}, \quad (14)$$

where Sr_m and m are the nondimensional frequency and mode of oscillation, M_∞ is the freestream Mach number, k_c is the ratio of the convective velocity of vortices in the shear layer to the freestream velocity, and α is the phase delay between the impact of the acoustic wave at the cavity front wall and the formation of a new vortex.[30] Consequently, this semi-empirical formula allows the oscillatory mode frequencies to be calculated through a combination of empirical values for α and k_c , and known values for the remaining flow parameters. However, it should be noted that although the most commonly used values for α and k_c are 0.25 and 0.57, their universal acceptance amongst researchers is currently a topic of much debate. [33] [29] [30] For example, in a review of previous experimental investigations, Unalmis et al.[33] report that measurements spanning the Mach numbers of 0.4 – 2.5 have resulted in values of k_c ranging from 0.5 through 0.75. In addition, there are still no simple means of determining which modes will dominate and what their respective amplitude will be.[30] Rossiter's formula [Eq. (14)] was also modified in 1975 by Heller and Bliss [34] such that the sound speed in the cavity would account for temperature recovery in the flow. The modified formula is as follows:

$$Sr_m = \frac{m - \alpha}{\frac{M_\infty}{\sqrt{1 + (r/2)(\gamma - 1)M_\infty^2}} + \frac{1}{k_c}}, \quad (15)$$

where r is the temperature recovery factor, γ is the ratio of specific heats, and the other parameters are as described in Eq. (14).

Compressible turbulent shear layers have also been studied independent of the cavity flow field for a number of years. The fundamental interest in this phenomenon was originally motivated by an observed decrease in the growth rate of the shear layer with increasing Mach number as one of the freestreams becomes supersonic.[30] first attempt at explaining this effect was by Brown and Roshko [35] who initially investigated the effect of density changes (which

are present in shear layers with two different Mach numbers) by experimentally varying the density ratio across a subsonic shear layer by using two streams of different gases. As a result, they observed a first-order reduction in the growth rate of the shear layer.[36] In relation to high-speed flow conditions, the Mach number difference across the shear layer develops a similar density variation and the compressibility effects directly account for a growth rate that is less than accounted for by the density variation alone. The investigation by Brown and Roshko[35] also clearly revealed the presence of coherent large-scale structures that develop in the shear layer; consequently, they are often referred to as “Brown and Roshko” structures. Through this discovery and the realization that they are related to the instability of the shear layer, the idea of developing a coordinate system based on the motion of large-scale structures was later introduced by Papamoschou and Roshko.[37] Specifically, the coordinate system relates to a reference frame moving with a convective velocity (U_c), defined as the velocity of dominant coherent structures. Within this convective frame of reference moving with a respective convective velocity, Papamoschou and Roshko [37] characterized a large-scale structure in the shear layer as consisting of a common stagnation point between the high and low speed streams. By then considering the two streamlines from each freestream, this led to the formulation of a pressure boundary condition, allowing the convective velocity to be calculated and a convective Mach number (M_c) to be determined. Accordingly, the convective Mach number defined by Papamoschou and Roshko [37] for two freestreams with the same specific heat ratio is given by:

$$M_c = \frac{U_1 - U_c}{a_1}, \quad (16)$$

and the convective velocity is given by: [30]

$$U_c = \frac{a_1 U_2 + a_2 U_1}{a_1 + a_2}, \quad (17)$$

where U_1 and U_2 are the velocities of the high-speed and low-speed streams, and a_1 and a_2 are each of the streams corresponding sound speeds. However, it should be noted that modified

forms of the convective Mach number have been developed to account for recompression shocks that may be present in the shear layer under high-compressibility conditions.[30]

From Eq. (17), the convective velocity of the shear layer over a cavity can be calculated. Following the work of Murray et al., which was based off of earlier studies by Rossiter [32] and Heller and Bliss,[34] the velocity of the fluid of the low-speed stream is neglected ($U_2 = 0$). Also, adiabatic temperature recovery was used by setting the temperature of the fluid within the cavity to be equal to the stagnation temperature. Thus, Eq. (17) yields an expression for the convective velocity ratio for the cavity flow, which is given by:

$$k_c = \frac{1}{\frac{a_1}{a_2} + 1} = \left(\frac{1}{\sqrt{1 + \frac{\gamma-1}{2} M^2}} + 1 \right)^{-1}, \quad (18)$$

In the current investigation, convective velocities predicted with Eq. (6) will be compared to those from experimental results.

With a wide range of tangible applications, the practical interest of controlling the characteristics of a cavity flow field has led to the investigation of a number of novel approaches. Although flow control techniques can be classified in several different ways, in general, two main categories exist: passive and active excitation. Passive excitation methods utilize a permanent change to the flow field, either through a geometric alteration to the cavity or by a mounted obstruction in the flow. Methods within this category are typically inexpensive and simple and can be employed through a variety of mechanisms, such as with spoilers, vortex generators, or by slanting the rear wall of the cavity to force a modification in the shear layer reattachment process.[29] Of particular interest to the current study is the application of these devices to counteract the observed decrease in the growth rate of the shear layer with increasing compressibility. In experiments performed by Island et al.[38] boundary layer disturbances were introduced by applying small pieces of Scotch tape to the high-speed (supersonic) side of a splitter tip. Different geometric parameters for the disturbances were also investigated which included changing their shape, number used, spatial distribution and location, surface texture, and thickness. Planar laser Mie scattering images and schlieren photography demonstrated that discrete three-dimensional disturbances increased the near- and far-field growth rate, with

enhancements of up to 45%. This was also presented with quantitative mixing measurements using cold chemistry planar laser-induced fluorescence. Results from this diagnostic revealed up to a 7% increase in the mixing efficiency. When coupled with the increased thickness of the shear layer this led to about 57% more mixed fluid than for the unperturbed case at the same compressibility. However, while this study, as well as many others, has demonstrated the effectiveness of passive excitation methods because these devices are permanent features they are generally limited as they typically can only be optimized for a specific flow condition. Consequently, performance can degrade to conditions worse than for the unforced case. [4]

In contrast, active excitation methods can continuously change and adapt to different flow conditions. Broadly speaking, forcing techniques of this type include acoustic driving, mechanical excitation, and fluid injection methods. [20] In relevance to cavity flow fields, the use of steady or pulsating microjets has acquired particular interest as a means of active flow control. In addition to being effective at controlling the cavity oscillations, this technique is advantageous as it is small, robust, and capable of producing a high momentum flux with a very small mass flux. [7] As an experimental example, Zhuang et al. [39] investigated the use of supersonic microjets at the leading edge of a Mach 2 cavity with an $L/D = 5.19$. The study concluded that the activation of the microjets resulted in up to a 20 dB reduction of amplitudes in cavity tones and more than 9 dB in the overall sound pressure levels. The injected mass also led to modifications in the shear layer and a significant reduction of the flow unsteadiness inside the cavity. There have also been a number of computational investigations. Rizzetta and Visbal [40] numerically studied the application of high frequency (5 kHz) forcing through pulsed mass injection at the leading edge of a cavity with an $L/D = 5$ and at Mach 1.19 to investigate the ability of large-eddy simulations to predict acoustic resonance suppression. They found that the perturbed shear layer resulted in several changes in comparison to the unforced case, including acoustic suppression, altered characteristics of vortices, and a decreased amplitude of vertical shear layer deflections.

While these types of mechanical devices have shown to be effective, there are several disadvantages associated with them. In particular, with devices such as blowing/suction jets, there are inherent challenges with installation and concerns with reliability and performance under extreme conditions such as icing or trapped debris.[8] Accordingly, in recent years there has been a renewed interest in the use of energy deposition for high-speed flow control. The scope

of this research activity encompasses a wide range of approaches (e.g. plasma arcs, pulsed lasers, microwaves) for use in practical applications, including: drag reduction, lift and moment enhancement, and in forcing modifications to shock structures.[9] [10] A selective review of using energy deposition as a means of aerodynamic flow control at high-speed is given by Knight. [10] In a related computational study, Aradag et al.[41] numerically examined the use of pulsed energy deposition to reduce the resonant pressure fluctuations in a cavity with an $L/D = 5.07$ and at Mach 1.5. A periodic pulsed input of 1.0 mJ was applied to the leading edge of the cavity to simulate energy deposition by a laser. The input was added at the beginning of each fundamental Rossiter period. Their simulation indicated that the applied forcing induced a reduction of the pressure fluctuations for the first several Rossiter modes, changing the flow structure within the cavity.

In the present experimental investigation, energy deposition will be similarly introduced to the leading edge of a supersonic cavity through the use of a pulsed laser. However, the forcing will be applied at a relatively low frequency of 10 Hz to provide a single burst of excitation to the shear layer spanning a cavity. The effectiveness of this technique will be determined by its ability to enhance the large-scale structures that develop in the shear layer to improve fuel-air mixing capabilities of scramjet engines. This experimental investigation is part of an ongoing joint research program with research colleagues at Rutgers University who have previously reported on computer modeling efforts for this type of flow field.[41]

3.1. Experimental Arrangement for Cavity ELFC Experiments

In the current experimental study, the flow over a rectangular cavity was investigated utilizing a supersonic blow down wind tunnel. The tunnel was operated with good flow quality (i.e. in absence of strong compression or expansion waves in the test section) at a Mach number of 1.4. The flow field conditions were confirmed with ensemble averaged velocity measurements obtained from particle image velocimetry (PIV) data. An illustration of the streamwise velocity for the unforced

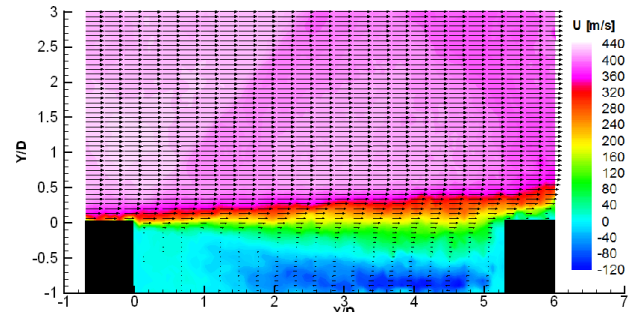


Fig 24. Streamwise velocity profile of entire cavity flow field obtained with PIV data

flow field is shown in Fig 24. Air was supplied through an Ingersoll-Rand compressor with a volumetric flow rate of 2040 m³/s and at a pressure of 1000 kPa. The flow from the compressor was filtered, dried, and cooled, and traveled to a 140 m³ tank farm. From this point, the air travels through a pipe to a pneumatic valve controlled by a Fisher TL 101 Process Controller and a manual gate valve prior to entering the wind tunnel. Before reaching the test section, the flow passes through a conventionally arranged settling chamber with a honeycomb filter and subsequent screens to reduce the scale of the incoming turbulence and to straighten and make the flow uniform. The cavity was located in the top wall of the wind tunnel test section, which has a square cross section measuring 63.5 mm on each side. The dimensions of the cavity were 71.9 mm long x 13.6 mm deep ($L/D = 5.29$) and spanned across the width of the test section. This arrangement forces the flow field in the cavity to be in the open configuration and creates longitudinal oscillations for experimental investigation. There are also large windows on each side of the test section to allow flow visualization studies to be conducted and a smaller window on the bottom to provide access for energy deposition into the flow field.[42] A full description of the wind tunnel can be found in Ref.[42]. Relevant flow condition parameters have also been summarized in Table 3. In Table 3, the convective Mach number was calculated with eqns. (4) and (6), which represents adiabatic temperature recovery in the cavity as used by other researchers.[30] For comparison, the convective Mach number was also calculated with the most commonly used value for temperature recovery, $r = 0.89$.[33] Under this condition the value varied only slightly with $M_c = 0.65$.

As a means of controlling the growth rate of coherent structures in the shear layer, pulsed energy deposition from a Quantel Brilliant series Q-switched Nd:YAG laser

was used as a form of excitation. The laser was operated at a wavelength of 532 nm, delivering approximately 230 mJ per pulse at a frequency of 10 Hz. The energy generated from the laser pulse was focused using a spherical lens and then expanded along the width of the cavity leading edge using a cylindrical lens. This optical arrangement resulted in a focused 25 mm spanwise

Table 3 Summary of experimental test condition.

Stagnation Pressure	200 - 235 kPa
Stagnation Temperature	27 - 34 °C
Boundary Layer Thickness	6.58 ± 0.1 mm
Cavity Length	71.9 mm
Cavity Depth	13.6 mm
Freestream Mach Number	1.4
Convective Mach Number	0.64

oriented “line” defining the excitation region. As a result, a single burst of excitation was introduced and ionized the flow before it propagated the length of the cavity.

Results from linear stability analysis and experimental measurements/observations indicate that for a compressible planar shear layer as the convective Mach number increases the flow becomes more three dimensional and the most amplified waves are oblique for convective Mach numbers above 0.6.[43] [44] This rise in the three dimensionality is important as it may impact the ability to force and control compressible mixing layers.[45] However, Murray and Elliott [30] suggest that for cavity flows the presence of two dimensional structures in the shear layer persists at higher Mach numbers (free stream Mach numbers up to 2.1). Also from linear stability theory Sandham and Reynolds [44] showed that in the convective Mach number range of the current study (~ 0.7) the most amplified wave may be oblique (at approximately 31° according to their formula), but the amplification appears to be relatively flat for lower disturbance angles based on their plot of amplification. Additionally based on our previous studies of flow control of shear layers using energy deposition for jets exhausting into ambient conditions it was found that positions near the exit (corner between the high speed flow and ambient) provides an excellent and possibly optimal position for excitation.[9] Therefore for the current study the location of the excitation pulse in the corner of the cavity was utilized and coupled with the geometry of the cavity restricted the study to using 2-D forcing.

As a first step in analyzing the effect of the pulsed plasma for local flow control, the resulting flow field was analyzed with a standard Z arrangement schlieren system. Illumination was provided by a Xenon spark lamp, which acted as a point light source providing high luminance and emitting a continuous spectrum of light, ranging from ultraviolet through visible to infrared. The generated light was then collimated through the wind tunnel test section and then focused to a point. Instantaneous schlieren images were recorded in the vertical and horizontal knife edge configuration with a 1600 x 1200 pixel CCD camera. The duration of each flash was on the order 20 ns and an imaging exposure time set at 1 μ s, which resulted in conditions short enough to freeze most of the turbulent structures and produce instantaneous images of flow.[39] All equipment was controlled with an 8-channel Quantum Composer pulse generator. A top down view of the experimental schlieren setup is shown in Fig 25 (a)

In addition, two-dimensional PIV measurements were conducted to obtain quantitative velocity fluctuation data. A schematic of the experimental setup used for obtaining the PIV images is shown in Fig 25 (b). The main flow was seeded with Di-Ethyl-Hexyl Sebacate (DEHS) through the use of a Laskin Nozzle that generated particles with a diameter less than 1 μm .[46] The seeding was introduced approximately 3.5 m upstream of the test section which resulted in a sufficient dispersion of the particles into the cavity and the freestream flow. The particles were illuminated by a thin (on the order of 0.1 mm) light sheet that spanned the streamwise length of the cavity at approximately the middle of the test section width. The light sheet was created by a dual-head New Wave Nd:YAG

laser in conjunction with spherical and cylindrical lenses. The PIV laser was operated at a frequency of 532 nm, with each pulse delivering approximately 40 mJ of energy. In order to avoid saturation of the CCD from intense reflections, the cavity surface was painted with a Rhodamine based fluorescent paint. As a consequence, (with about 30% efficiency) the wavelength of the light off of the cavity walls was increased from 532 nm to above 620 nm. By using a 532 nm band-pass filter on the camera, this allowed the particle signal to be picked up closer to the cavity walls. The time separation between the laser pulses to illuminate the DEHS particles was adjusted according to the flow velocity and camera magnification. The PIV images recorded were taken with the CCD camera as described above in the schlieren photography setup. The image pairs for each delay time and for the no forcing case were then processed and averaged through a PIV program developed by Innovative Science Solutions, Inc.

The accuracy of velocity measurements obtained from the PIV data was a composite of the ability of the seed to follow the flow and for the imaging and analysis system to record and

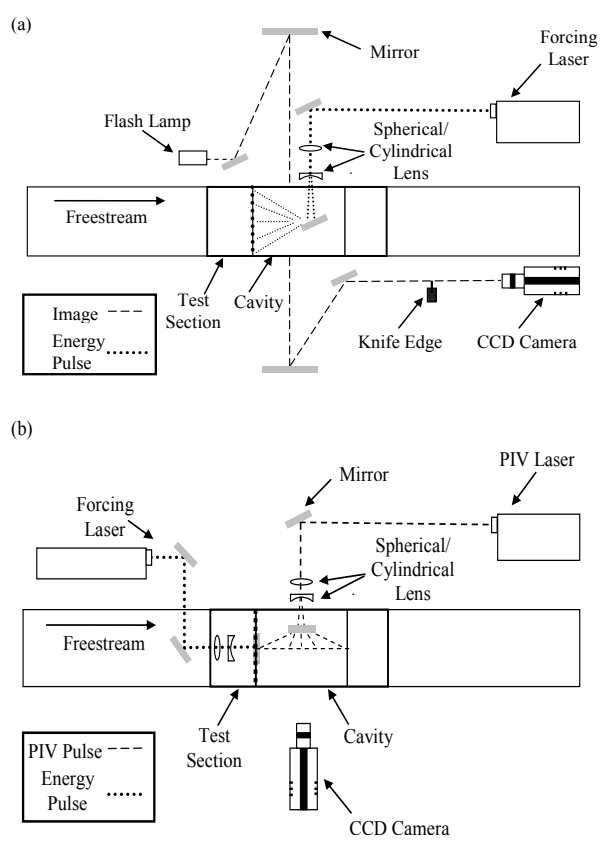


Fig 25. Schematic of flow visualization setups: (a) schlieren and (b) PIV

process a field of particle images.[47] In quantifying the accuracy a number of factors need to be considered, such as the number of samples, turbulence intensity, computational algorithm, equipment, and particle size.[39] The error in timing between two laser pulses was estimated to be 6 ns. The uncertainty in pixel displacement by correlation analysis of the PIV software program was approximated at one-tenth of a pixel, assuming the laser sheet is providing Gaussian illumination. Subpixel accuracy was achieved by matching the intensity captured from illuminated particles through a Gaussian shaped peak locator.[48] With these assumptions and using an ensemble average of 340 image pairs, a relative error of 2.5% was calculated for the mean velocity. For the freestream flow, the PIV measurements were less than 2% of the values predicted with 1-D gas dynamic equations. A similar comparison of measured and expected values for velocities within the cavity and shear layer could not be evaluated because these values were not known *a priori*.[39] Also, consideration of seed-particle dynamics was especially important since the large velocity gradients present challenge the flow-following capability of all but the smallest particles and spatial variations in density make it difficult to establish uniformly satisfactory seeding levels. Particle dynamic effects are typically parameterized by the Stokes number (St), which is the ratio of the characteristic particle time to the time scale of the flow variations to be measured.[47] Following the work of Scarano and Oudheusden,[49] given the relatively low Mach and Reynolds numbers for this study, the drag relation suggested by Melling [50] was used to determine the characteristic particle time. The flow time scale in the shear layer was be calculated from the work of Samimy and Lele [51] This yielded, immediately downstream of separation, a worst-case Stokes number of $St = 0.024$. The response of the particles to turbulent fluctuations in the shear layer was then quantified using the results from Samimy and Lele [51] which predicted a maximum RMS velocity fluctuation error, due to particle lag of approximately 0.35 %.[52] Further downstream, the growth in the shear layer thickness drops the Stokes number below 0.013, reducing the particle lag error to 0.1 %.

3.2. Schlieren Images for Cavity ELFC Experiments

Preliminary schlieren measurements from previous work indicated that ELFC may be an effective means to control the formation of large scale structures in the shear layer created above the cavity. As a first step in the more detailed investigation (i.e. utilizing particle image velocimetry) of this flow field during the present study, instantaneous schlieren images were

obtained to investigate the distribution of density gradients within the cavity flow field before and after excitation. The experimental study was conducted at incremental delay times ranging from $10 - 1000 \mu\text{s}$ ($\pm 1 \text{ ns}$) from the laser energy input at the cavity leading edge. At each delay time and for the no forcing case, 138 instantaneous images were collected and phase averaged. Although the cavity flow field was investigated with the knife edge in the horizontal and vertical arrangements, only images in the vertical orientation are presented. The images in the vertical arrangement were selected because of the suppression of the vertical density gradients due to the shear layer and boundary layer. As a result, large-scale structures within the shear layer are more easily visualized.[30]

Shown in Fig 26, phase averaged schlieren images are illustrated for selected delay times from the excitation pulse and also without any forcing. The direction of the flow is from left to right. Apparent in all the images, an oblique shock can be seen at the leading edge of the cavity. An expansion or compression wave is similarly seen at the trailing edge. The images also resolve the reflection of the leading edge shock off of the bottom wall of the test section and its subsequent impact with the trailing edge wave. Several other weaker waves can also be identified. These were formed from minor surface discontinuities in the test section walls and are common in most supersonic wind tunnel facilities. Their presence did not appear to influence the results presented in any significant manner. In image (a) the flow field is shown without any applied excitation. As discussed earlier, the dynamics of cavity flow fields are dominated by a feedback mechanism, consisting of instability waves or shear layer structures in one leg and acoustic waves on the return.[39] Therefore, while dominant cavity tones were expected, the phase-conditioned data was not measured with respect to them. Accordingly, in image (a), no large-scale structures are evident due to their decreased coherence and random occurrence. Image (b) corresponds to a $10 \mu\text{s}$ delay from the excitation pulse. In this image, the blast wave from the laser pulse originates at the leading edge and is distorted by the relative velocity internal and external to the cavity. At this point the disturbance has not significantly propagated through the flow and the shear layer remains primarily unaltered. In images (c) and (d), the delay time between excitation and imaging was increased to $20 \mu\text{s}$ and $40 \mu\text{s}$, respectively. At these increased times, the disturbance from the laser pulse, which first appeared as a single thermal spot, has traversed through the shear layer to considerably alter the flow field.

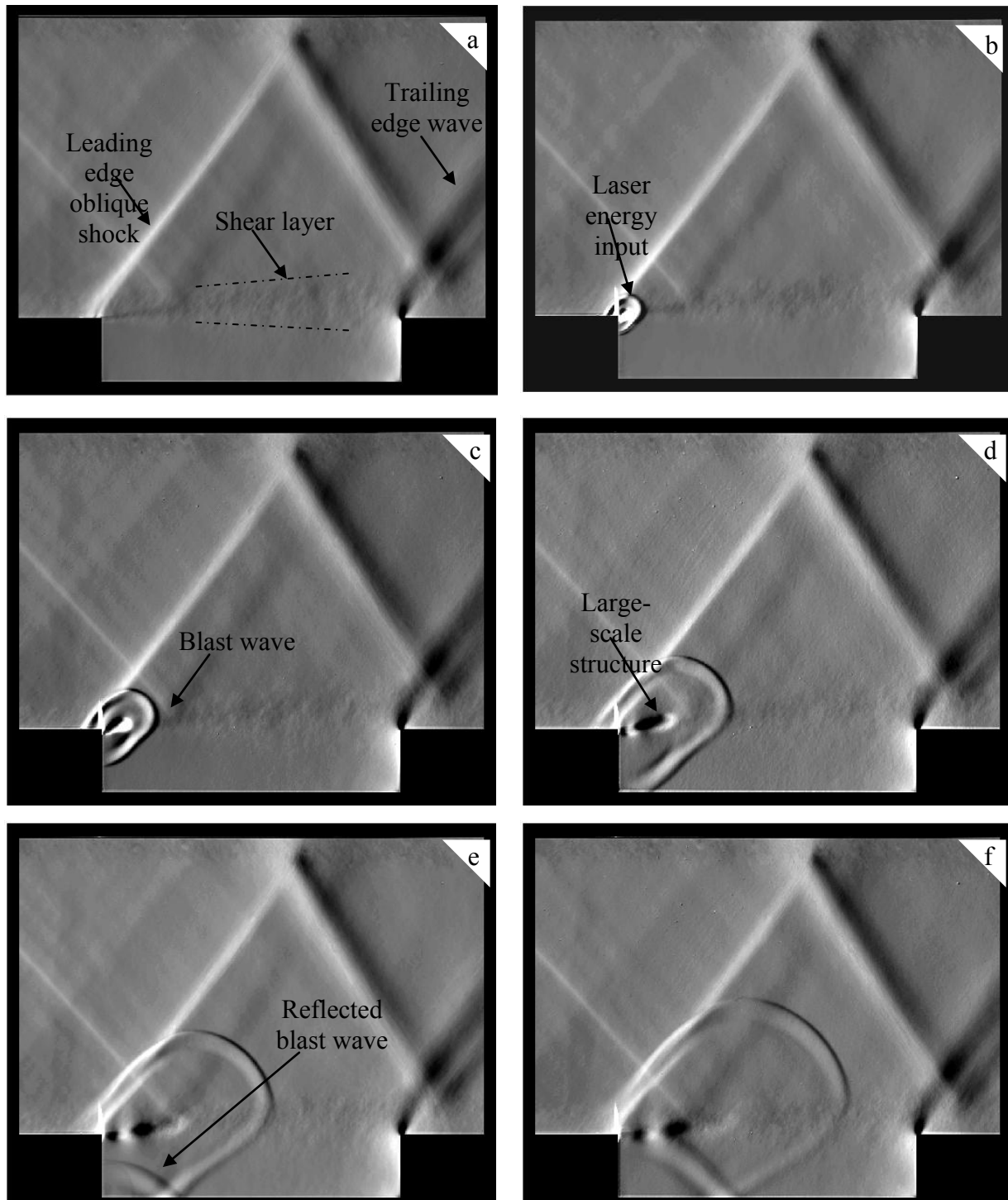


Fig 26 Phase averaged schlieren images without forcing (a) and at selected delay times from an energy input: (b) 10 μ s, (c) 20 μ s, (d) 40 μ s, (e) 60 μ s, and (f) 80 μ s (cont. on next page)

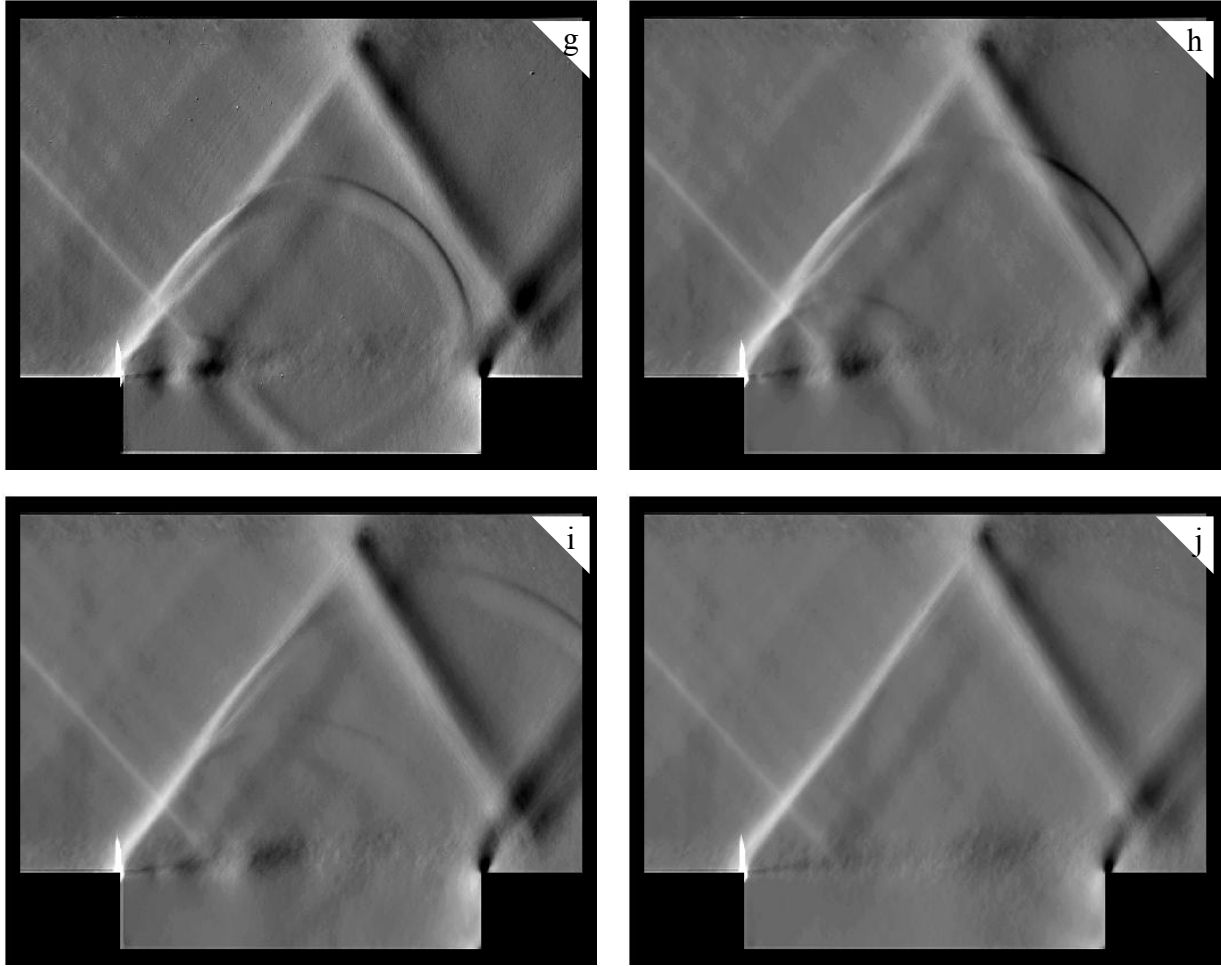


Fig 26 cont. Phase averaged schlieren images at selected delay times from an energy input: (g) 100 μ s, (h) 120 μ s, (i) 160 μ s, and (j) 240 μ s.

Specifically, in image (c) a neighboring pair of light and dark regions (centered approximately in the wake of the blast wave) can be identified. A second similar pair of regions can also be seen forming in the shear layer image in (d). While the schlieren images provide no further qualitative information towards the nature of these induced regions, the shadow pattern suggested a density variation distribution and location that was consistent with the presence of a large-scale structure within the shear layer. Since these results are qualitative in nature, one goal of the present investigation was to give a more detailed description of this flow field using two-component velocity field measurements obtained using PIV. Through the velocity data it will be shown that the structure consists of two vortices with a common stagnation point between them; therefore, having a comparable appearance and behavior to the model proposed by Papamoschou and Roshko.[37] Shown in the remaining images (e) through (j), for increasing delay times the

large-scale structure (both proposed vortices) convects, grows, and decays as it moves further downstream.

In addition to the formation of the large-scale structure in the shear layer, the images in Fig 26 also illustrate the propagation of the blast wave through the cavity flow field. Associated with this event is the reflection of the blast wave off of the cavity bottom wall which results in a reflected wave, forming a second disturbance to the shear layer. The reflected wave can first be seen in image (e). In this image, 60 μ s have elapsed from the energy input and the reflected wave is propagating toward the underside of the shear layer. The resulting impact is shown in images (f), (g), and (h). In contrast to the initial wave, the reflected wave appeared to transverse through the shear layer while leaving it primarily unaltered. Although this phenomenon was not directly investigated, images (f), (g), and (h) suggest three possible explanations. First, with increasing time the energy of the blast wave is being distributed over a greater arc length and dissipated by flow field motions, reducing its local intensity. As a result, the reflected wave may have been too weak to provide a sufficient disturbance to alter the shear layer. Secondly, the reflected wave obliquely impacts the bottom of the shear layer and then propagates across its thickness. This differs from the initial wave that spans the entire shear layer thickness and transverses along its length. Lastly, as shown in images (f), (g), and (h) the reflected wave impacts the section of the shear layer containing the large-scale structure. While the interaction between these features is not clear, the presence of the structure may have suppressed any affects from the reflected wave.

3.3. Particle Image Velocimetry for Cavity ELFC Experiments

Particle Image Velocimetry (PIV) was conducted to determine the two-component velocity field and provide detailed quantitative information on the large-scale structure that formed in the shear layer from the energy deposition at the cavity leading edge. Ensemble averages of 340 image pairs were used for the analysis of all conditions tested. The results are presented as color contours for the average transverse and streamwise velocity components and for a selected region of the cavity flow field. This region was chosen to show key attributes of the flow; this included the propagation of the blast wave through the shear layer and the subsequent formation and development of the large-scale structure. For all of the velocity data presented, the axes of

the images were nondimensionalized by the cavity depth. Also, for streamwise locations the selected view was positioned such that the full length of the x-axis directly corresponds to the full cavity length. Consequently, the upstream wall of the cavity is located at $X/D = 0$, while the downstream wall is at $X/D = 5.29$. Along the y-axis, negative values of Y/D identify locations within the cavity, while positive values are those within the freestream. Therefore, using a conventional format for coordinates $(X/D, Y/D)$, the cavity leading edge is located at $(0, 0)$, the cavity trailing edge at $(5.29, 0)$, and the cavity bottom wall for all values of X/D with $Y/D = -1$.

3.3.1. Transverse Velocity component

In Fig 27, the average transverse velocities are shown for selected delay times from the energy input, ranging from $40 \mu\text{s}$ to $240 \mu\text{s}$ ($\pm 1 \text{ ns}$) and also without excitation. Apparent in all the images of Fig 27, the leading edge oblique shock can be identified as a velocity field boundary in the upper left corner. The shear layer is also shown by the region of decreased transverse velocity along the streamwise direction for $Y/D = 0$. A baseline illustration of the flow field without any forcing applied is shown in image (a). Consistent with the phase averaged schlieren images, no organized motions within the shear layer can be identified.

In image (b), $40 \mu\text{s}$ have elapsed from the excitation pulse. The resulting blast wave is shown by the band of sharp velocity change that is approximately centered about the cavity leading edge [i.e. $(X/D, Y/D) = (0, 0)$]. In the wake of the blast wave, induced vertical motions in the flow field (internal and external to the cavity) can be seen. These vertical motions are especially significant in the wake of the blast wave entering the cavity. The initial development of the large-scale structure illustrated in the schlieren images can also be seen forming in image (b) at the cavity leading edge. In this case, the structure is first identified as a coherent region of increased positive transverse velocity; for clarity, this region is boxed in dashed lines in image (b). In image (c), $80 \mu\text{s}$ have elapsed from the energy input. At this delay time, the boxed region of positive transverse velocity identified in image (b) has propagated away from the cavity leading edge and undergone considerable growth. Additionally, a second region of negative transverse velocity can be seen forming at the upstream end of the image. Image (c) also illustrates the development of the reflected blast wave within the cavity. The flow field following its impact with the reflected wave and shear layer is shown in image (d). The full development of the large-scale structure can be seen in image (e), which corresponds to a delay

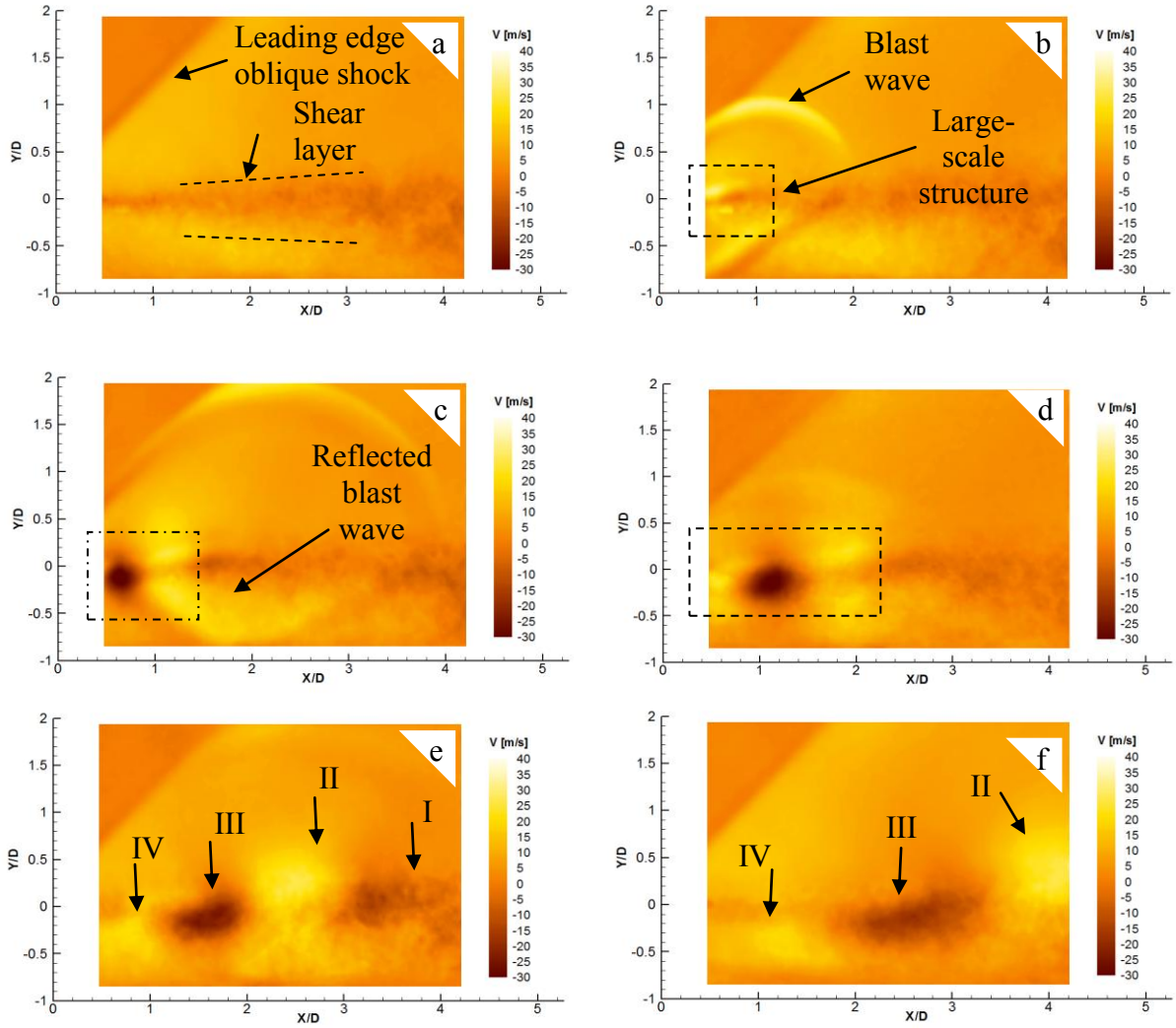


Fig 27. Average transverse velocity without forcing (a) and at selected delay times from an energy input: (b) 40 μ s, (c) 80 μ s, (d) 120 μ s, (e) 160 μ s, (f) 240 μ s.

time of 160 μ s. In this image, four regions of transverse velocity, alternating between positive and negative, can be observed; collectively, these four regions are being referred to as the large-scale structure seen in the schlieren images. The four regions have also been labeled (I, II, III, and IV) in image (e), and this convention will be referenced back to throughout the discussion.

By comparing images (b) – (e), it can be seen that while region (I) was partially visible at all delay times it did not become well defined until image (e), which was for 160 μ s. Furthermore, in image (e) region (II) appears to have undergone a similar transition and is also positioned relatively high in the shear layer. It is unclear if this result was due to the impact of the reflected

blast wave with the shear layer or the manner it would have naturally developed. In further defining the large-scale structure, the alternating directions of the neighboring velocity field regions (I – IV) suggested the presence of vortices within the shear layer. In particular, it is proposed that the pair of regions I and II and regions III and IV each represent a vortex, where then both vortices represent the large-scale structure. Taking after Adrian et al. [53] while a widely accepted definition of a vortex does not exist in the fluid dynamics community, for the present study the definition offered by Kline and Robinson [54] is used: “A vortex exists when instantaneous streamlines mapped onto a plane normal to the core exhibit a roughly circular or spiral pattern, when viewed in a reference frame moving with the center of the vortex core.” Accordingly, two necessary conditions are that the velocity field must be viewed in a convective reference frame and that the vorticity must be concentrated in a “core.” If a turbulent field consists of large-scale motion with many small-scale vortices embedded within it, it will only be possible to identify a vortex in terms of the foregoing definition if the velocity at the center of each small vortex is removed.[53] From this method, the respective streamlines for the flow field were analyzed in a convective reference frame. This was completed by subtracting the experimental convective velocity for the streamwise velocity measurements from the PIV data. The resulting streamlines are shown in Fig 28, where they have been superimposed on the transverse velocity contours at a delay a delay time of 160 μ s. The streamwise axis also been reconfigured with the stagnation point so the scale of each vortex can be clearly seen. Shown in this representation, two vortices are clearly identifiable with a stagnation point between them. While similar types of structures periodically form in cavity flow fields due to a feedback mechanism, where the modal frequency is given by Eqns. (14) or (15), Fig 28 illustrates the effectiveness of the excitation pulse to interact with the dominant instabilities of the undisturbed cavity flow.

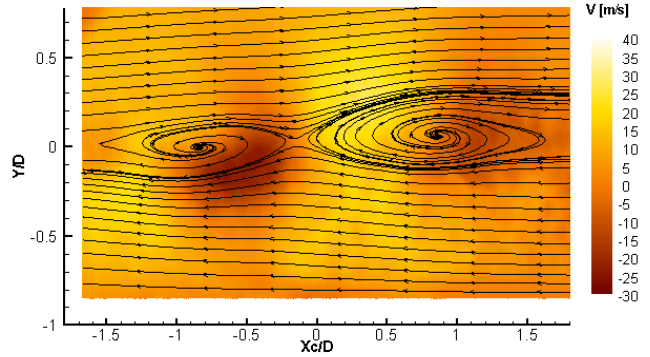


Fig 28. Transverse velocity contours at a 160 μ s from the excitation pulse with superimposed streamlines analyzed in a convective reference frame.

3.3.2. Streamwise Velocity Component

As the counterpart to the transverse velocity images, similar analysis for the average streamwise component was also determined. The resulting velocity contours are shown in Fig 29. In image (a), the flow field is shown without any excitation applied. The leading edge oblique shock can be identified as a velocity boundary in the upper left corner, where there is a slight velocity decrease downstream of the shock. Within the cavity, negative streamwise velocities are resolved representing a recirculation region, fundamental of open cavity flows.

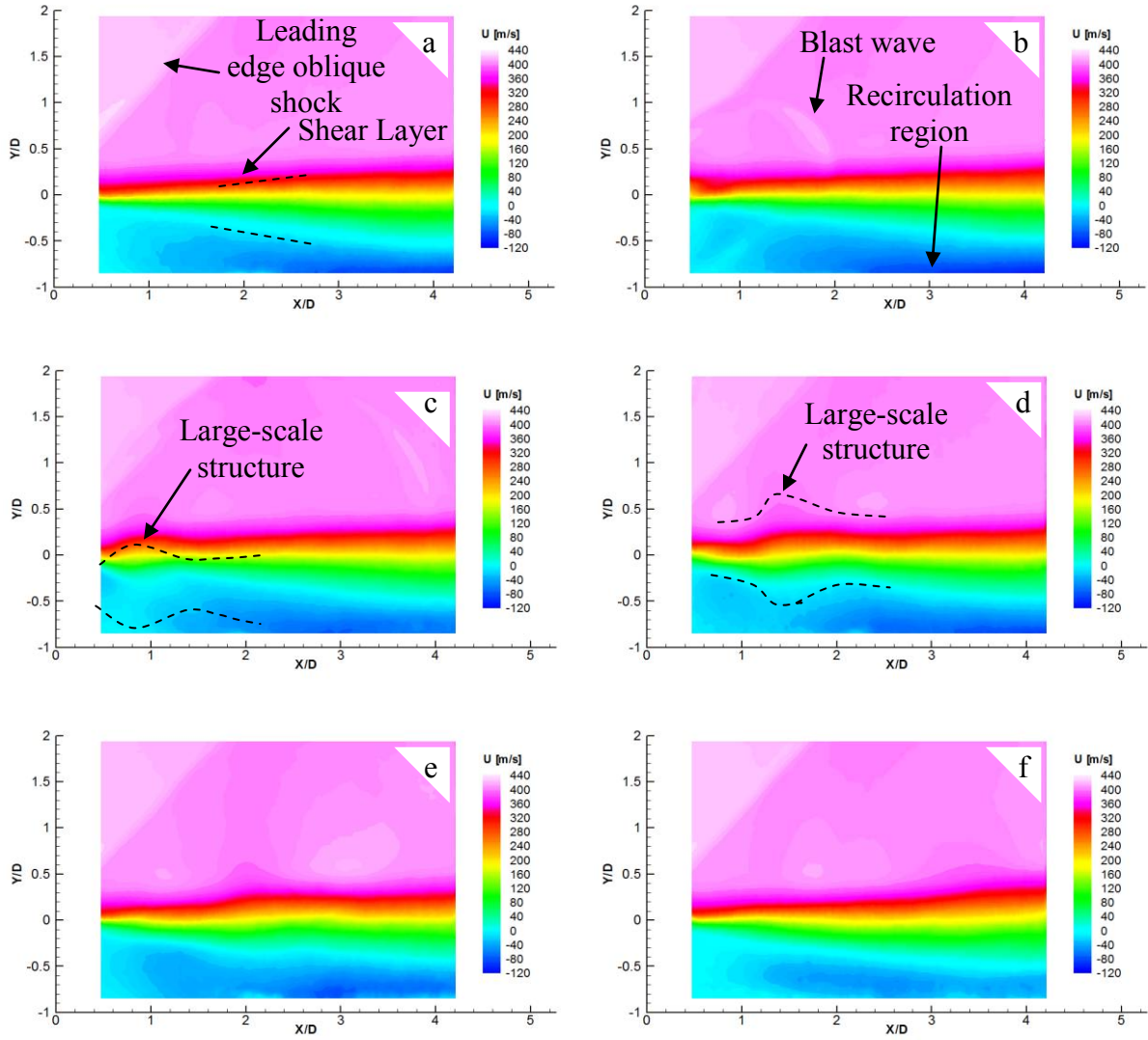


Fig 29. Average streamwise velocity without forcing (a) and at selected delay times from an energy input: (b) 40 μ s, (c) 80 μ s, (d) 120 μ s, (e) 160 μ s, (f) 240 μ s.

Velocity data from image (a) also reveal that the reverse velocities within the cavity reach as high as 25 % of the freestream value (~ 100 m/s). However, higher reverse velocities may exist outside of the region shown in image (a). For increased values of Y/D the recirculation region diminishes with the flow velocity eventually becoming stagnant and then positive representing the lower boundary of the shear layer. Within the shear layer, the streamwise velocity progressively transitions from supersonic conditions to stagnant over a distance ranging from approximately 6.1 mm at the leading edge to 11.6 mm at the trailing edge (± 0.03 mm for both measurements based on the spatial resolution of the images and the error in the mean velocity). These values were based on spatial measurements of 5% and 95 % of the freestream velocity. Although for this type of flow there were significant reverse velocities within the cavity, the recirculation region was not well defined along its streamwise length and especially at the leading and trailing edges where the shear layer thickness was estimated. Accordingly, the convention used for defining the shear layer thickness is assumed appropriate for establishing the comparative trends in the present study.

In image (b) of Fig 29, 40 μ s have elapsed from the excitation pulse. Although the blast wave is less apparent as with the images of the transverse component in Fig 27, it can be recognized as a curved region of slightly increased streamwise velocity approximately centered about the cavity leading edge. The location of the large-scale structure is also less defined. However, as seen in images (c) through (f) as the large-scale structure convects downstream it causes a slight thickening of the shear layer. This also leads to a deflection in the upper and lower boundaries defining the shear layer, as highlighted in images (c) and (d). By comparing the location of the deflection with the images of the transverse velocity component its position is approximately the same as the stagnation point between the two vortices shown in Fig 28. While the deflection may be a remnant of the initial perturbation due to the high temperature spark created by the focused laser line the velocity data suggests it is a weak compression wave traveling with the large-scale structure. Lastly, as the large-scale structure propagated downstream a decrease in the size of the recirculation region and in the maximum magnitude of the reverse velocities was also observed. This characteristic is most clearly seen by comparing images (a) and (f), where the reverse velocities decrease by almost 50% from the unforced case. As a result, in image (f) the reverse velocities reach roughly 13% of the freestream value (~ 55 m/s).

3.3.3. Correlation Analysis

Another parameter of interest in the current investigation was the convective velocity of the large-scale structure that developed in the shear layer. From this quantity the convective velocity ratio can be calculated, which as noted earlier, choosing an appropriate value for has been an unresolved issue in previous studies. Furthermore, the large-scale structure in this investigation was forced in the shear layer as opposed to naturally occurring through the feedback mechanism, which also allows for comparison under these conditions. To quantify and analyze the development of this parameter, the positive and negative transverse velocity regions of each vortex in the shear layer were tracked in space and time. This method was selected as a consequence of the centroid (position of local minimum or maximum transverse velocity) for each region being well defined. Given the associated error in the PIV velocity data and spatial resolution of the images, it was estimated that the centroidal position for each region was calculated with an uncertainty of ± 0.2 mm. Curve fitting of the experimental data also suggested that this estimate was reasonable.

Using the delay time between the excitation pulse and imaging, as well as the relationship between pixels and distance, the experimental convective velocities were determined for each of the four regions. These velocities are related to the inverse of the slope for each of the regions position-time curves as displayed in Fig 30 and the cavity depth. Again, in Fig 30 regions I – IV are identified and labeled in image (e) of Fig 27; the position of the stagnation point between the two vortices seen in Fig 28 is similarly presented. The data sets of time related positions have also been fit with linear curves. As can be seen in Fig 30, to a good approximation a linear fit can describe all variability in the positions of each set of experimental points. Accordingly, this illustrates that while the convective velocity varies between each region (I –

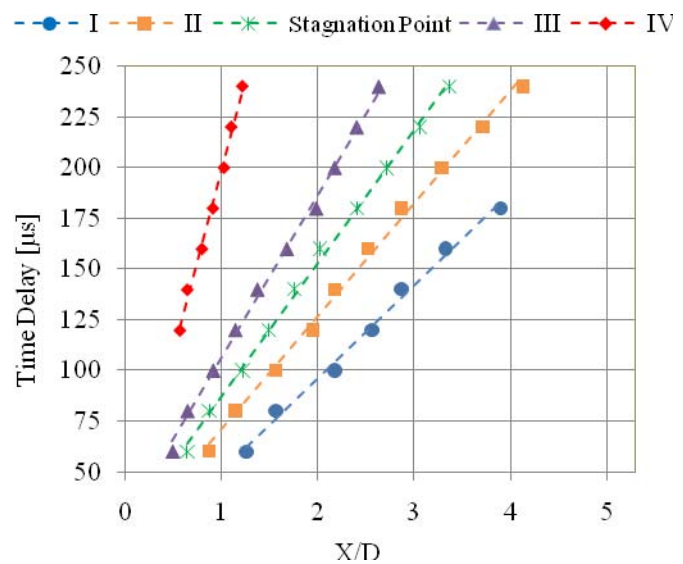


Fig 30. Spatial tracking of different features of the large-scale structure in time; points represent experimental data and lines as linear fit curves.

IV), it remains constant with changes in time and position. These velocities have also been summarized in Table 4. In Table 4 a theoretical value for the convective velocity of the stagnation point has been included. From the work of Papamoschou and Roshko [37] this convective velocity is assumed to represent the entire large-scale structure. The calculation of the theoretical convective velocity listed in Table 4 for the stagnation point was based on the assumption that the effective freestream velocity of the low-speed side was zero in the cavity and the speed of sound in the cavity calculated assuming adiabatic temperature recover, yielding a value of 224 m/s. This value is slightly higher (8.2%) in comparison to the measured results using the PIV data. However, it is interesting to note that as the temperature of the fluid in the cavity reduces to the free stream value the theoretical convective velocity approaches the experimental value of 207 m/s.

There are also several other trends that can be inferred by comparing the different convective velocities in Table 4. In particular, by temporally tracking the positions of regions I – IV and the stagnation point the convective velocity for the large-scale structure was spatially sampled along its streamwise length. From Table 4 and Fig 30, beginning with region I, the convective velocity decreased from 297 m/s to 77 m/s for region IV. Therefore, since the convective velocities were also constant in time, this result suggests a linear growth rate, or streamwise stretching, for the large-scale structure.

To further investigate the streamwise and transverse growth rate for the large-scale structure a characteristic length and height were calculated. In determining

Table 4. Summary of convective velocities

	Convective Velocity, m/s	
	Experimental	Theoretical
<i>I</i>	297 ± 9	-
<i>II</i>	242 ± 8	-
<i>Stagnation Point</i>	207 ± 7	224
<i>III</i>	169 ± 6	-
<i>IV</i>	77 ± 4	-

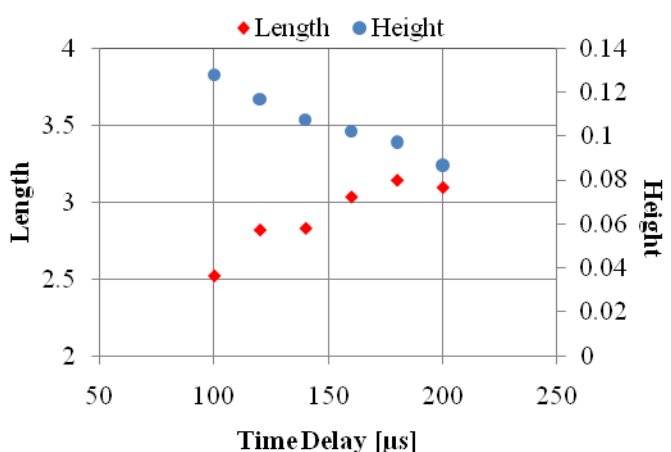


Fig 31. Characteristic length and height scale nondimensionalized by unperturbed local shear layer thickness .

this parameter the streamlines were plotted in a convective reference frame allowing the core of each vortex to be visualized. Using the coordinates for each origin, the characteristic length was then expressed as the difference in the streamwise locations between the cores of the upstream and downstream vortices. The results are shown in Fig 31, where the values have been nondimensionalized by the unperturbed local shear layer thickness at the location of the stagnation point for each corresponding delay time. Once the shear layer becomes fully developed its thickness was expected to grow linearly along the length of the cavity.[37] A characteristic height was also calculated by taking the difference of the vortex core locations in the transverse direction.

In quantifying the accuracy of the values presented in Fig 31 consideration was given to several sources of error. These included the uncertainty in the convective velocity, shear layer thickness, mean velocity, and in the ability to resolve each vortex core. Based on these factors, the values presented for the characteristic length and height were estimated to be within ± 0.3 mm, or approximately ± 0.02 in terms of the nondimensional values presented in Fig 31. In interpreting the data shown in Fig 31, a linear trend in time appears to exist for the nondimensionalized characteristic length and height scales. This result is consistent with the constant convective velocities for regions I – IV of the large-scale structure as shown in Table 4. Additionally, the streamwise distance between the upstream and downstream vortices is increasing at a rate greater than the growth of the shear layer. For the transverse direction the distance between the vortices is decreasing. However, it is only slightly greater than the uncertainty of the measurement and it is unclear whether this trend will continue after a value of zero for the characteristic height is achieved.

4. TRANSVERSE JET IN A SUPERSONIC CROSSFLOW

The second flow configuration investigated the application of ELFC to a sonic transverse jet injected into a supersonic crossflow. The transverse (normal) injection of a gaseous jet into a supersonic freestream is a fluid dynamic configuration that has been studied extensively due to its widespread use in a variety of technological applications.[55] Early investigations in the area were motivated by the aerodynamic control of supersonic vehicles at high altitude, forming initial qualitative descriptions for the structure of the resulting flow field.[56] [57] Of particular

relevance to the current study is the use of this flow field in high-speed propulsion systems. Because of the high velocities in these systems, challenges arise in the fuel injection method which must provide sufficient fuel-air mixing in an environment with limited flow residence time in the combustor.[27] As a means of addressing this problem past studies have investigated the arrangement of the transverse injection of fuel from a wall orifice to evaluate near-field mixing and methods of enhancing it.[58]

A jet injected normally from a wall into a crossflow involves two fundamental flows: a perpendicular free jet and a boundary-layer driven by uniform flow far above the injection wall. However, the characteristics of the transverse jet are far more complex than those present in these basic canonical flows.[59] Fig 32 (Refs. [58] [60]) illustrates the typical flow field characteristics of an underexpanded transverse sonic jet injected into a supersonic crossflow. The displacement of the crossflow by the jet induces a three-dimensional bow shock, due to the partial blockage of the flow.[61] The bow shock causes the upstream wall boundary layer to separate creating a region where the boundary layer and jet fluids mix at subsonic speeds, upstream of the jet exit. This region, confined by the separation shock wave formed in front of it, is important in transverse injection flow fields owing to its flame-holding capability in combusting situations.[58]

Turning to the internal structure of the jet, after leaving the wall orifice the underexpanded jet initially expands through a Prandtl–Meyer expansion fan centered at the nozzle lip.[61] In the case of circular injector ports, this expansion terminates in a barrel shaped shock and a Mach

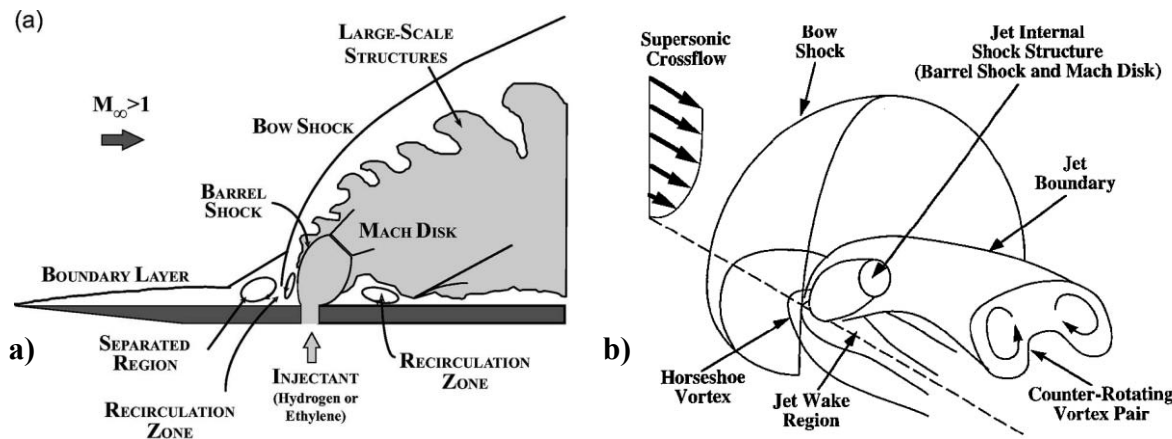


Fig 32. Illustration of an underexpanded transverse injection into a supersonic crossflow for (a) instantaneous side view and (b) 3D perspective of averaged features (images from Ref. 60).

disk. The upstream separation region creates a horseshoe shaped vortex that wraps around the injector exit along the wall.[62] The majority of the jet fluid passes through the oblique shocks that define the sides of the barrel shock and forms an annular shear layer between the jet plume and the crossflow. Recirculation regions are located just upstream and downstream of the jet orifice near the wall. The velocity field within the jet plume downstream of the barrel shock is dominated by two streamwise-oriented, counter-rotating vortices.[61]

Mixing properties of normal injection into supersonic flow are controlled by jet vortical structures.[58] Following the work of Ben-Yakar et al., [29] experimental studies by Fric and Roshko[63] of a transverse jet injected into a low-speed crossflow have given insight into the characterization of these flow field features. In particular, four types of coherent structures were discerned: (i) near-field jet shear layer vortices; (ii) the horseshoe vortex which wraps around the jet column; (iii) the far-field counter-rotating vortex pair; (iii) downstream wake vortices originating from the horseshoe vortex. Presumed vortical structures for a transverse jet in a supersonic crossflow are shown in Fig 32.

The near-field mixing of transverse jets is predominantly controlled by an “entrainment-stretching-mixing process,” which is driven by large-scale jet-shear layer vortices. Near the jet exit, the injected fluid moves with a higher velocity tangent to the interface than the freestream fluid. This effect leads to the periodic formation of large-scale vortices which engulf large quantities of freestream fluid and draw it into the jet shear layer. These vortices also act to stretch the interface between the unmixed fluids. More specifically, stretching increases the interfacial area and steepens the local concentration gradient along the entire surface while enhancing the diffusive micromixing. Preliminary studies of the convection characteristics of these large-scale structures (conducted in sonic transverse jet injection into supersonic crossflow), suggested that in the far-field eddies tend to travel with velocities that are close to the freestream velocity. For high-speed freestream conditions, the large-scale coherent structures, where the fuel and air are mixed by slow molecular diffusion, will also convect at high speeds, suggesting that the combustion process will be mixing controlled.[58] Accordingly, understanding of the mixing process and its enhancement presents a critical component in the development of air-breathing propulsion systems for use in hypersonic flight.

In addition to the mixing characteristics of the flow field, simultaneous penetration of the fuel jet into the high-speed crossflow must also be achieved to ensure efficient combustion.[64]

Penetration has been shown to be dependent primarily on the jet-to-freestream momentum flux ratio (J), which is expressed by:

$$J = \frac{(\gamma PM^2)_j}{(\gamma PM^2)_\infty} \quad (19)$$

where the subscripts j corresponds to the jet exit conditions and ∞ to the freestream conditions upstream of the bow shock. In Eqn. (19), γ is the specific heat ratio, P is the pressure, and M the Mach number. Work conducted by Schetz and Beillig [65] have identified the jet-to-freestream momentum flux ratio as the most important parameter that determines jet penetration. However, exceptions under different conditions/configurations may exist.[58]

In an effort to further understand the mechanisms of mixing in a jet-in-crossflow, as well as gain further insight into the physics of the flow field, there have been a vast number of experimental and computational investigations. In a recent numerical study by Kawai and Lele,[66] an underexpanded sonic jet injection into a supersonic crossflow was considered using high-order compact differencing/filtering schemes coupled with recently developed localized artificial diffusivity methodology in the context of large-eddy simulation. For their study, flow conditions from the experiment by Santiago and Dutton [67] were selected ($M_\infty = 1.6$). To that end, the simulation by Kawai and Lele [66] qualitatively reproduced the unsteady dynamics of the barrel shock and bow shock as observed in the experiment. With regard to the processes controlling the jet mixing, two regions of vortex formation that create hairpin-like structures were identified in the windward and leeward jet boundaries, and that these vortices play an important role in determining the behavior of jet fluid stirring and subsequent mixing.

In a another numerical study conducted by Srinivasan and Bowersox,[62] simulations were conducted for a sonic transverse jet in a Mach 2 and Mach 5 crossflow using diamond-shaped orifices. The authors report that two new vortex features were observed in the vicinity of the injector port when compared with circular injector ports. First, a pair of vortices was seen to form near the leading edge of the injector due to the corner vortices in the injector port and the interaction between the freestream and injector fluids. Of particular interest is the potential for these structures to serve as a mixing enhancement mechanism. Second, their investigation found that the shape of the barrel shock generated by the diamond-shaped injector influenced the flow around the injector port, leading to the formation of a vortex pair downstream of the injector port. They report that this induced flow structure can act as a flameholding device.

In other related experimental work, a study conducted by VanLerberghe et al.[61] investigated a sonic jet injected normally into a Mach 1.6 crossflow. Shadowgraph photography and planar laser-induced fluorescence from acetone were used to obtain temporally resolved flowfield visualization of a side-view of the barrel shock region, a side-view of the downstream plume, and an end-view cross section of the plume. The mixing produced by large-scale turbulent structures was analyzed by instantaneous images, mean and standard deviation images, and image-intensity probability density functions. Comparisons of the instantaneous images and probability density functions illustrated the role of large-scale rolling structures and jet-like plumes in transporting coherent packets of fluid across the three-dimensional shear layer formed between the jet and crossflow. Significant instantaneous mixing in the flow field occurred in the wake region downstream of the barrel shock region and below the jet centerline. They also report that the counter-rotating streamwise vortex pair in the jet plume plays an important role in the scalar mixing processes, as it transports jet fluid down toward the wake and entrains crossflow fluid from below up into the jet.

In another experimental study by Ben-Yakar et al.,[58] the temporal evolution, the penetration, and the convection characteristics of hydrogen and ethylene sonic jets in a Mach 10 crossflow were observed. The experiment was conducted with schlieren imaging and performed for a similar jet-to-freestream momentum flux ratio between the two gases (hydrogen and ethylene). While previously the momentum flux ratio was considered to be the main controlling parameter in the jet penetration, results from their work suggested the existence of an additional mechanism that altered the penetration, as well as affected the vortical structures and mixing properties of the jet shear layer. Increased penetration depths of the ethylene jets were attributed to the significant differences in the development of large-scale coherent structures present in the jet shear layer. More specifically, for the hydrogen case, the periodically formed eddies persisted for a longer distance downstream, while for ethylene, the eddies lost their coherence as the jet bended downstream. The large velocity difference between the ethylene jet and the freestream (due to the increased molecular weight of ethylene) was seen to induce enhanced mixing at the jet shear layer as a result of the velocity induced stretching-tilting-tearing mechanism.

As part of the work by Ben-Yakar et al.,[58] the authors suggested that there would be value in identifying other mechanisms or controlling parameters, other than the jet-to-freestream momentum flux, which may alter the large eddy characteristics of the jet shear layer and

therefore affect near field mixing in realistic conditions. In an attempt to also contribute to this effort, we report an experimental study on the influence of pulsed energy deposition through laser induced optical breakdown on the characteristics of a transverse sonic jet in a supersonic crossflow.

4.1. Experimental Arrangement: ELFC Transverse Jet in a Supersonic Cross Flow

In the current experimental study, a transverse sonic jet in a crossflow was investigated utilizing a supersonic blow down wind tunnel. The tunnel was operated with good flow quality (i.e. in absence of strong compression or expansion waves in the test section) at a Mach number of 2.25. Air was supplied from a compressor with a volumetric flow rate of 34 m³/min and at a pressure of 1000 kPa. The flow from the compressor was filtered, dried, and cooled, and stored in a 140 m³ tank farm. From this point, the air traveled through a pipe and a series of control valves prior to entering the wind tunnel. Before reaching the test section, the flow passed through a conventionally arranged settling chamber with a honeycomb filter to reduce the scale of the incoming turbulence and to straighten and make the flow uniform. After leaving the test section, the flow entered the diffuser which was approximately 91.4 cm long and sloped at 2.5°. This diffuser exhausts through a bent pipe wrapped in sound insulation and then through a silencer to the atmosphere.[42]

The test section used for investigation had a square geometry measuring 63.5 mm on each side. There were also two large windows (119.1 mm x 239.7 mm x 25.4 mm) on each side of the test section and a smaller bottom window (36.5 mm x 163.5 mm x 19.1 mm). Each of the windows was fabricated with a BK-7 grade A glass to provide high optical quality. The top of the test section was constructed with a polycarbonate resin thermoplastic (LEXAN), in which a circular round jet was installed with an exit diameter (D) of 4.8 mm and operated with a jet-to-freestream momentum flux of $J = 1.7$, as calculated from Eq. (19). A full description of the wind tunnel can be found in Ref. [42], and relevant flow condition parameters have also been summarized in Table 5.

As a means of applying excitation to the flowfield, pulsed energy deposition from a Q-switched Nd:YAG laser was used. The laser was operated at a wavelength of 532 nm, delivering approximately 200 mJ per pulse at a frequency of 10 Hz. The energy generated from the laser pulse was manipulated using a series of lenses (Fig 33) and brought through the center of the jet where it was focused to a point; the final distance from the last lens to the jet exit was approximately 70 mm. This optical arrangement resulted in the induced optical breakdown of air, providing a single burst of excitation by ionizing the flow and creating plasma. The excitation was applied at three vertical positions (relative to the jet exit) within the flow field. These included vertical distances of 0, 1.5, and 3 jet diameters from the jet exit, and in each case along the jet centerline. The resulting flow field was analyzed with schlieren photography and particle image velocimetry (PIV). For the unperturbed flow field, additional diagnostics of pressure sensitive paint measurements and surface oil flow visualizations were also conducted.

The schlieren system was setup in a standard Z arrangement. Illumination was provided by a Xenon spark lamp, which acted as a point light source providing high luminance and emitting a broadband light. The generated light was then collimated through the wind tunnel test section and focused to a point. Instantaneous schlieren images were recorded in the vertical and horizontal knife edge configuration with a scientific-grade 1600 x 1200 pixel CCD camera; the CCD camera was also used for each of the diagnostics described below. The duration of each flash for the spark lamp was on the order 20 ns, which resulted in conditions short enough to freeze most of the turbulent structures and produce instantaneous images of flow.[39]

Two-dimensional particle image velocimetry (PIV) measurements were conducted to obtain quantitative velocity fluctuation data. The crossflow and jet were individually seeded with Di-Ethyl-Hexyl Sebacate (DEHS) though the use of separate Laskin Nozzles that generated particles with a diameter less than 1 μm .[46] For both flows, seeding was introduced approximately 3.5 m upstream of the test section which resulted in a sufficient dispersion of the particles. The

Table 5. Summary of experimental test condition.

Freestream Stagnation Pressure	$276 \pm 3 \text{ kPa}$
Freestream Boundary Layer Thickness	$3.05 \pm 0.13 \text{ mm}$
Freestream Mach Number	2.25
Jet Stagnation Pressure	$378 \pm 13 \text{ kPa}$
Jet-to-Freestream Momentum Flux Ratio	1.7
Jet Exit Mach Number	1
Jet Exit Diameter	$4.8 \pm 0.05 \text{ mm}$

particles were illuminated by a thin (on the order of 0.1 mm) light sheet. The light sheet was created by a dual-head New Wave Nd:YAG laser in conjunction with spherical and cylindrical lenses. The light sheet was brought in through the bottom access window of the test section and exited through the top section constructed of LEXAN. This design allowed particles near the surface to be recorded without saturating the CCD camera. An illustration of the setup is shown in images (a) and (b) of Fig 33. The PIV laser was operated at a frequency of 532 nm, with each pulse delivering approximately 50 mJ of energy. The time separation between the laser pulses to illuminate the particles was adjusted according to the flow velocity and camera magnification. For the results shown in the present, a separation time of approximately 600 ns was used.

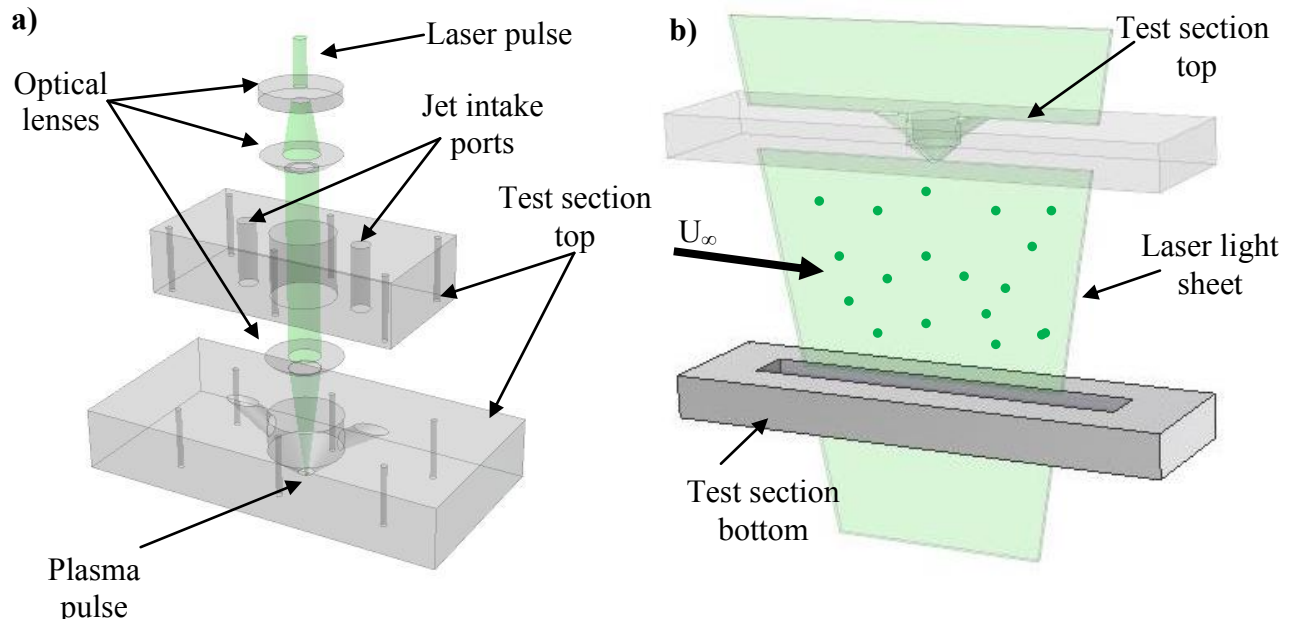


Fig 33. Schematic of (a) the jet and excitation arrangement and (b) PIV setup.

The accuracy of velocity measurements obtained from the PIV data was a composite of the ability of the seed to follow the flow and for the imaging and analysis system to record and process a field of particle images.[47] In quantifying the accuracy a number of factors need to be considered, such as the number of samples, turbulence intensity, computational algorithm, equipment used, and particle size.[39] In an effort to quantify some of these factors, several sources of error were considered. The error in timing between two laser pulses was estimated to be 6 ns. The uncertainty in pixel displacement by correlation analysis of the PIV software

program was approximated at one-tenth of a pixel, assuming the laser sheet is providing Gaussian illumination. Subpixel accuracy was achieved by matching the intensity captured from illuminated particles through a Gaussian shaped peak locator, resulting in a positional error estimate of approximately 0.1 pixels.[48]

For the mean flow, another source of error in the PIV data is due to the turbulence, which requires averaging of multiple images to obtain accurate mean properties. Using the approach outlined by Grant and Owens [68] and following the work of Zhuang et al.[39] the relative error in the mean velocity from sample averaging was estimated at up to 2.6% for the unperturbed flow field velocity data and for a 95% confidence level. This value was based on the maximum turbulence intensity observed in the shear layer ($U_{RMS}/U_{\infty} = 0.35$, discussed below) and the averaging of 680 image pairs. This also translates to an uncertainty of no more than 8.3% for the turbulence intensity measurements. The uncertainty is slightly increased for the velocity data with forcing applied, as fewer images pairs were used for sampling averaging.

Pressure sensitive paint (PSP) measurements were conducted to investigate the static pressure distribution on the surface in the near jet region. For this diagnostic, the surface surrounding the jet exit was coated in a paint consisting of organic luminophores suspended in polymeric binders. The luminophores were excited using a blue LED lamp as an illumination source. The LED lamp was fitted with a low-pass filter so that the incident light in the range of the luminescent signal wavelength was mostly filtered. The intensity of the fluorescence from the PSP was captured with a CCD camera equipped with a 50 mm lens and a 610 nm high-pass filter to separate the fluorescent signal from the paint from that of the light source. The spatial resolution of the PSP surface measurements was calculated to be $59.9 \mu\text{m}/\text{pixel}$ or approximately 278 pressure measurements per square millimeter. 50 run images and 50 reference images were acquired for the results presented. Each sequence was ensemble-averaged and the background noise subtracted to provide a single run image. Following the experiment, pressure tap measurements were taken at five selected locations using transducers and correlated to the corresponding PSP intensity values to form a calibration curve. The location of the tap sites were selected to include a wide range pressures (approximately 1 – 8 PSIA), thereby minimizing errors introduced through extrapolation. The resulting calibration curve was constructed with a second-order polynomial and had a correlation coefficient of $R^2 = 0.999$. The maximum deviation of the pressures at the tap sites to the calibration curve was approximately 0.12 PSIA.

Finally, surface oil flow visualizations were performed by using a surface tracer mixture consisting of Oleic acid, titanium dioxide, and silicon oil. The mixture was applied with a standard foam brush covering the entire surface far upstream and downstream of the jet exit. Images of the surface were then recorded with a CCD and in ambient light.

4.2. Surface Oil Flow Visualization: ELFC Transverse Jet in a Cross Flow

Surface flow visualization experiments were performed as a means of investigation of the streaklines surrounding the jet exit. Using this technique, instantaneous images of the surface for the unperturbed flow field were recorded. A selected image is shown in Fig 34 for which the tunnel was operated long enough for steady state surface flow patterns to develop. In Fig 34, the streamwise and transverse positional coordinates (X , Y) have been nondimensionalized by the jet diameter. The jet exit is located at the positional coordinates of $(0, 0)$. As shown by Fig 34, the surface flow pattern displays expected symmetry about the tunnel midline and also indicates that the near-jet region was not affected by the influence of the wind tunnel side walls. There are several separation lines that can be identified in Fig 34 and have been labeled (1) – (4). Following the work of Everett et al.,[69] lines (1) and (2) can be seen to wrap around the injector

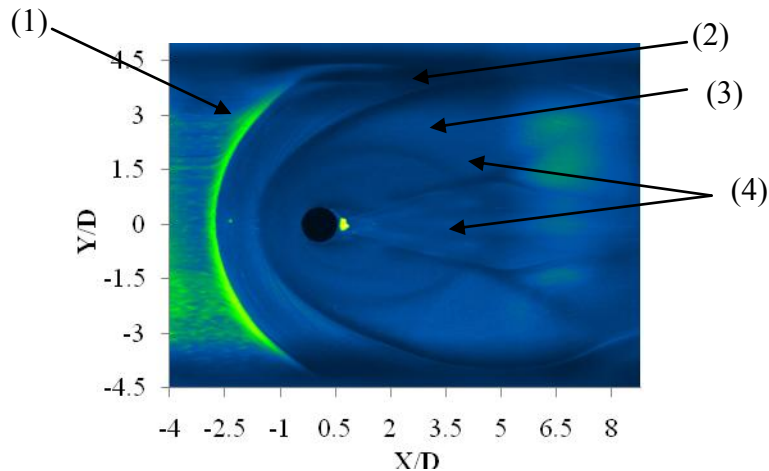


Fig 34. Surface flow oil visualizations of a transverse sonic jet in a supersonic crossflow.

the velocity data taken from the present work, lines (1) and (2) appear to correspond to the approximate position of the lambda shock and bow shock, and line (3) to the barrel shock.

port. The distinctive shape of these lines has led investigators to commonly refer to the vortex system resulting from the flow separation in this region as the horseshoe vortex. Consistent with the work by Everett et al. [69] the oil between lines (1) and (2) was observed to move outward and around the jet and not penetrate the boundary of either line. By comparison with

Also shown in Fig 34, immediately downstream of the jet exit a point was observed where oil accumulated and then two separation lines emerged. These lines are labeled as (4) in Fig 34. Again, similar to the work by Everett et al. [69] these lines appeared to represent a boundary between the reattaching flow downstream of the jet exit and the fluid upstream of the exit that moved around the jet. The lines initially diverge with increasing downstream position, until a location of approximately $x/D = 5$, after which they were observed to converge slightly.

4.3. Pressure Sensitive Paint: ELFC Transverse Jet in a Cross Flow

PSP was applied to the near-jet region to obtain qualitative information for the surface pressure distribution generated by the transverse jet flow field. A color contour plot of the resulting distribution of the absolute surface pressure is shown in Fig 35. In Fig 35, the flow direction is from left to right, where the jet exit is represented by the dark circular feature located

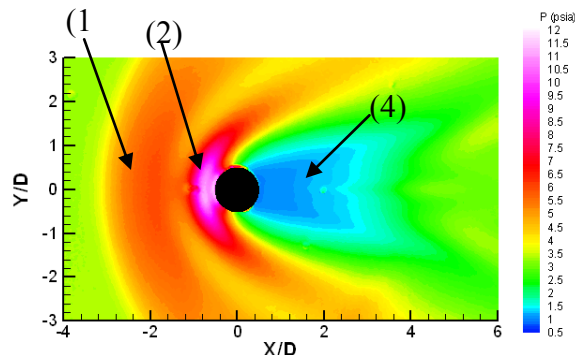


Fig 35. Surface pressure distribution in the near-jet

injector port. High-pressure region (1) is caused by the lambda shock and is (spatially) the larger of the two. The foot of the curved bow shock is located between the high-pressure regions (1) and (2). The bow shock causes a significant increase in pressure in region (2) and extends to the front lip of the jet exit.[69] Behind of the jet exit, a low-pressure region (4) exists that extends approximately 3.5 jet diameters downstream (along the tunnel centerline). However, low-pressure region (4) extends slightly further downstream for off centerline axis locations, giving the region a wing-like shape. This characteristic has also been reported on by other investigators.[69]

at the image origin. Each of the lines described in Fig 34 can also be identified in Fig 35 as a boundary to a distinctive pressure region. For clarity, these pressure regions have been labeled to correspond to the labels of the separation lines in Fig 34. Starting upstream of the jet exit, the lambda shock and bow shock are represented as two curved bands of high-pressure that wrap around the

4.4. Schlieren Imaging: ELFC Transverse Jet in a Cross Flow

Instantaneous schlieren images were obtained to investigate the distribution of density gradients within the flow field of a transverse jet. For this study, 200 instantaneous images were collected and phase averaged. Although the flow field was investigated with the knife edge in the horizontal and vertical arrangements, only images in the vertical orientation are presented. The images in the vertical arrangement were selected because of the suppression of the vertical density gradients due to the boundary layer, allowing key features of the flow field to be more easily visualized.[30] The resulting images (instantaneous and phase averaged) for the unperturbed flow are shown below in Fig 36. The flow is from left to right, and the incoming boundary layer is identified in Fig 36 (a). Several weak waves can also be identified in Fig 36. These weak waves were formed from minor surface discontinuities in the test section walls and are common in most supersonic wind tunnel facilities. Their presence did not appear to influence the results presented in any significant manner. In Fig 36 (b), distinct flow field features in the near-jet region have also been labeled, specifically: the lambda shock, barrel shock, bow shock, and Mach disk.

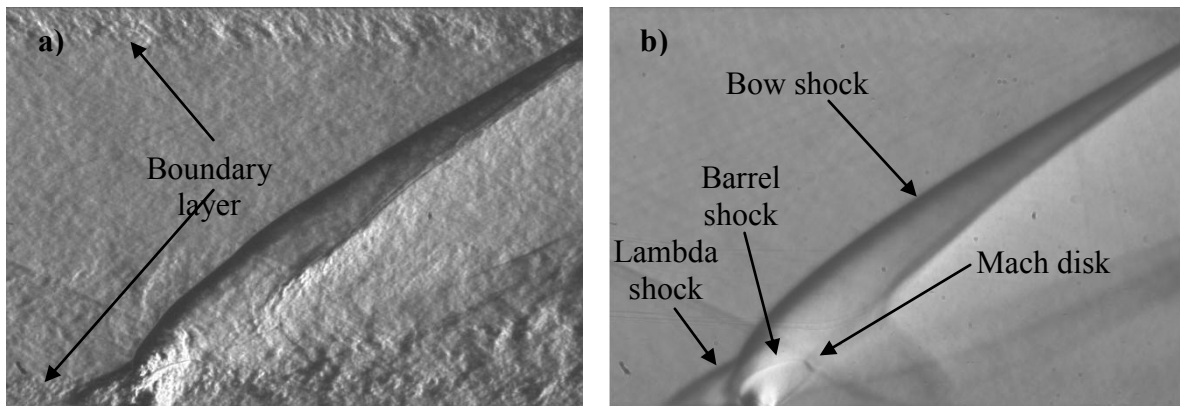


Fig 36 (a) Instantaneous and (b) time-averaged schlieren images of a sonic transverse jet in a supersonic crossflow.

The experimental study for the flow field following the excitation pulse was conducted for incremental delay times ranging from 5 – 120 μ s from the laser energy input at the jet exit. Phase averaged schlieren images are illustrated in Fig 37 for selected delay times from the excitation pulse. Also, for the images in Fig 37, the excitation pulse was located at a transverse position of 0D from the jet exit (i.e. directly at the jet exit). Although schlieren imaging was conducted for the remaining two vertical positions of the excitation pulse (1.5D and 3D), similar

results were observed for each of the three cases. Moreover, the 0D case most clearly illustrated the interaction between the excitation pulse and relevant flow field features. All three cases will be considered and compared in the velocity data section to follow. Apparent in all the images,

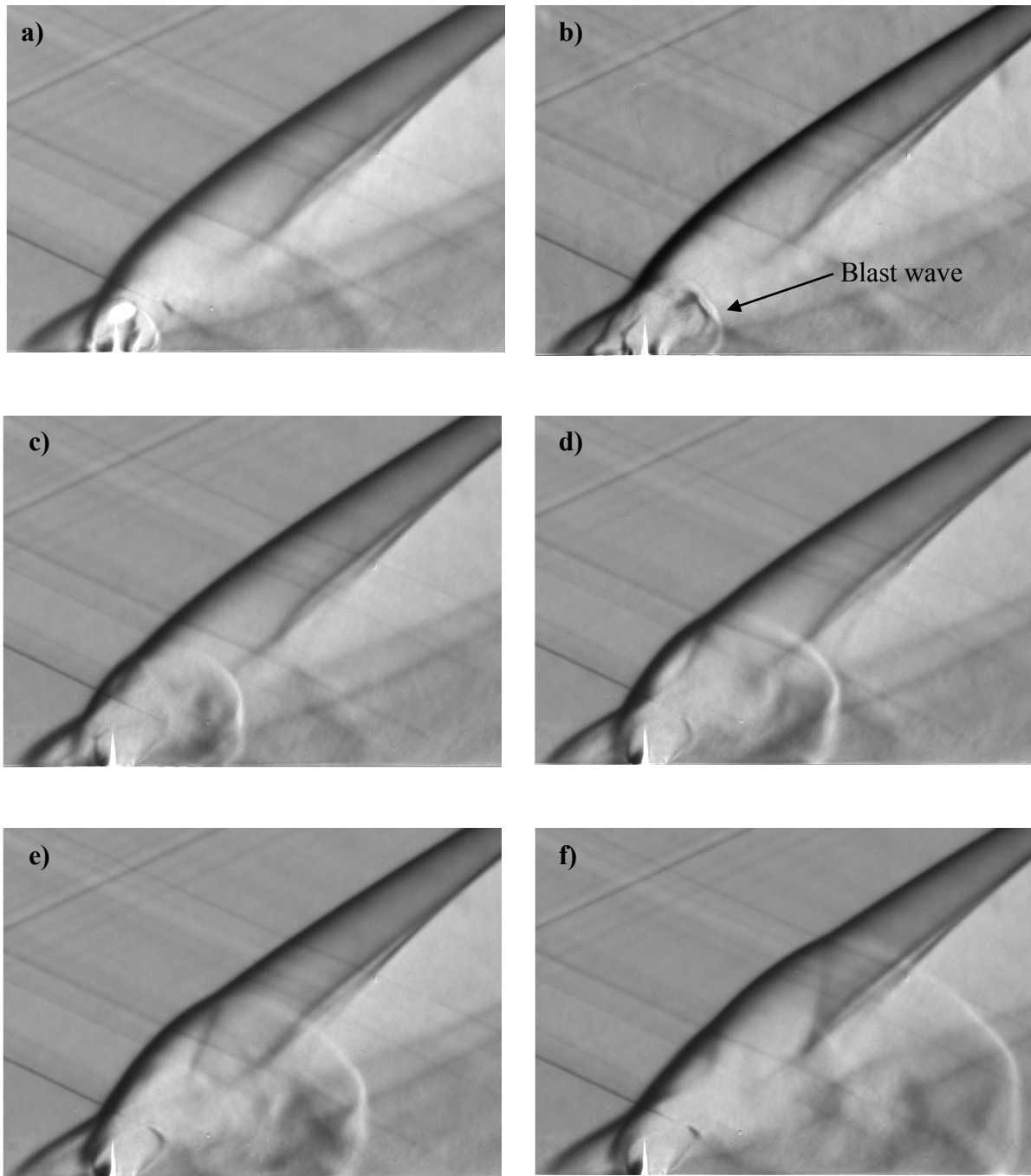


Fig 37. Phase averaged schlieren images at selected delay times from a 200mJ energy input at a 0D vertical location: (a) 5 μ s, (b) 10 μ s, (c) 20 μ s, (d) 30 μ s, (e) 40 μ s, (f) 60 μ s for a sonic transverse jet in a supersonic crossflow.

the flow field features as described for Fig 36 (b) can be identified. Image 37a corresponds to a 5 μ s delay from the excitation pulse. In this image, the blast wave from the laser pulse originates at the jet exit and is distorted by the relative velocity internal and external to the jet. At this point the disturbance has not significantly propagated through the flow. In images Fig 37 (b) and Fig 37 (c), the delay time between excitation and imaging was increased to 10 μ s and 20 μ s, respectively. At these increased times, the disturbance from the laser pulse, which first appeared as a single thermal spot, has traversed through the flow field, altering some of the characteristics seen in the unperturbed flow. Specifically, the propagation of the blast wave through the flow field has disrupted the structure of the barrel shock and Mach disk and can be seen reforming in images Fig 37 (d) and Fig 37 (f).

4.5. Particle Image Velocimetry: ELFC Transverse Jet in a Supersonic Cross Flow

In addition to the schlieren imaging, PIV was conducted to determine the two-component velocity field for the jet-in-crossflow (with and without excitation) and to determine the incoming boundary layer thickness (δ) without the jet operating. For all PIV images presented the streamwise and transverse axes have been similarly nondimensionalized by the jet exit diameter, as in Fig 34 and Fig 35. The jet exit is also again located at the origin of the image, or the coordinates $(x/D, y/D) = (0, 0)$.

For measurement of the incoming boundary layer thickness, the test section model was replaced with a smooth top-wall assembly not containing the transverse jet orifice. Also, in constructing the boundary layer thickness, ensemble averages of 1344 image pairs were used. The results are presented as color contours for the average streamwise velocity component as shown in Fig 38 (a). In Fig 38 (a), although velocities only as low as 70% of the freestream velocity were measured, the transition from slower velocities near the wall to freestream conditions can still be observed. From this velocity data, a boundary layer profile was constructed and is illustrated in Fig 38 (b). A boundary layer thickness (δ_{99}) was also calculated based on the position of 99% of the freestream velocity. Under this approach, the boundary layer thickness was determined to be approximately $\delta_{99} = 3.05$ mm (± 0.13 mm, based on measurement resolution), where the current experimental arrangement was capable of resolving velocity vectors within 200 μ m of the surface.

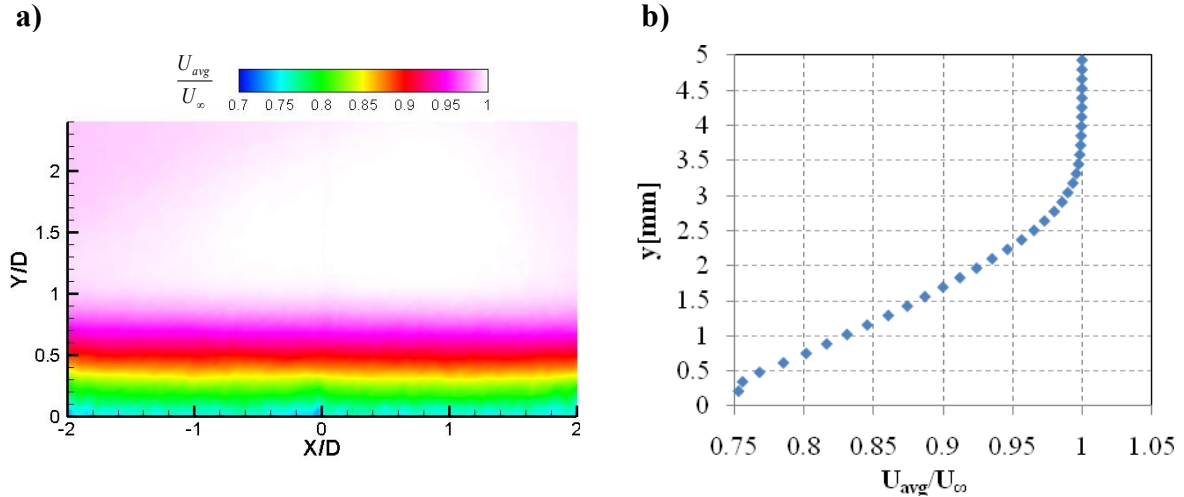


Fig 38. Boundary layer illustrations using (a) color contours of the average streamwise velocity and (b) a spatially averaged profile.

In the analysis of the unperturbed flow, ensemble averages of 640 image pairs were used. The results are presented as color contours for the average streamwise and transverse velocity along with their root-mean-square (RMS) components in Fig 39. Corresponding streamlines have also been superimposed on the image of the average streamwise velocity [Fig 39 (a)] and vectors for the image of the average transverse velocity [Fig 39 (b)]. As can be seen in the images in Fig 39, the PIV system was capable of resolving several of the features seen in the schlieren images and that are typical of a transverse jet flow field. Among these are the lambda shock, bow shock, barrel shock, and Mach disk. However, for the last two features, because of the scarcity of flow tracking particles in the near-jet region (due to the flow field dynamics) and the resolution of the subregions used to calculate the PIV vectors, the barrel shock and Mach disk were imaged with limited detail. Also, it is important to note that the particles utilized for PIV, although small, still have a slight lag time in tracking the fluid. This is particularly evident across the sharp velocity gradients found through shock waves. To this end, only the relative position and size of these features can be inferred from the velocity images with little information on their internal structures.

For the jet flow field following the disturbance from the excitation pulse, two-component contour plots were generated for the vorticity field. However, in contrast to the images in Fig 39, the view was shifted almost three jet diameters downstream of the spot where the forcing was introduced to protect the CCD camera from the intense laser light in that area. As a means of

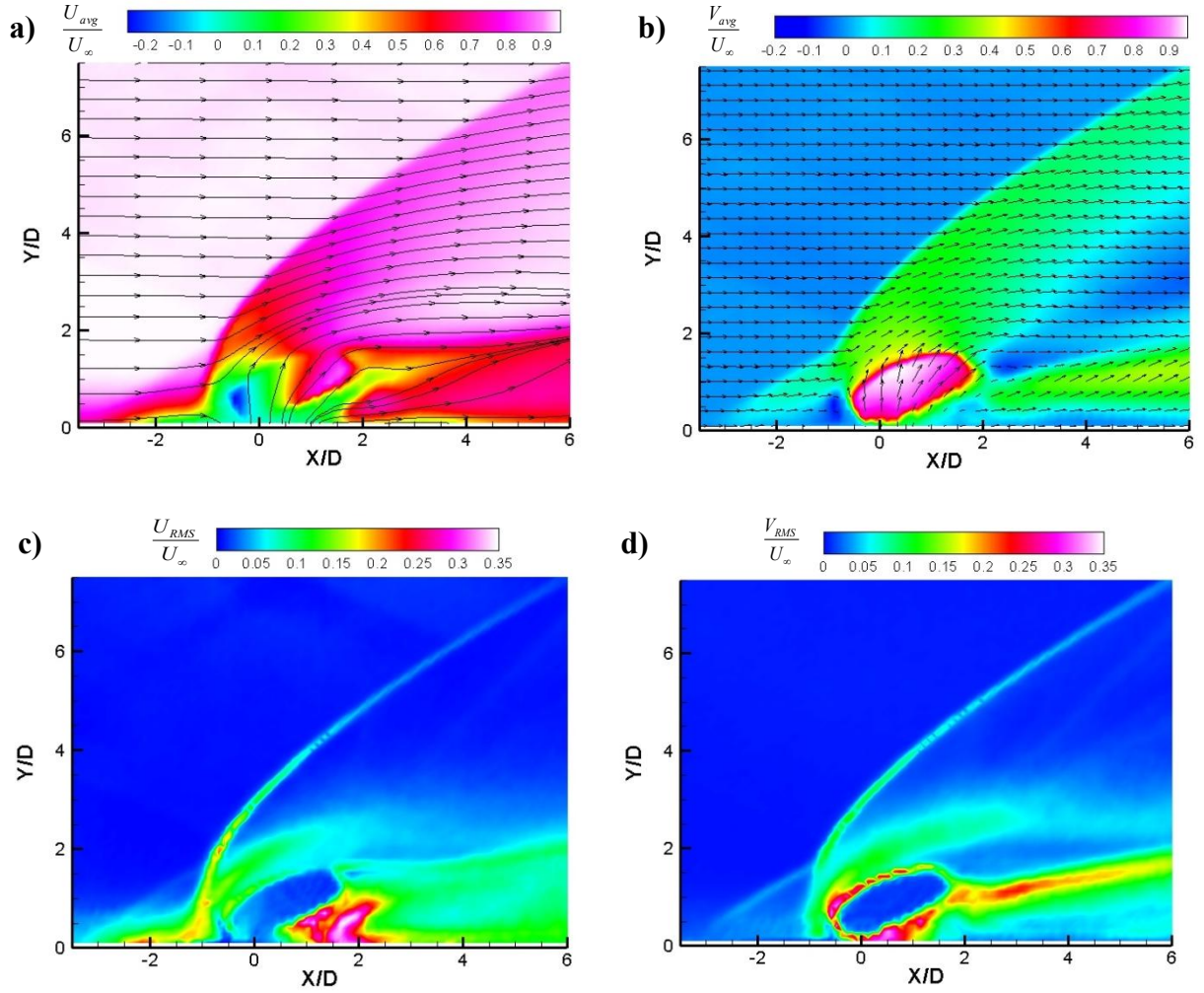


Fig 39. (a) Average streamwise velocity, (b) average transverse velocity, (c) streamwise root mean square velocity, and (d) transverse root mean square velocity for a sonic transverse jet in a supersonic crossflow.

comparison, vorticity field images of the unperturbed flow, for both, the full and shifted field of view, are shown in Fig 40. For both images shown in Fig 40, the instantaneous vorticity values have been nondimensionalized by the freestream velocity and the jet exit diameter. In image 9a, the full view of the transverse jet flow field is shown in which it can be seen that the highest values of vorticity are within a region of 1 – 2 jet diameters of the jet exit. A layer of increased vorticity, however, does persist further downstream of the jet exit, but with decreasing intensity. In image Fig 40 (b), a shifted (and slightly zoomed in) view of the vorticity field is shown. The streamlines for several coherent structures detected in the

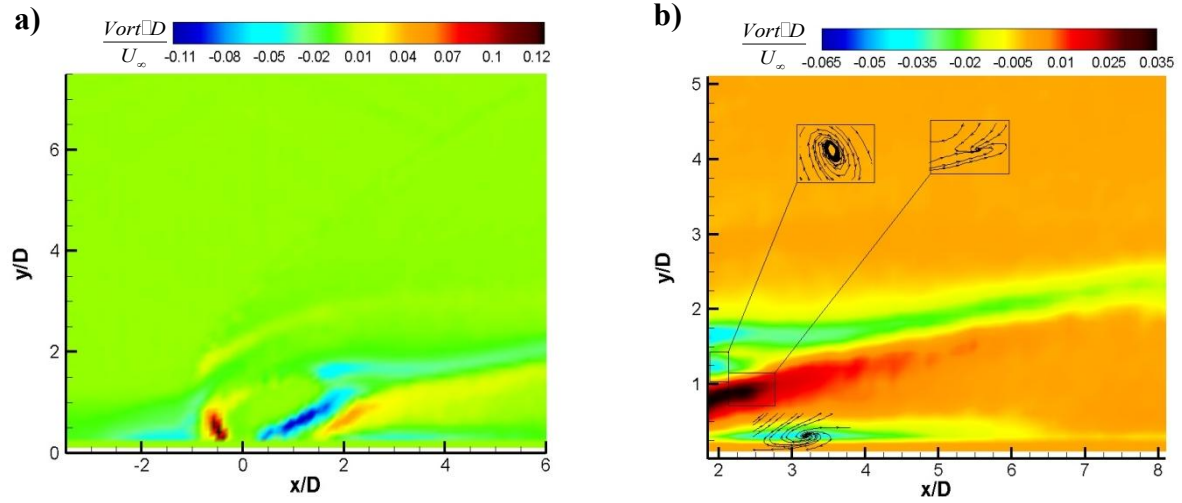


Fig 40. Vorticity contour plots for the (a) full and (b) shifted field of views for the unperturbed flow field.

unperturbed flow field have also superimposed onto image Fig 40(b) to serve as a baseline for the flow field with forcing applied.

In identifying large-scale structures, taking after Adrian et al.,[53] the definition of a vortex offered by Kline and Robinson [54] was used as discussed previously. Again the two necessary conditions suggested previously are that the velocity field must be viewed in a convective reference frame and that the vorticity must be concentrated in the “core” of the structure. However, vorticity not only identifies vortex cores, but also shearing motions that may be also present in a flow.[53] Again, taking after Adrian et al.,[53] a number of methods have been developed for identifying locations of vortices and calculating vortex statistics from critical-point analysis of the local velocity gradient and its corresponding eigenvalues. In view of a three-dimensional field, the local velocity gradient tensor will have one real eigenvalue (λ_r) and a pair of complex conjugate eigenvalues ($\lambda_{cr} \pm i\lambda_{ci}$), when the discriminant of its characteristic equation is positive. As discussed by Chong et al.,[70] when this condition holds valid the particle trajectories about the eigenvector corresponding to the eigenvalue λ_r exhibit a swirling, spiral motion, where the quantity $(\lambda_{ci})^{-1}$ represents the period for a particle to swirl once about the λ_r -axis. Zhou et al. [71] [72] have further shown that λ_{ci} quantifies the strength of any swirling motion and hence, defined λ_{ci} as the swirling strength of a vortex. For two-dimensional PIV field, an equivalent form of the three-dimensional local velocity gradient tensor can be computed in the plane in which the PIV data lies from the following equation:

$$\underline{\underline{D}}^{2-D} = \begin{bmatrix} \frac{\partial u_1}{\partial x_1} & \frac{\partial u_1}{\partial x_2} \\ \frac{\partial u_2}{\partial x_1} & \frac{\partial u_2}{\partial x_2} \end{bmatrix} \quad (20)$$

where (x_1, x_2) are the streamwise and transverse directions and (u_1, u_2) the corresponding velocities. Eqn. (20) will have either two real eigenvalues or a pair of complex conjugate eigenvalues. Regions in which vortices exist can then be identified by plotting iso-regions of $\lambda_{ci} > 0$. Moreover, the swirling motion in these regions can be observed by performing a local Galilean decomposition in the immediate vicinity of peaks in swirling strength.[53] For the present work, Eqn. (20) was computed using a second-order, central-difference scheme for interior points, and second-order forward-differencing and backward-differencing schemes for the boundary points. Iso-regions for which $\lambda_{ci} > 0$ were then identified and plotted in a convective reference frame. The convective velocity was determined by the corresponding velocity at the location of peak swirling strength for a given iso-region. Additional details in vortex detection and visualization can be found in Ref. [53].

For the flow field including the excitation pulse, based on the results shown by the schlieren images, four delay times from the laser energy input at the jet exit were selected for investigation with PIV. This included delay times of: 20 μ s, 40 μ s, 60 μ s, and 80 μ s, respectively. Velocity field data from PIV were also obtained at these delay times for each of the three excitation positions relative to the jet exit. Again, this was at vertical distances of the excitation pulse from the jet exit of 0, 1.5, and 3 jet diameters and in each case, centered along the exit centerline. Vorticity plots for the three cases are shown in Fig 41, Fig 42, and Fig 43. As for the unperturbed case in Fig 40, streamlines for coherent structures within the flow field were calculated and superimposed onto the images. The method described above for visualizing vortices was again used, however, only vortices that were not observed in the baseflow were considered. Furthermore, vortices with a peak swirling strength of less than 25% of the maximum swirling strength seen in the unperturbed flow field were ignored. The threshold value was selected a priori to capture only the dominant structures induced into the flow through the excitation pulse. This approach also helped to eliminate any remnants of instantaneous features of the flow field that were not completed removed by averaging image pairs.

Beginning with image a) of Fig 41, a single vortex was visualized in the flow field at 20 μ s; this vortex has been labeled as I_{0D} . A circular region of increased positive vorticity can also be observed entering the field of view at the approximate coordinates of $(x/D, y/D) = (2, 2)$. Both of these features occurred in the wake of the blast wave from the excitation pulse, whose location is depicted as a curved black line in image 10a. By 40 μ s [Fig 41 (b)], five additional vortices developed in the flow field; however, only one of these vortices (labeled II_{DO}) remained coherent and persisted in the flow for increased delay times. This can be seen in images 41c and 41d for the increased delay time of 60 μ s and 80 μ s. The dark circular region of increased positive vorticity in image [Fig 41 (a)], can also be identified in image [Fig 41 (b)], separating vortices I_{DO} and II_{DO} .

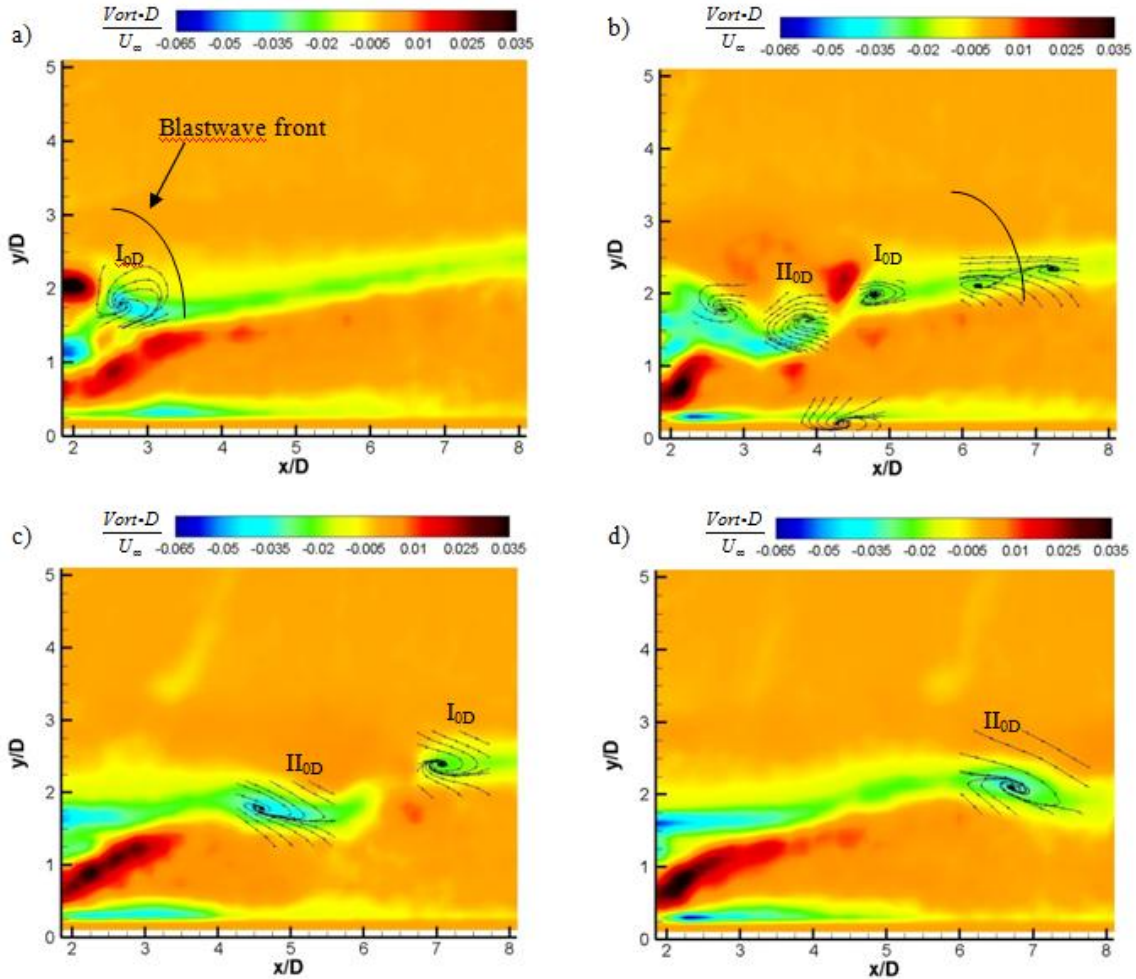


Fig 41. Vorticity contour plots for the 0D case and at delay times from a 200 mJ laser excitation pulse of (a) 20 μ s, (b) 40 μ s, (c) 60 μ s, and (d) 80 μ s.

Vorticity contour plots for the excitation location of $1.5D$ are shown in Fig 42. The four selected delay times ($20\ \mu\text{s}$, $40\ \mu\text{s}$, $60\ \mu\text{s}$, and $80\ \mu\text{s}$) are again considered, where Fig 42 (a) corresponds to the flow field at $20\ \mu\text{s}$ after the excitation pulse. In contrast to the $0D$ case, two vortices (labeled $I_{1.5D}$ and $II_{1.5D}$) were identified at this delay time and the front edge of the blast wave was positioned at a slightly further downstream location. The dark circular region of increased positive vorticity seen in image Fig 41 is also apparent in image Fig 42 (a), but with less intensity. It was not clear if this was due to its slightly further downstream position or through a different mechanism. At $40\ \mu\text{s}$, a relatively large gap (in comparison to the $0D$ case) develops between vortices $I_{1.5D}$ and $II_{1.5D}$. While at this delay time the position of $II_{1.5D}$ correlates well with II_{0D} , the center of vortex $I_{1.5D}$ is located almost one jet diameter upstream of I_{0D} . Vortices $I_{1.5D}$ and $II_{1.5D}$ both persist in the flow for increased delay times [(Fig 42 (c) and Fig 42 (d)], and their locations continue to be slightly downstream of those observed for the $0D$ case.

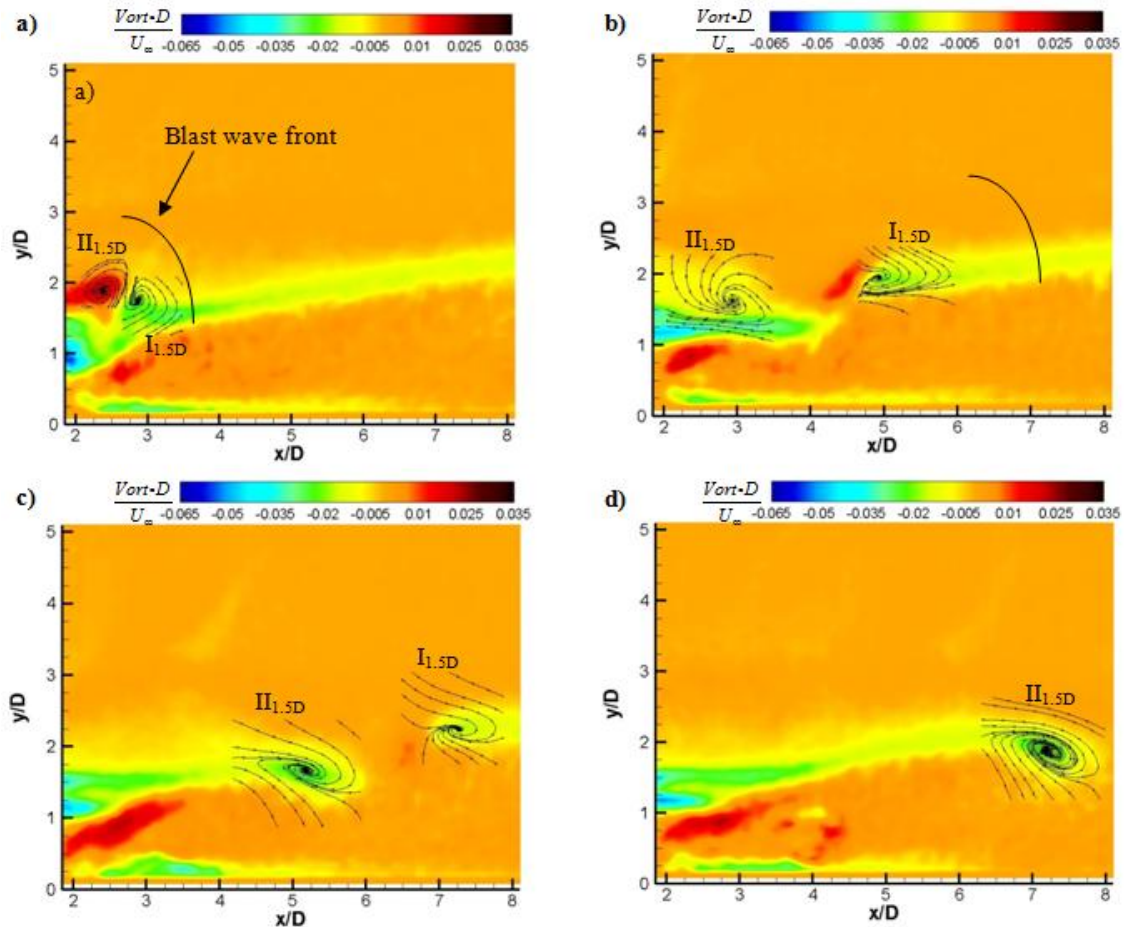


Fig 42. Vorticity contour plots for the $1.5D$ case and at delay times from a $200\ \text{mJ}$ laser excitation pulse of (a) $20\ \mu\text{s}$, (b) $40\ \mu\text{s}$, (c) $60\ \mu\text{s}$, and (d) $80\ \mu\text{s}$.

Lastly, vorticity contour plots for the vertical location of $3D$ are shown in Fig 43. From Fig 43 (a), two vortices (labeled I_{3D} and II_{3D}) formed in the flow field at a $20 \mu\text{s}$ delay time. Consistent with the trends from the $1.5D$ case, lowering the position of the excitation pulse into the flow field resulted in the center of both vortices and the location of the blast wave having a slightly more downstream position. The circular region of increased positive vorticity seen in the $0D$ and $1.5D$ case, however, was not observed for the $3D$ case. This region first appeared in image Fig 43 (b), separating the two vortices. In Fig 43 (b), both vortices appear with a further downstream position (in comparison to the previous two cases), but with less of a separation gap than in the $1.5D$ case. Vortices I_{3D} and II_{3D} continue to convect downstream [Fig 43 (c) and Fig 43 (d)] with increasing delay time.

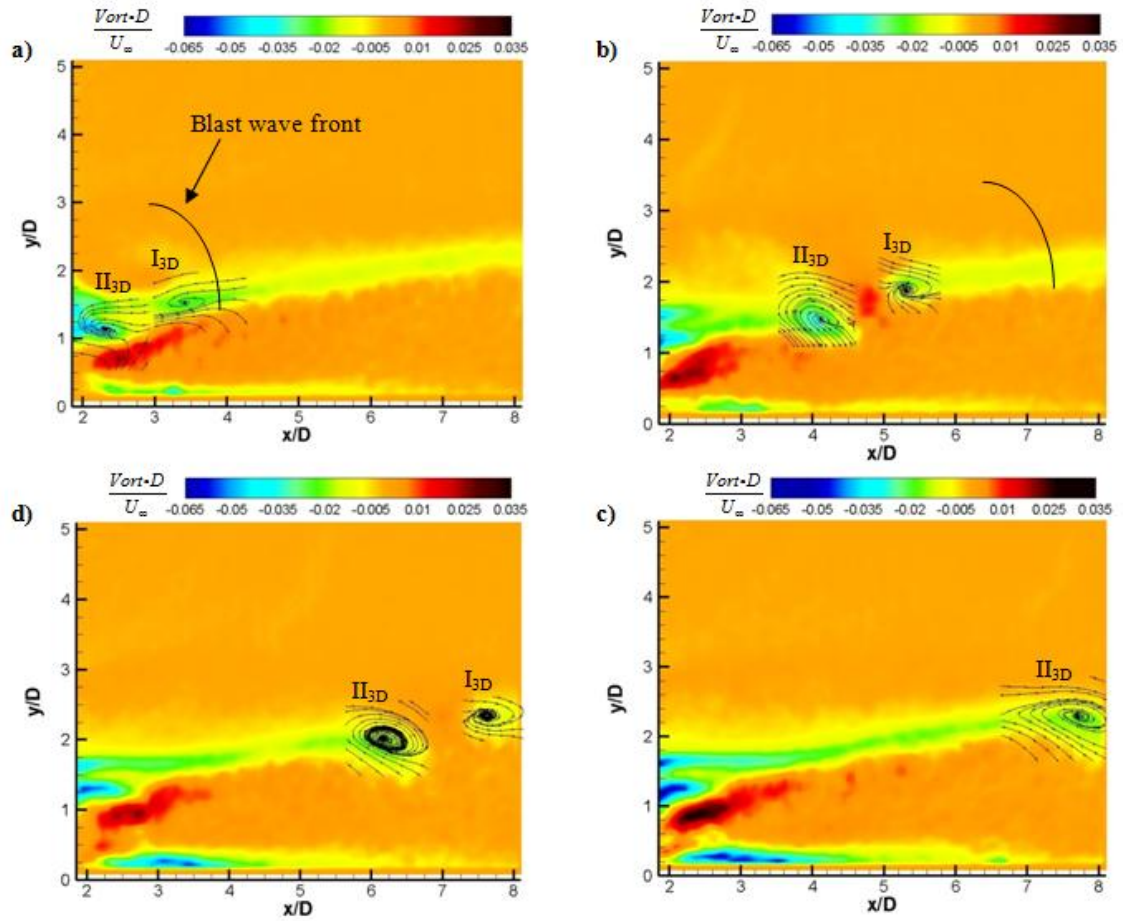


Fig 43. Vorticity contour plots for the $3D$ case and at delay times from a 200 mJ laser excitation pulse of (a) $20 \mu\text{s}$, (b) $40 \mu\text{s}$, (c) $60 \mu\text{s}$, and (d) $80 \mu\text{s}$.

As a means of further quantifying the behavior of the vortices seen in Fig 41, Fig 42, and Fig 43., as well as their relative strength, plots of the streamwise position and period required for a particle to swirl once about the λ_r -axis are given in Fig 44. In Fig 44, only vortices $I_{0D, 1.5D, 3D}$ (vortex I) and $II_{0D, 1.5D, 3D}$ (vortex II) are considered, and at delay times which they can be compared for the three vertical excitation positions. The streamwise positions (nondimensionalized by the jet exit diameter) of the vortices are shown as a function of delay time in image Fig 44 (a). This plot confirms the observations made from vorticity contour plots discussed above; specifically, as the excitation pulse is introduced at lower positions below the jet exit the vortices are either forming earlier or convecting through the flow field at an increased rate. While the data suggests the former for vortex I and the latter vortex II, it is difficult to infer any trends since only three points are being compared. The period required for a particle to swirl once about the λ_r -axis for both vortices are similarly shown as a function of delay time in Fig 44 (b). The values in Fig 44 (b) have been nondimensionalized by the vortex with the shortest period (or highest swirling strength) seen in the unperturbed flow field shown in Fig 40 (b). The shortest period calculated from the unperturbed flow field in Fig 40 (b) was approximately $(\lambda_{ci, \text{unperturbed}})^{-1} = 12.47 \text{ ms}^{-1}$. In Fig 44 (b), similar trends can be observed for the vortices induced with the excitation pulse located at vertical positions of $0D$ and $1.5D$. For these two cases, while for vortex II the period is decreasing in time, opposite behavior is seen for vortex I. Then for the case of the excitation pulse located at vertical positions of $3D$, the period increases in time for both, vortices I and II.

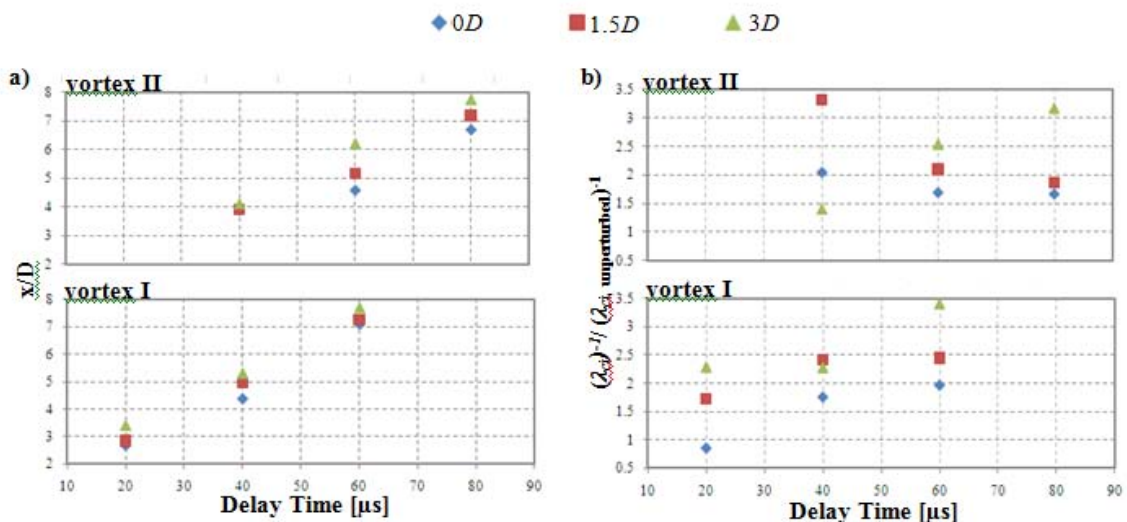


Fig 44. (a) Streamwise position and (b) period required for a particle to swirl once about the λ_r -axis for vortices $I_{0D, 1.5D, 3D}$ (Vortex I) and $II_{0D, 1.5D, 3D}$ (Vortex II).

4.6. Mixing Flow Visualizations: ELFC Transverse Jet in a Supersonic Cross Flow

A final diagnostic applied to the transverse jet flow field was planar Mie scattering from condensed ethanol droplets. The purpose of this diagnostic was to provide instantaneous images with higher spatial resolution for the study of large-scale structures and scalar mixing in the flow field. For this technique liquid ethanol was injected into the transverse jet flow as a fine mist of droplets by air atomization nozzles upstream of the test section, allowing for almost complete evaporation to be achieved in the near jet region. Scattered light from the particles was generated from a pulsed laser and then collected in the CCD camera as described above. Selected results are shown below in Fig 45 for 50 time averaged images. Fig 45 (a) corresponds to a baseline flow field without any forcing applied. Several of the characteristic features of a transverse jet flow can be identified and are labeled in the image; specifically, the bow shock, barrel shock, and Mach disk. In Fig 45 (b) 10 μ s have elapsed from the introduction of the plasma pulse into the flow field. Based on the PIV results, the plasma pulse was located at the 1.5D location, which the PIV image suggested to be an effective position for generating

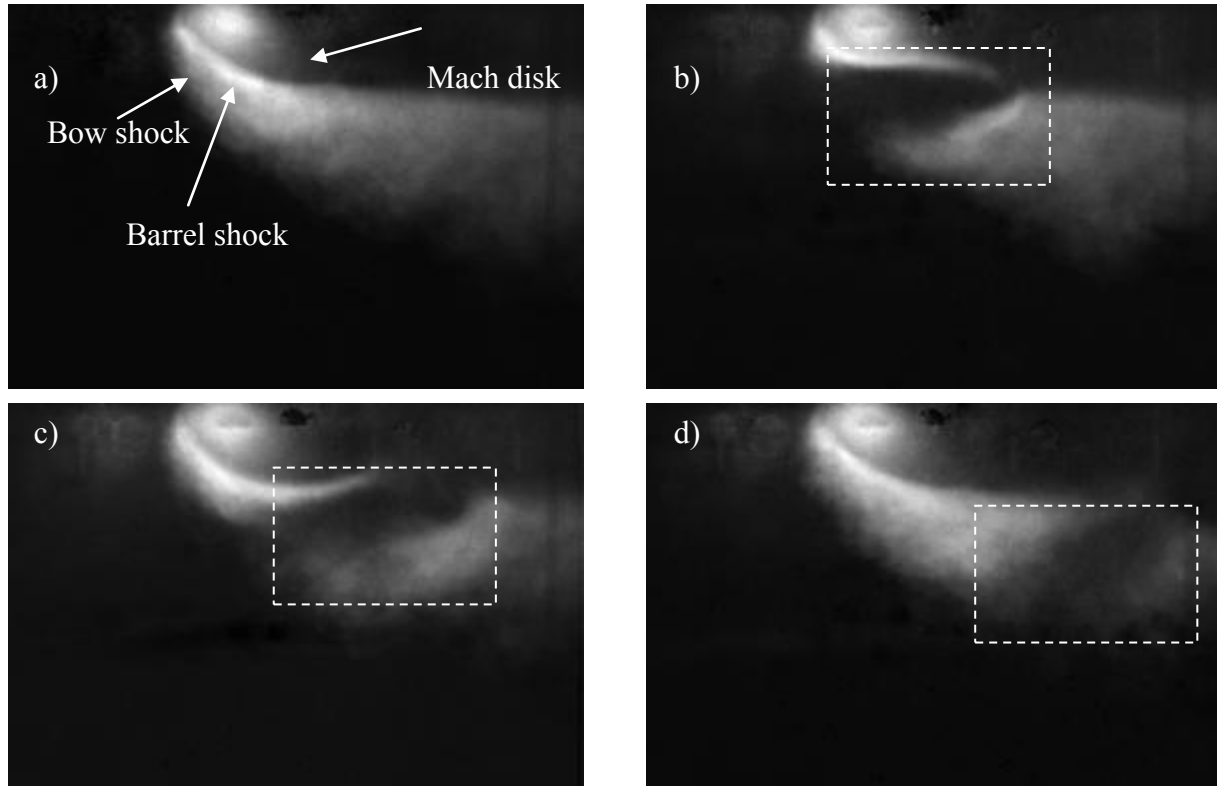


Fig 45. Time averaged Mie scattering images for a delay time from the excitation pulse of: (a) 0 μ s, (b) 10 μ s, (c) 20 μ s, and (d) 30 μ s.

structures in the jet shear layer. A large dark feature can be seen in Fig 45 (b) which is boxed in a dashed line. By comparing the location of this dark feature with the Fig 45, it appears to correlate well with the position of the large-scale structures visualized with the PIV data. Fig 45 also suggests that the structures are pulling warmer fluid from the crossflow and mixing it with the fluid from the jet exit. The temporal evolution of the structures is shown in Fig 45 (a) and Fig 45 (b), which correspond to a delay time of 20 μ s and 40 μ s.

5. CONCLUSIONS

In the present work, the effectiveness of electromagnetic local flow control (ELFC) has been considered. This effort has been conducted by investigating two different systems for generating an electromagnetic disturbance as well as being directly applied to two different flow field configurations that are commonly found in aerospace applications. The systems investigated for generating the electromagnetic disturbance included focused laser radiation and a microwave co-axial resonator. The plasma generated by each system was characterized through several diagnostics to determine its thermal properties and ability to be used as ELFC under a wide range of experimental conditions. The plasma generated by the laser spark system was also applied as a flow control technique for a supersonic cavity and transverse jet in a supersonic crossflow. For both flows, the disturbance generated by the laser spark was shown to be effective in inducing the formation of large-scale structures which may enhance fluid mixing and entrainment between the flows.

REFERENCES

- [1] L. Prandtl, "Über Flüssigkeitsbewegung bei sehr kleiner Reibung," *Proc. Third International Congress of Mathematics, Heidelberg, Germany*, pp. 484 – 491, 1904.
- [2] S. S. Collis, Joslin, R. D., Seifert, A., and Theofilis, V., "Issues in active flow control: theory, control, simulation, and experiment," *Progress in Aerospace Sciences*, vol. 40, pp. 237-289, 2004.
- [3] M. Gad-el-Hak, *Flow Control: Passive, Active, and Reactive Flow Management*,. New York: Cambridge University Press, 2000.
- [4] L. N. Cattafesta, Williams, D. R., Rowley, C. W., and Alvi, F. S., "Review of Active Control of Flow-Induced Cavity Resonance," *AIAA Paper 2003-3567*, 2003.
- [5] E. J. Gutmark, Schadow, K. C., and Yu, K. H., "Mixing Enhancement in Supersonic Free Shear Flows," *Annual Review Fluid Mechanics*, vol. 27, pp. 375-417, 1995.
- [6] A. Labergue, Moreau, Zouzou, E., and Touchard, G., , "Separation Control Using Plasma Actuators: Application to a Free Turbulent Jet," *Journal of Physics D: Applied Physics*, vol. 40, pp. 674-684, 2007.
- [7] N. Zhuang, Alvi, F. S., Alkislar, M. B., Shih, C., Sahoo, D., and Annaswamy, A. M., "Aeroacoustic Properties of Supersonic Cavity Flows and Their Control," *AIAA Paper 2003-3101*, 2003.
- [8] S. Chan, Zhang, X., Gabriel, S., "Attenuation of Low-Speed Flow-Induced Cavity Tones Using Plasma Actuators," *AIAA Journal*, vol. 45, pp. 1525-1538, 2007.
- [9] R. G. Adelgren, Elliott, G. S., and Crawford, J. B., "Axisymmetric Jet Shear-Layer Excitation by Laser Energy and Electric Arc Discharges," *AIAA Journal*, vol. 43 pp. 776-791, 2005.
- [10] D. Knight, "Survey of Aerodynamic Flow Control at High Speed by Energy Deposition," *AIAA Paper 2003-525*, 2003.
- [11] A. I. Klimov, Koblov, A. N., Mishin, G. I., Serov, Y. L., and Yavor, I. P., "Shock Wave Propagation in a Glow Discharge," *Soviet Technical Physics Letters*, vol. 8, pp. 192-194., 1982.
- [12] J. Von Hagen, Venot, Y., Zhang, Y., and Wiesbeck, W., "Microwave-Generated Plasma in Air Under Standard Conditions," *IEEE Transactions on Plasma Science*, vol. 29, pp. 604-608, 2001.
- [13] K. Linkenheil, Ruob, H.-O., Heinrich, W., "Design and Evaluation of a Novel Spark-Plug Based on a Microwave Coaxial Resonator," *34th European Microwave Conference*, 2004.
- [14] K. Linkenheil, Ruob, H.-O., Grau, T., Seidel, J., and Heinrich, W., "A Novel Spark-Plug for Improved Ignition in Engines with Gasoline Direct Injection (GDI)," *IEEE Transactions on Plasma Science*, vol. 33, pp. 1696-1702, 2005.
- [15] C. O. Laux, Spence, T. G., Kruger, C. H., and Zare, R. N, "Optical Diagnostics of Atmospheric Pressure Air Plasmas," *Plasma Sources Sciences and Technology*, vol. 12, pp. 125-138, 2003.
- [16] P. D. Maker, Terhune, R.W., and Savage, C.M. , *Proc. 3rd Int. Conf. Quantum Electronics, Paris, France*, vol. 2, 1963.
- [17] N. Glumac, Elliot, G., Boguszko, M., "Temporal and spatial evolution of a laser spark in air," *AIAA Journal*, vol. 43, pp. 1984–1994, 2005.
- [18] Y. P. Raizer, "Breakdown and Heating of Gases Under the Influence of a Laser Beam," *Soviet Physics Uspekhi*, vol. 8, pp. 650–673, 1966.
- [19] Y. P. Raizer, "Laser-Induced Discharge Phenomena," *Consultants Bureau, New York*, 1977.
- [20] R. Adelgren, Elliott, G., Knight, D., Zheltovodov, A., and Beutner T. J., "Energy Deposition in Supersonic Flows," *AIAA Paper 2001-0885*, 2001.
- [21] A. H. Bhuiyan, Richardsaon, D. R., Naik, S. V., and Lucht, R. P., "Development of an Optical Parametric Generator with Pulsed Dye Amplification for High-resolution Laser Spectroscopy," *Applied Physics B*, vol. 96, pp. 559-567, 2009.
- [22] W. D. Kulatilaka, Anderson, T. N., Bouger, T. L., and Lucht, R. P., "Development of Injection-Seeded, Pulsed Optical Parametric Generator/Oscillator Systems for High-Resolution Spectroscopy," *Applied Physics B*, vol. 80, pp. 669-680, 2005.

- [23] A. H. Bhuiyan, Naik, S. V., and Lucht, R. P., " High-Spectral Resolution PLIF Imaging of Compressible Flows and Plasmas," *AIAA Paper 2010-1408*, 2010.
- [24] I. G. Dors, and Parigger, C. G., "Computational Fluid-Dynamic Model of Laser-Induced Breakdown in Air," *Applied Optics*, vol. 42, pp. 5978-5985, 2003.
- [25] X. Zhang, "Compressible Cavity Flow Oscillation due to Shear Layer Instabilities and Pressure Feedback," *AIAA Journal*, vol. 33, pp. 1404-1411, 1995.
- [26] J. Zhang, Morishita E., Okunuki T., and Itoh, H., "Experimental and Computational Investigation of Supersonic Cavity Flows," *AIAA Paper 2001-1755*, 2001.
- [27] C.-K. Kim, Yu, S.-T. J., and Zhang, Z.-C., "Cavity Flow in Scramjet Engine by Space-Time Conservation and Solution Element Method," *AIAA Journal*, vol. 42, pp. 912-919, 2004.
- [28] K. H. Yu, Wilson, K. J., and Schadow, K. C., "Effect of Flame-Holding Cavities on Supersonic-Combustion Performance1295.," *Journal of Propulsion and Power*, vol. 17, pp. 1287-1295, 2001.
- [29] A. Ben-Yakar, and Hanson, R. K., "Cavity Flame-Holders in Ignition and Flame Stabilization in Scramjets: An Overview," *Journal of Propulsion and Power*, vol. 17, pp. 869-877, 2001.
- [30] R. C. Murray, and Elliott, G. S., "Characteristics of the Compressible Shear Layer over a Cavity," *AIAA Journal*, vol. 39, pp. 846-856, 2001.
- [31] A. Quick, King, P. I., Gruber, M. R., Carter, C. D., Hsu, K.-Y., "Upstream Mixing Cavity Coupled with a Downstream Flameholding Cavity Behavior in Supersonic Flow," *AIAA Paper 2005-3709*, 2005.
- [32] J. E. Rossiter, "Wind Tunnel Experiments on the Flow over Rectangular Cavities at Subsonic and Transonic Speeds.," *Aeronautical Research Council, Repts. and Memoranda No. 3488, London*, 1964.
- [33] O. H. Unalmis, Clemens, N. T., and Dolling, D. S., "Cavity Oscillation Mechanisms in High-Speed Flows," *AIAA Journal*, vol. 40, pp. 2035-2041, 2004.
- [34] H. H. Heller, and Bliss, D. B., "The Physical Mechanism of Flow-Induced Pressure Fluctuations in Cavities and Concepts for Their Suppression," *AIAA Paper 75-491*, 1975.
- [35] G. Brown, and Roshko, A., "On Density Effects and Large Structure in the Turbulent Mixing Layers," *Journal of Fluid Mechanics*, vol. 64, pp. 775-816, 1974.
- [36] A. J. Smits, and Dussauge, J. P., *Introduction, "Turbulent Shear Layers in Supersonic Flow"* vol. 2nd ed. New York: Springer, 2005.
- [37] D. Papamoschou, and Roshko, A., "The Compressible Turbulent Shear Layer: An Experimental Study," *Journal of Fluid Mechanics*, vol. 197, pp. 453-477, 1988.
- [38] T. C. Island, Urban, W. D., Mungal, M. G., "Mixing enhancements in compressible shear layers via sub-boundary layer disturbances " *Physics of Fluids*, vol. 10, pp. 1008-1020, 1998.
- [39] N. Zhuang, Alvi, F. S., Alkislar, M. B., Shih, C., Sahoo, D., and Annaswamy, A. M., "Supersonic Cavity Flows and their Control," *AIAA Journal*, vol. 44, pp. 2118-2128., 2006.
- [40] D. P. Rizzetta, and Visbal, M. R., "Large-Eddy Simulation of Supersonic Cavity Flowfields Including Flow Control," *AIAA Journal*, vol. 41, pp. 1452-1462, 2003.
- [41] S. Aradag, Yan, H., and Knight, D., "Energy Deposition in Supersonic Cavity Flow," *AIAA Paper 2004-514*, 2004.
- [42] T. Swanson, "Interaction of Laser Energy Deposition with a Normal Shock," *M.S. Thesis, Univ. of Illinois, Urbana-Champaign, IL*, 2006.
- [43] S. Martens, Kinzie, K. W., and McLaughlin, D. K., "Measurements of Kelvin-Helmholtz Instabilities in a Supersonic Shear Layer," *AIAA Journal*, vol. 32, pp. 1633-1639., 1994.
- [44] N. D. Sandham, and Reynolds, W. C.4, "Compressible Mixing Layer: Linear Theory and Direct Simulation," *AIAA Journal*, vol. 28, pp. 618-624, 1990.
- [45] N. T. Clemens, and Mungal, M. G., "Two- and Three- Dimensional Effects in the Supersonic Mixing Layer," *AIAA Journal*, vol. 30, pp. 973-981, 1992.

[46] W. M. Humphreys, and Bartram, S. M., "Measurement of Separating Flow Structures using a Multiple-camera DPIV System," *19th International Congress on Instrumentation in Aerospace Simulation Facilities*, 2001.

[47] W. D. Urban, and Mungal, M. G., "Planar Velocity Measurements in Compressible Mixing Layers," *Journal of Fluid Mechanics*, vol. 431, pp. 189-222. , 2001.

[48] R. Huffman, "An Experimental Investigation into the Effect of Plasma on the Flow Features of an Axisymmetric Jet," *PhD Dissertation, Univ. of Illinois, Urbana-Champaign, IL*, 2006.

[49] F. Scarano, and Oudheusden, B. W., "Planar Velocity Measurements of a Two-dimensional Compressible Wake," *Experiments in Fluids*, vol. 34, pp. 430-441, 2003.

[50] A. Melling, "Seeding Gas Flows for Laser Anemometry," *AGARD Conference Proceedings*, pp. 8.1-8.11, 1986.

[51] M. Samimy, and Lele, S. K. , "Motion of Particles with Inertia in a Compressible Free Shear Layer," *Physics of Fluids*, vol. 3, pp. 1915-1923., 1995.

[52] J. L. Herrin, and Dutton, J. C., "Effect of a Rapid Expansion on the Development of Compressible Free Shear Layers," *Physics of Fluids*, vol. 7, pp. 159-171, 2003.

[53] R. J. Adrian, and Christensen, K. T., and Liu, Z.-C., "Analysis and Interpretation of Instantaneous Turbulent Velocity Field," *Experiments in Fluids*, vol. 29, pp. 275-290, 2000.

[54] S. J. Kline, and Robinson, S. K.,, " Quasi-coherent Structures in the Turbulent Boundary Layer. Part I: Status Report on a Community-wide Summary of the Data," *Proceedings of Zaric Memorial Conference*, pp. 200-217, 1989.

[55] S. R. Shapiro, King, J. M., M'Closkey, R. T., and Karagozian, A. R., "Optimization of Controlled Jets in Crossflow," *AIAA Journal*, vol. 44, pp. 1292-1298, 2006.

[56] R. W. Cubbison, Anderson, B. H., and Ward, J. J., "Surface Pressure Distributions with a Sonic Jet Normal to Adjacent Flat Surfaces at Mach 2.92 to 6.4," *NASA TN D-580*, 1961.

[57] J. J. Janos, "Loads Induced on a Flat-Plate Wing by an Air Jet Exhausting Perpendicularly Through the Wing and Normal to a Free-Stream Flow of Mach number 2.0," *NASA TN D-649*, 1961.

[58] A. Ben-Yakar, Mungal, M. G., and Hanson, R. K., "Time Evolution and Mixing Characteristics of Hydrogen and Ethylene Transverse Jets in Supersonic Crossflows," *Physics of Fluids*, vol. 18, p. p. 026101, 2006.

[59] L. S. Alves, Kelly, R. E., and Karagozian, A. M., "Local Stability Analysis of an Inviscid Transverse Jet," *Journal of Fluid Mechanics*, vol. 581, pp. 401 – 418, 2007.

[60] M. R. Gruber, Nejad, A. S., Chen, T. H., and Dutton, J. C., "Mixing and Penetration Studies of Sonic Jets in a Mach 2 Freestream," *Journal of Propulsion and Power*, vol. 11, pp. 315 – 323, 1995.

[61] W. M. VanLerberghe, Santiago, Dutton, J. G., and Lucht, R. P., "Mixing of a Sonic Transverse Jet Injected into a Supersonic Flow," *AIAA Journal*, vol. 38, pp. 470 – 479., 2000.

[62] R. a. B. Srinivasan, R. , "Simulation of Transverse Gaseous Injection through Diamond Ports into a Supersonic Freestream," *Journal of Propulsion of Power*, vol. 23, pp. 772 – 782, 2007.

[63] T. F. a. R. Fric, A., "Vortical Structure in the Wake of a Transverse Jet," *Journal of Fluid Mechanics*, vol. 275, pp. 1 – 47, 1994.

[64] S. Murugappan, Gutmark, E., Carter, C. Dunbar, J., Gruber, M., Hsu, K.-Y., ", "Transverse Supersonic Controlled Swirling Jet in a Supersonic Cross Stream," *AIAA Journal*, vol. 44, pp. 290 – 300. , 2006.

[65] F. S. Billig, Orth, R. C., and Lasky, M., "A Unified Analysis of Gaseous Jet Penetration," *AIAA Journal*, vol. 9, pp. 1048 – 1058., 1971.

[66] S. a. L. Kawai, S., "Mechanisms of Jet Mixing in a Supersonic Crossflow: A Study Using Large-Eddy Simulation," 2008., 2008.

[67] J. G. Santiago, and Dutton, J. C., ", "Velocity measurements of a jet injected into a supersonic crossflow," *Journal of Propulsion and Power*, vol. 13, pp. 264 – 273, 1997.

- [68] I. a. O. Grant, E., "Confidence Interval Estimates in PIV Measurements of Turbulence Flows," *Applied Optics*, vol. 29, pp. 1400–1402, 1990.
- [69] D. E. Everett, Woodmansee, M. A., Dutton, J. C., and Morris, M. J., "Wall Pressure Measurements for a Sonic Jet Injected Transversely into a Supersonic Crossflow," *Journal of Propulsion and Power*, vol. 14, pp. 861 – 868 1998.
- [70] M. S. Chong, Perry, A. E., Cantwell, B. J., "A General Classification of Three-Dimensional Flow Fields," *Physics of Fluids*, vol. 2, pp. 408–420, 1990.
- [71] J. Zhou, Adrian, R. J., Balachandar, S. , "Autogeneration of Near-Wall Vortical Structures in Channel Flow," *Physics of Fluids*, pp. 288-190, 1996.
- [72] J. Zhou, Adrian, R. J., Balachandar, S. Kendall, T. M., "Mechanisms for Generating Coherent Packets of Hairpin Vortices in Channel Flow," *Journal of Fluid Mechanics*, vol. 387, pp. 353-359, 1999.

Acknowledgment/Disclaimer

This work was sponsored (in part) by the Air Force Office of Scientific Research, USAF, under grant/contract number FA9550-07-1-0215. The views and conclusions contained herein are those of the authors and should not be interpreted as necessarily representing the official policies or endorsements, either expressed or implied, of the Air Force Office of Scientific Research or the U.S. Government.

Personnel Involved in University of Illinois Research Effort

Greg Elliott	Professor, University of Illinois
Nick Glumac	Professor, University of Illinois
Eli Lazar	Graduate Student, University of Illinois

Publications Stemming from Research Effort

1. Lazar, E., "Control of the Shear Layer above a Supersonic Cavity Using Energy Deposition," Masters Thesis, University of Illinois at Urbana-Champaign, 2008.
2. Lazar, E., Elliott, G.S., and Glumac, N., "Microwave Generated Plasma for Active Flow Control in Aerodynamic Applications," AIAA Paper 2008-1387, *46th AIAA Aerospace Sciences Meeting and Exhibit*, Reno, Nevada, 2008.
3. Lazar, E., Elliott, G.S., and Glumac, N., "Energy Deposition for Control of a Supersonic Cavity," *AIAA Journal*, Vol. 46, No. 12, pp. 2987-2997, 2008.
4. Lazar, E., Elliott, G.S., and Glumac, N., "Energy Deposition applied to a Transverse Jet in a Supersonic Flow," AIAA Paper 2009-1534, *47th AIAA Aerospace Sciences Meeting and Exhibit*, Orlando, Florida, 2009. *AIAA Plasmadynamics and Lasers Conference Outstanding paper Award*, 2009.
5. Lazar, E., Elliott, G.S., and Glumac, N., "Energy Deposition applied to a Transverse Jet in a Supersonic Flow," *Submitted to the AIAA Journal*, 2009.